

**Anatomical, Functional, and Molecular Imaging of left Ventricular Myocardial  
Infarction in Mice Using High Frequency Ultrasound**

A Dissertation

Presented to

the faculty of the School of Engineering and Applied Science

University of Virginia

---

in partial fulfillment

of the requirements for the degree

Doctor of Philosophy in Biomedical Engineering

by

Dan Lin

August, 2014

APPROVAL SHEET

The dissertation  
is submitted in partial fulfillment of the requirements for  
the degree of  
Doctor of Philosophy

Dan Lin  
AUTHOR

The dissertation has been read and approved by the examining committee:

Dr. John A. Hossack  
Advisor

Dr. Brent A. French

Dr. Jeffrey W. Holmes

Dr. Craig H. Meyer

Dr. Scott T. Acton

Dr. Alexander L. Klibanov

Accepted for the School of Engineering and Applied Science:



Dean, School of Engineering and Applied Science

August, 2014

# Abstract

Echocardiography plays a vital role in the evaluation of patients with suspected cardiovascular disease. Heart disease is the leading cause of death worldwide, with myocardial infarction being the major contributing factor to the high morbidity and mortality rates. Preclinical research on heart attack and heart failure is frequently conducted in mouse models of myocardial ischemia. The mouse species is preferred due to its low-cost, short reproductive cycle, and its utility in studying the role of specific genes in the pathophysiology of myocardial ischemia via transgenic and knockout mice. High frequency ultrasound is well suited to in vivo imaging of the mouse heart due to its high spatial and temporal resolution, lack of ionizing radiation, versatility, low-cost, ease of use, and non-invasive nature.

To demonstrate the utility of high frequency ultrasound in small animal imaging, I explore several novel approaches to quantify cardiac function in mouse models of myocardial ischemia and infarction. In Chapters 2 and 3, reconstruction of 3D motion in the mouse left ventricle is demonstrated by combining orthogonal 2D displacement fields. A finely sampled matrix of 3D motion vectors is then used to build a kinematic model of the left ventricle using polynomial functions and by assuming that the myocardium is approximately incompressible. In Chapter 4, novel metrics for quantification of left ventricular dyssynchrony and infarct size using ultrasound displacement and strain data, respectively, are presented. Using these metrics, myocardial contractile dysfunction in inducible nitric oxide synthase knockout mice exhibits improved function after myocardial infarction compared to control, wild type mice. Finally, in Chapter 5, a method for identifying previously ischemic regions of the myocardium by using molecularly targeted ultrasound contrast agents is presented.

# Acknowledgments

I would like to thank the members of my committee who made this dissertation possible. First, I would like to thank my advisor, Dr. John Hossack, for giving me the opportunity to learn from him. Dr. Hossack's knowledge of ultrasound, guidance, support, and advice were essential for the completion of this dissertation. I would like to acknowledge Dr. Hossack's grants that supported most of the work in this dissertation: NIH NIBIB - EB001826, and NCCR - RR027333. I would like to thank Dr. Brent French for sharing his expert knowledge on mouse cardiovascular physiology and his invaluable guidance throughout all of the projects presented in this dissertation. I would like to thank Dr. Jeffrey Holmes for his expertise in heart mechanics and mathematical modeling which contributed significantly to my understanding and this dissertation. I would also like to recognize the other members of my committee, Dr. Alexander Klibanov, Dr. Craig Meyer, and Dr. Scott Acton for challenging me to think critically about my dissertation.

I would also like to thank my colleagues for their assistance, insightful comments, and critiques toward my dissertation. From Dr. Hossack's lab, Dr. Ali Dhanaliwala, Dr. Joseph Kilroy, Adam Dixon, Shiyang Wang, and Dr. Will Mauldin have all provided ultrasound knowledge and ideas for experimental design and data acquisition. From Dr. French's Lab, I would like to thank Daniel O'Connor for his assistance with mouse imaging as well as Yikui Tian and Yaqin Xu for their skills in animal surgery. From Dr. Klibanov's lab, I would like to thank Sunil Unnikrishnan for his insightful discussion on microbubbles.

Lastly, I would like to thank my parents for their unconditional support and patience during the five years of my PhD training.

# Table of Contents

<b>Abstract</b> .....	<b>I</b>
<b>Acknowledgments</b> .....	<b>II</b>
<b>Table of Contents</b> .....	<b>III</b>
<b>List of Figures</b> .....	<b>V</b>
<b>List of Abbreviations</b> .....	<b>XV</b>
<b>Chapter 1: Introduction</b> .....	<b>1</b>
<b>Chapter 2: Reconstruction of 3D Myocardial Displacement</b> .....	<b>7</b>
2.1 INTRODUCTION .....	7
2.2 METHODS .....	8
2.3 RESULTS .....	14
2.4 DISCUSSION.....	16
<b>Chapter 3: Kinematic Model of LV Using Near Incompressibility</b> .....	<b>18</b>
3.1 INTRODUCTION .....	18
3.2 METHODS .....	21
3.2.1 Mouse Heart Imaging and Motion Estimates.....	21
3.2.2 Myocardial Incompressibility.....	22
3.2.3 General Model Formulation .....	23
3.2.4 Linear Model of Deformation in the Normal Mouse Heart.....	25
3.2.5 Polynomial Model of Deformation in Normal and Infarcted Mouse Heart .....	27
3.3 RESULTS .....	29
3.3.1 Linear Model of Deformation in Normal Mouse Heart.....	29
3.3.2 Polynomial Model of Deformation in Normal and Infarcted Mouse Heart .....	33
3.3.2 Impact of the Incompressibility Constraint .....	35
3.4 DISCUSSION.....	37
<b>Chapter 4: iNOS KO Mice Exhibit Reduced LV Dysfunction</b> .....	<b>42</b>
4.1 INTRODUCTION .....	42
4.2 METHODS .....	44
4.2.1 Animal Model and Myocardial Infarction.....	44
4.2.2 Ultrasound Image Acquisition .....	44
4.2.3 Quantifications of Cardiac Function .....	46
4.3 RESULTS .....	50

4.4 DISCUSSION.....	57
<b>Chapter 5: Ultrasound-Mediated Molecular Imaging.....</b>	<b>60</b>
5.1 INTRODUCTION .....	60
5.2 METHODS .....	63
5.2.1 Microbubble Preparation.....	63
5.2.2 Animal Imaging .....	64
5.3 RESULTS .....	67
5.4 DISCUSSION.....	71
<b>Chapter 6: Modeling Human Arterial Wall Motion.....</b>	<b>74</b>
6.1 INTRODUCTION .....	74
6.2 METHODS .....	76
6.2.1 Ultrasound Estimation of Wall Motion.....	76
6.2.2 Viscoelastic Model of Wall Motion .....	78
6.3 RESULTS .....	79
6.4 DISCUSSION.....	82
<b>Chapter 7: Motion Estimation Using the Monogenic Signal.....</b>	<b>84</b>
7.1 INTRODUCTION .....	84
7.2 METHODS.....	86
7.2.1 The Monogenic Signal .....	86
7.2.2 Synthetic Mouse Heart Data .....	89
7.2.3 In vivo Mouse Heart Data Acquisition .....	90
7.2.4 Speckle Tracking (MSAD) .....	91
7.2.5 Displacement Estimation via the Monogenic Signal .....	91
7.3 RESULTS .....	92
7.4 DISCUSSION.....	95
<b>Chapter 8: Conclusions.....</b>	<b>97</b>
8.1.1 Kinematic Models of Left Ventricle Using Near Incompressibility.....	97
8.1.2 Improved Cardiac Function in iNOS KO Mice .....	98
8.1.3 Ultrasound-Mediated Molecular Imaging Using Targeted Microbubbles .....	99
<b>References.....</b>	<b>100</b>

## List of Figures

Figure 2.1: Acquisition and orientation of SA and LA cines. The endocardial wall surface is shown in red and the epicardial surface in yellow. Only the slices near the center of the LV are shown for illustrative purposes. Intervals between each SA and LA slices are 0.5mm.

Figure 2.2: Displacement field derived from speckle tracking for an SA image with severe image artifact. In this example, the anteroseptal region of the LV is shadowed by reverberation from sternum. (A) Speckle tracking of raw displacement data illustrates absence of displacement arrows in the region shadowed by the sternum. (B) Full displacement field obtained after applying the LV kinematic model.

Figure 2.3: The scatter plot above shows the correlation between axial displacements from SA and LA data at intersection points. Displacements near the apex are more disperse.

Figure 2.4: 3D trajectory the points in the LV. Magnified view of region in the cube on the right shows loops that are not completed enclosed, this corresponds to the error in tracking. Each red and green segment represents the distance traversed in every 2 frames.

Figure 2.5: Displacement components in the basal (top row), mid (middle row), and apical (bottom row) regions of the LV. Contrasts between displacement from normal (black curves) and infarcted (red curves) hearts are shown. Unit is in millimeter.

Figure 3.1: Linear regression of LV deformed longitudinal (A) and circumferential (B) positions and circumferential displacement (C) in a representative normal mouse heart. LV extension (slope  $> 1.0$  in panel A) and torsion (different signs of mean circumferential displacement in panel C) are apparent in both raw and fitted data.

Figure 3.2: Radial (panels A and B) and circumferential (panels C and D) observed (circles) and polynomial model predicted (triangles) displacement of points throughout the myocardium as derived from speckle tracking using SA B-mode images for infarcted (panels A and C) and normal (panels B and D) hearts. X-axes in panels A and B are myocardial position in SA view as defined in panel E. Region in the enclosed red contour is the infarcted zone, with minimal radial displacement and clockwise circumferential motion.

Figure 3.3: Linear model simulations for normal hearts using different combinations of  $a$  and  $c$ . The NRMSE is calculated for each simulation and the combination with the minimum NRMSE (*arrow*) represents the optimal parameter values.

Figure 3.4: Observed and linear model-predicted radial motion at the basal (A), midventricular (B) and apical (C) levels of a normal LV.

Figure 3.5: Mean Squared Error (MSE) in the polynomial model for each component of the optimization Equation (13) for a representative infarcted heart. Higher incompressibility weights push the determinant value closer to 1, decreasing incompressibility error (blue curve). The tradeoff for increasing incompressibility weights is the increase in error in the longitudinal (black curve) and radial (red curve) deformation components.

Figure 3.6: Color map of myocardial displacement derived from using MSAD speckle tracking only (A), and corrected displacement map using the polynomial kinematic model (B). Color represents relative magnitude of displacement. In (A), improbable displacements are observed where myocardial regions appear to collapse or overlap as shown inside the white circle.

Figure 4.1: (A) Mouse setup during imaging (not drawn to scale). Mouse is kept sedated through constant infusion of anesthesia from an isoflurane gas tank. Sensors on the platform monitor both heart rate and respiration, while also providing heat to help maintain normal body temperature. An external lamp provides additional source of heat, and body temperature is monitored using a digital rectal thermometer. (B) Acquisition of parallel SA B-mode cines along the length of the ventricle. Adjacent B-mode cines are 0.5 mm apart. For display purpose, B-mode cines for every other slice are omitted (dotted blue outline). ESV and EDV volumes are quantified using Simpson's disc method, where endocardial contours (green) defined at ES and ED are used to derive at cylindrical discs (red) at 0.5 mm thickness.

Figure 4.2: Radial strain data derived from ultrasound speckle tracking in SA B-mode cines were used to determined infarct size after MI. Infarct size were similar between KO and WT on days 2 and 4 after MI. Significant differences in infarct sizes were observed on days 14 and 28 after MI.

Figure 4.3: Time course of CI values show reduced dyskinetic systolic bulging in KO mice after 4 days post MI ( $p < 0.05$  compared to WT mice). Myocardial dyskinesia occurs early after MI for both groups.

Figure 4.4: Time course of ESV and EDV (E) shows similar volumes at baseline, D2, and D4 between WT and KO mice. Volumes diverge after D4 and are significantly different between WT and KO at D7, D14, and D28 ( $p < 0.05$ ). Panels A-D are examples of LA B-mode images, A, WT at ED; B, KO at ED; C, WT at ES; and D, KO at ES). LV cavity areas based on endocardial wall tracing (shaded red region) are also shown. While not the actual volume measurements, these area measurements showed attenuated LV remodeling for iNOS KO mice late after MI. Scale bar in each B-mode image is 1mm.

Figure 4.5: Time course of EF computed as the ratio of the difference between EDV and ESV to EDV. Both groups have similar EF on Baseline, and D2 and D7 post-MI. Significant differences in EF between KO and WT mice are observed D7 and D29 post-MI.

Figure 4.6: Time course of DI shows increased dyssynchronous myocardial motion after MI for both groups. Dyssynchrony was most apparent at D4, with KO mice exhibiting less dyssynchrony than WT mice ( $p < 0.05$ ).

Figure 4.7: Epicardial and endocardial were manually traced at ES phase of the cardiac cycle for all time points. Circumferential extent of wall thinning is defined as the extent (in degrees) of myocardium where thickness is less than 50% of baseline values. Panels A and B above are baseline SA B-mode images (acquired 2mm from apex) for WT and KO mice, respectively. Myocardial region is shown in green. Panels C and D are SA B-mode images acquired at D14 for WT and KO mice, respectively. Regions of significant wall thinning is shown between red arrows. Scale bars are 1mm.

Figure 4.8: Time course of wall thinning between KO and WT mice acquired at the basal (A), mid (B), and apical (C) levels of the LV, and the average total (D) across all acquired SA slices. As a result of LAD ischemic-reperfusion surgery, apical slices have greater extent in wall thinning.

Figure 5.1: Specific ligands can be attached to the microbubble shell that binds to a selected receptor that is displayed on the activated endothelial cells during the course of the disease of interest. Microbubble targeting can mimic the behavior of leukocytes during inflammation.

Figure 5.2: Conjugation of targeted ultrasound microbubble. Specific ligand of interest are conjugated to microbubble via a biotin-streptavidin bridge. Targeted microbubble design consist of single targeted microbubbles using control anti-VCAM isotype, anti-P-Selectin, Sialyl Lewis X, anti-VCAM, and dual targeted microbubbles using Sialyl Lewis X and anti-VCAM.

Figure 5.3: Timeline and signal processing of molecular imaging experiment. Mice underwent ischemia/reperfusion injury via 15 minutes occlusion of the left anterior descending (LAD) coronary artery followed by 2 hours reperfusion. Mice were imaged with a Sequoia 15L8 transducer at 14 MHz (panel 1) and video data were processed offline to arrive at regional time intensity curve (panels 4 and 5). Video data were compared to histological stains (panels 2 and 3) to assess the accuracy of targeted microbubbles using ROC analysis (panel 6).

Figure 5.4: Normalized microbubble concentration (top) and mean diameter (bottom) from *in vitro* constant infusion experiments. Both microbubble concentration and diameter decreases over time, the change is insignificant over the first 4-minute of the infusion.

Figure 5.5: Normalized intensities, plotted as the ratio of intensity in the ischemic region to the intensity in the non-ischemic region. (\*  $P < 0.05$  compared to  $MB_i$ , #  $P < 0.05$  compared to  $MB_v$ ,  $MB_x$ , and  $MB_p$ )

Figure 5.6: ROC curves using histological stain as the gold standard showed accurate detection of both ischemic and non-ischemic regions using  $MB_D$  (AUC = 0.90),  $MB_x$  (AUC = 0.89),  $MB_p$  (AUC = 0.87), and  $MB_v$  (AUC = 0.97).

Figure 6.1: B-mode image of the common carotid artery. Image on the right is a magnified view of the yellow rectangular region, showing the intima (the bright band touching the vessel lumen), the media (the dark band below the intima), and the adventitia/surrounding tissue. The transducer was focused at the distal wall, as tracking of the proximal wall was impeded by signal artifacts.

Figure 6.2: Blood flow velocity measured in the center of common carotid artery using pulse wave Doppler. The red curve is a representative pressure waveform derived from a series of Gaussian functions over the velocity profile.

Figure 6.3: Displacement field of distal carotid wall derived using 2D RF speckle tracking. Displacement vectors are color-coded based on magnitude (scale bar shown at the top). The green curve is the ECG trace and tracking was performed from end-diastole to end-systole (portion of the ECG curve shown in red).

Figure 6.4: Comparison of arterial radial displacement using speckle tracking (black lines) and model simulation (dotted red lines) for points in the intima (top) and adventitia (bottom). Subpanel below each graph shows the absolute percent error (black), and ECG tracing in green.

Figure 7.1: Surface of the RBF constructed using difference of Gaussian functions. RBF is an even filter and radially symmetric. The goal of this filter is to maintain the main characteristics of the image structure within a defined range of frequency.

Figure 7.3: Random scatterers used for simulating a short-axis view of the left ventricle (Black = surrounding tissues, green = myocardium, red = blood).

Figure 7.4: Synthetic B-mode image simulated with Field II. Green displacement vectors is shows motion from end-diastole to end-systole, and is enforced using an mathematical model based on myocardial incompressibility.

Figure 7.5: Tracked displacement vector using MSAD speckle tracking algorithm.

Figure 7.6: Phase-based tracking technique yields more uniform displacement vectors over MSAD block-matching technique.

Figure 7.7: Displacement magnitude of mouse left ventricular wall at the mid-papillary level shown through a complete heart cycle. Phase-based tracking show lower tracking error as shown by lower displacement at the end of the cardiac cycle (inset, upper right), where the final displacement should be zero.

Figure 7.8: Displacement of mouse left ventricle in long-axis view from end-diastole to end-systole. Green arrows on the cavity show orientation of blood flow during late systole.

## List of Abbreviations

2D, 3D	Two-dimensional, Three-dimensional
AHA	American Heart Association
AUC	Area under the curve
BSL	Baseline
cGMP	Cyclic guanosine monophosphate
CI	Contraction index
CVD	Cardiovascular disease
CURE	Circumferential uniformity ratio estimate
DI	Dyskinesia Index
DSPC	1,2-dioctadecanoyl-sn-glycero-3-phosphocholine
ECG	Electrocardiogram
ED	End-diastole
EDV	End-diastolic volume
EF	Ejection fraction
ES	End-systole
ESV	End-systolic volume
FOV	Frame of view

FIR	Finite impulse response
FS	Fractional shortening
ICAM	Intercellular adhesion molecule
IHME	Institute of health metrics and evaluations
IMT	Intima-media thickness
iNOS	Inducible nitric oxide synthase
KO	Knockout
LAD	Left anterior descending (Coronary artery)
LGE	Late gadolinium enhancement
MI	Myocardial infarction
MRI	Magnetic resonance imaging
MSAD	Minimum sum absolute difference
MSE	Mean square error
NO	Nitric oxide
NRMSE	Normalized root mean square error
PE	Phosphatidylethanolamine
PEG	Polyethylene glycol
RBF	Radial bandpass filter
RF	Radio frequency

ROC	Receiver-operating characteristic
RURE	Radial uniformity ratio estimate
SA	Short-axis
SNR	Signal to noise ratio
SQF	Spherical quadrature filter
TTC	Triphenyltetrazolium chloride
VCAM	Vascular cell adhesion molecule
WT	Wild type

## Chapter 1: Introduction

Ultrasound is a ubiquitous and versatile imaging modality with both diagnostic and therapeutic clinical applications. Particularly, cardiovascular ultrasound, or echocardiography, is a vital component in the evaluation of patients with suspected cardiovascular diseases. Globally, cardiovascular disease (CVD) remains the leading cause of death (AHA 2013). Technological and medicinal advances have resulted in a gradual decline in overall cardiovascular death rate; however, the majority of the decline is observed in people over 50, and for people under 50, the death rate is gradually increasing (IHME 2013).

Myocardial ischemia is one of the most common cardiovascular diseases (AHA 2013), and occurs when blood supply to cardiac muscle is impaired due to complete or partial blockage of coronary arteries. Preclinical experiments in myocardial ischemia have relied heavily upon mouse models of the disease. The mouse species is a popular animal model due to its low cost, short reproductive cycle, and its utility in studying the role of specific genes in the pathophysiology of myocardial ischemia via transgenic and knockout mice (Michael 1995, Yang 2000). Due to its small size and rapid heart rate, quantification of mouse cardiac function is challenging using clinical ultrasound scanners (<10MHz) due to poor spatial and temporal resolution. Development of high frequency (“micro”) ultrasound system with transducers operating at 15-50MHz has enabled preclinical experiments in

mouse models by improving spatial and temporal resolution (Foster 2001, Foster 2009), and has been used for cardiovascular research (Lui 2007, Li 2007, 2008, 2011, Zhou 2003, 2004).

To demonstrate the utility of high frequency ultrasound in small animal imaging, I will explore several novel approaches to quantifying cardiac function in mouse models of myocardial ischemia and infarction. This dissertation is organized as follows:

In Chapters 2 and 3, a 3-dimensional (3D) mathematical model of left ventricular myocardial infarction is developed by enforcing near incompressibility. Mathematical models of varying complexity have proven useful in fitting and interpreting regional cardiac displacements obtained from imaging methods such as ultrasound speckle tracking (Wang 2010). Simpler models, such as the classic thick-walled cylinder model of the left ventricle (LV) (Guccione 1991), solve quickly and are easy to implement, but they ignore regional geometric variations and are difficult to adapt to the study of regional pathologies such as myocardial infarction. Complex, anatomically accurate finite-element models work well but are computationally intensive and require specialized expertise to operate accurately (Herz 2005; Ingrassia 2007). I developed a kinematic model that offers a compromise between these two traditional approaches, assuming only that displacements in the left ventricle are polynomial functions of initial position and that the myocardium is approximately incompressible, while allowing myocardial motion to vary spatially as would be anticipated in an ischemic or dyssynchronous left ventricle.

Building a 3D mathematical model of the mouse LV requires a finely sampled matrix of 3D heart motion vectors. The capability to track 2D components of 3D displacement within each 2D B-mode image acquisition can be obtained using conventional speckle tracking (Li 2007). However, 3D displacement components are of significantly greater value since they can more accurately capture complex, out of plane, motion (such as twisting and basal-apical shortening). High spatial and temporal resolution displacement fields describing the mouse left ventricle can be reconstructed by combining two finely sampled stacks of 2D images acquired orthogonal to one another. Using orthogonal 2D image stacks allows X, Y and Z direction displacement vectors to be quantified. Further discussion of 3D motion reconstruction from orthogonal 2D images is outlined in Chapter 2.

Mathematical modeling also provides an alternative method to correct motion discrepancies due to ultrasound signal artifacts. This is particularly useful in the imaging of small animals using ultrasound, where signal dropout, attenuation and anatomical related artifacts (e.g. multi-path reverberation) can degrade image quality. Using high order polynomial functions to model myocardial motion provides significant leverage in capturing high degrees of motion variability, particularly in the infarcted heart. I derive a kinematic model describing myocardial deformation using a classic cylindrical model, assumed myocardial incompressibility and actual heart geometry. This formulation allows more freedom in describing cardiac motion but retains the incompressibility of myocardium as a constraint on the fitted

displacement field. A detailed discussion of this kinematic model of the left ventricle using near incompressibility is examined in Chapter 3.

Ultrasound methods have widely been used for quantifying left ventricular function due to their portability, inexpensive nature and non-invasive quality. Myocardial function is highly complex, and a number of ultrasound indices have been developed to describe complex myocardial motion, particularly left ventricular dyssynchrony (Li 2008, Li 2011). Significant numbers of studies on cardiac wall motion assessment are performed using ultrasound (Gorcsan 2005, Suffoletto, 2006).

In Chapter 4, new metrics for quantification of left ventricular dyssynchrony and infarct size using ultrasound displacement and strain data, respectively, are developed. Using these metrics, myocardial contractile dysfunction was quantified in inducible nitric oxide synthase knockout mice to demonstrate improved function after myocardial infarction compared to control, wild type mice.

Inducible nitric oxide synthase (iNOS) plays an important role in left ventricular remodeling and dysfunction after myocardial ischemia. Studies have reported that lack of nitric oxide (NO), achieved via iNOS gene knockout, is beneficial to heart function after ischemia in mice (Guo 1999; Sam 2001; Feng 2001; Li 2003; Lui 2005). A metric for estimating infarct size using ultrasound radial strain data is validated using late gadolinium enhancement (LGE) magnetic resonance imaging (MRI). Radial strain data, derived from high-resolution ultrasound images is used to detect and quantify infarct zones in the ischemic mouse model. A novel displacement-based dyssynchrony metric, referred to as

“Dyskinesia Index” (DI), is developed for detecting LV dyssynchrony, particularly dyskinesia. Myocardial remodeling and function are assessed using ultrasound periodically for a month after myocardial infarction (MI) in both iNOS knockout (KO) and wild type (WT) control mice. Further description of this work is examined in Chapter 4.

Another benefit of ultrasound is the ability to perform molecular imaging using molecularly targeted microbubbles. Ultrasound contrast agents are micron-size microbubbles that are injected intravenously and circulate in the bloodstream. In Chapter 5, molecularly targeted ultrasound contrast agents are demonstrated to identify previously-ischemic regions of the myocardium by virtue of specific cell adhesion molecules that are displayed on activated endothelial surfaces in response to ischemia/reperfusion injury.

Molecularly targeted ultrasound microbubbles possessing specific ligands selectively adhere, via ligand-receptor pairing, on the endothelial wall in regions of the myocardium previously subjected to ischemia/reperfusion injury (Davidson 2012; Kaufmann 2007). Current methods for detecting targeted microbubbles rely on waiting for unbound microbubbles to clear out of systemic circulation after an initial bolus. However, using this method, the dynamics of microbubble interaction with endothelial surface receptors cannot be realized due to initial microbubble saturation that causes acoustic shadowing (Schlosser 2003). A method for injecting microbubbles via constant infusion is shown to reduce acoustic signal shadowing when characterizing time intensity curves for ultrasound contrast agents. Furthermore, antibodies were conjugated to the microbubble surface, in

single- or dual-targeted fashion, to test the efficacy of binding to endothelial receptors after ischemia/reperfusion injury.

In Chapter 6, a model for human arterial wall motion is presented with *in vivo* validation. Arterial stiffness has been shown to be a predictor of cardiovascular events and has been shown to be correlated with clinical outcomes. The ability to measure changes in the mechanical properties of an arterial vessel wall may enable detection of early manifestations of cardiovascular disease. In this study, motion of the human common carotid arteries is examined.

In Chapter 7, a novel motion tracking method is presented by using the monogenic signal. Motion tracking via the monogenic signal is a phase-based displacement estimation technique. It is an improved alternative to conventional block-matching techniques as it makes use of image signal phase information, and is also computationally inexpensive and accurate.

Finally, Chapter 8 provides a summary of my dissertation in high frequency mouse imaging works with discussion on future developments.

# **Chapter 2: 3D Displacement Measurements of Mouse Left Ventricle Using Orthogonal Sets of 2D B-Mode Ultrasound Images.**

## **2.1 INTRODUCTION**

Noninvasive medical ultrasound imaging has become an indispensable tool in assessing myocardial mechanics and function in patients with myocardial infarction (MI). The mouse species provides a well characterized, and widely accepted, model for conducting basic cardiovascular research into the evolution of disease (Nahrendorf 2003) and response to experimental therapy (Harding 2001). Consequently, there is significant value in the comprehensive and non-invasive quantification of mouse left ventricular (LV) function. Unfortunately, due to the technical challenges in high resolution ultrasound, the vast majority of assessments of LV function in mice rely on M-mode or single-slice 2D analyses, whereas the actual myocardial motion is complex and 3 dimensional.

While real-time 3D data of high resolution ultrasound is challenging to acquire, 3D motion can be estimated from sequences of 2D data encompassing the entire length of the LV. 3D myocardial function has been estimated from 2D B-mode images using multiple short-axis (SA) cines acquired along the base-to-apex axis of the human LV (Lee 2008), where out of plane motion was estimated using LA cines. Through plane motion estimation has been attempted using orthogonal displacement measurements and radio frequency (RF) signal decorrelations between A-lines (Garson 2008). Correlation-based 3D speckle tracking (Chen

2005), spatio-temporal non-rigid image registration (Elen 2008), and tracking using sum of absolute difference algorithm (Crosby 2009) on 3D ultrasound data have also been investigated. These 3 techniques were tested using simulated 3D ultrasound data, and methods for acquiring human 3D LV data are still being refined. 3D tracking of the endocardial wall has been used in humans to calculate LV volume, and has been validated with magnetic resonance imaging (Nesser 2009). We have developed an approach for reconstructing 3D motion, throughout the mouse LV, that combines orthogonal stacks of 2D imaging planes with mouse heart mathematical model fitting to arrive at a finely sampled 3D displacement mapping through the entire heart cycle.

## **2.2 METHODS**

The animal experiments in this study conformed to a protocol approved by the University of Virginia Animal Care and Use Committee. Four C57BL/6 mice were scanned at baseline and 2 days after MI using a Vevo2100 (VisualSonics, Toronto, Canada) scanner with a MS400 30 MHz linear array transducer. The transducer has a spatial resolution of 50  $\mu\text{m}$  axially and 110  $\mu\text{m}$  laterally (Foster 2009). Parallel SA cines of the LV were acquired sequentially at 0.5mm intervals from apex to base. The transducer was rotated exactly 90° within a pivoting mount and serial long-axis (LA) cines were acquired at 0.5 mm intervals from the lateral to septal wall. Approximately 10-12 SA slices and 6-8 LA slices were acquired across the entire LV. A schematic of SA and LA orientation is shown in Figure 2.1. For

clarity, only 5 each of the SA and LA slices are shown near the center of the heart. In this rendering, the endocardial surface is indicated in red and the epicardial surface is indicated in yellow.

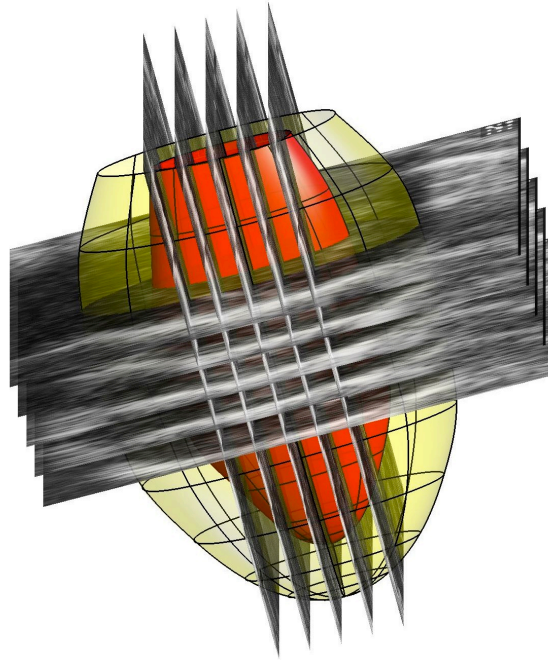


Figure 2.1: Acquisition and orientation of SA and LA cines. The endocardial wall surface is shown in red and the epicardial surface in yellow. Only the slices near the center of the LV are shown for illustrative purposes. Intervals between each SA and LA slices are 0.5mm.

Excluding the time spent on mouse preparation, the time spent acquiring SA and LA cines was less than 5 minutes. During scanning, body temperature was maintained at  $37\pm 0.2^{\circ}\text{C}$  with the aid of a digital rectal thermometer, a heated plate on which the animal lay, and an external lamp heat source. A constant body temperature was important in maintaining consistent heart rates ( $439\pm 23$  bpm and

581±64 bpm for normal and post-infarct hearts, respectively) during data acquisition. This ensured proper registration of displacement data between different SA and LA images through time. Scan settings were optimized and maintained through the study to achieve a frame rate at approximately 350 Hz. Approximately 40-50 frames per heart cycle were collected for mice at baseline, and 35-45 frames per heart cycle for post-infarct mice.

For each SA and LA cine, myocardial displacement was obtained by speckle tracking with approximately 0.2 mm x 0.2 mm pixel blocks using a 2D minimum sum of absolute differences algorithm (Li 2007). In regions experiencing image artifacts or signal dropouts, a kinematic model of the heart was applied (Lin 2011), and motion was corrected based on a weighted average of tracked motion and model predicted values. Briefly, the kinematic model used polynomial functions to fit longitudinal and circumferential motion derived from speckle tracking. The derivatives of these functions are then employed to determine radial motion using a myocardial incompressibility assumption (Judd 1991). The kinematic model is useful in estimating and correcting motion in regions that are severely degraded with image artifact and regions near the endocardial surface where tracked myocardial motion can be perturbed by blood motion.

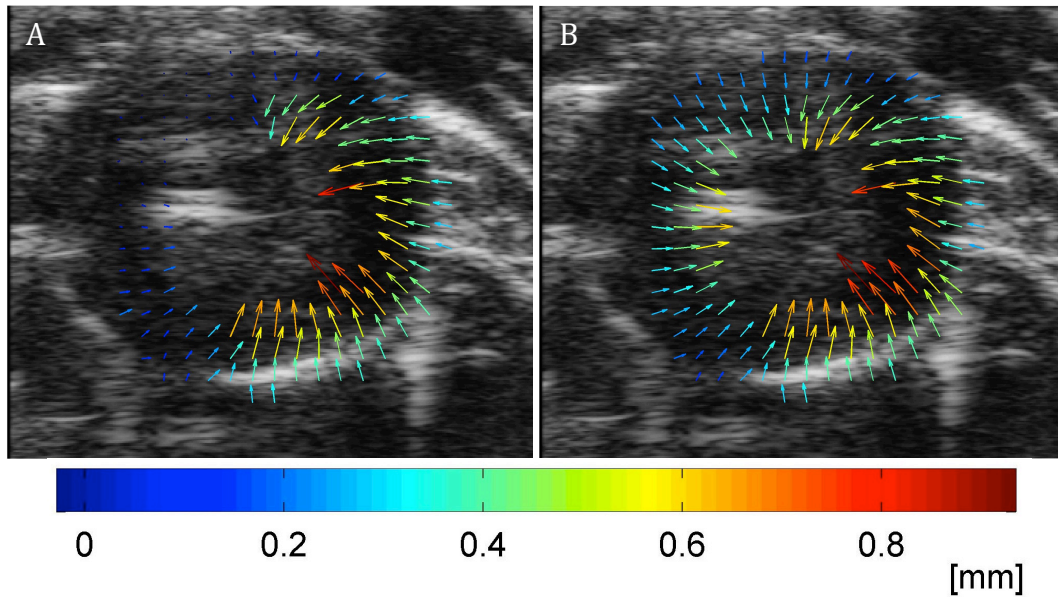


Figure 2.2: Displacement field derived from speckle tracking for an SA image with severe image artifact. In this example, the anteroseptal region of the LV is shadowed by reverberation from sternum. (A) Speckle tracking of raw displacement data illustrates absence of displacement arrows in the region shadowed by the sternum. (B) Full displacement field obtained after applying the LV kinematic model.

In mouse heart imaging, reverberation from the sternum and ribs is a common source of image artifact. Since the sternum is static, the reverberation signals from the sternum show up as a high intensity static image feature overshadowing the dynamic motion of the heart underneath. Reverberation artifacts can be filtered using a principal component analysis based filter that exploits the fact that reverberation signal in this case is static and the myocardium is dynamic (Mauldin 2011). However, in cases where severe reverberations are

present, the filter can degrade the myocardial signal, and result in poor tracking. In these cases, a mathematical model is therefore preferred to estimate displacement. Figure 2.2 shows an SA image where the anteroseptal region of the heart is overshadowed by severe reverberation from the sternum. In Figure 2.2A, raw displacement data from end-diastole (ED) to end-systole (ES) using speckle tracking exhibited little or no motion in this region, however, motion of the endocardial wall coming in and out of the artifact can be observed on the cine sequence. In Figure 2.2B, motion in the anteroseptal region is corrected using the kinematic model, while motion in other regions is preserved as determined from speckle tracking. The kinematic model is also important in proper registration of SA and LA data, as explained in the following paragraph.

Lateral and axial displacements in the SA data correspond to motion in the X and Y directions, respectively, while lateral and axial displacements in the LA reveal motion in the Z and Y directions, respectively. SA and LA data shared displacement information in the axial (Y) direction. Registration of SA and LA slices is performed by optimizing the correlation between axial displacements at the intersection points. Figure 2.3 shows the correlation between axial displacements derived from SA and LA data. Data near the apex, corresponding to displacement values near zero, are more dispersed due to higher error in tracking data. The inclusion of kinematic model is also important in improving correlation between axial displacement in SA and LA images. From observation, the reverberation artifact is more prevalent in SA images than it is in LA images. The presence of the

artifact yields low correlation between axial displacements from SA and LA data resulting in higher tracking errors. Using the kinematic model, displacement estimates corrupted by imaging artifact is retrieved using displacements obtained in adjacent artifact-free regions and exploiting the incompressible tissue characteristic encompassed within the model. By registering SA and LA data, 3D displacement data are compiled using SA lateral displacement for the X component, LA lateral displacement for the Z component, and the average of shared axial displacement for the Y component.

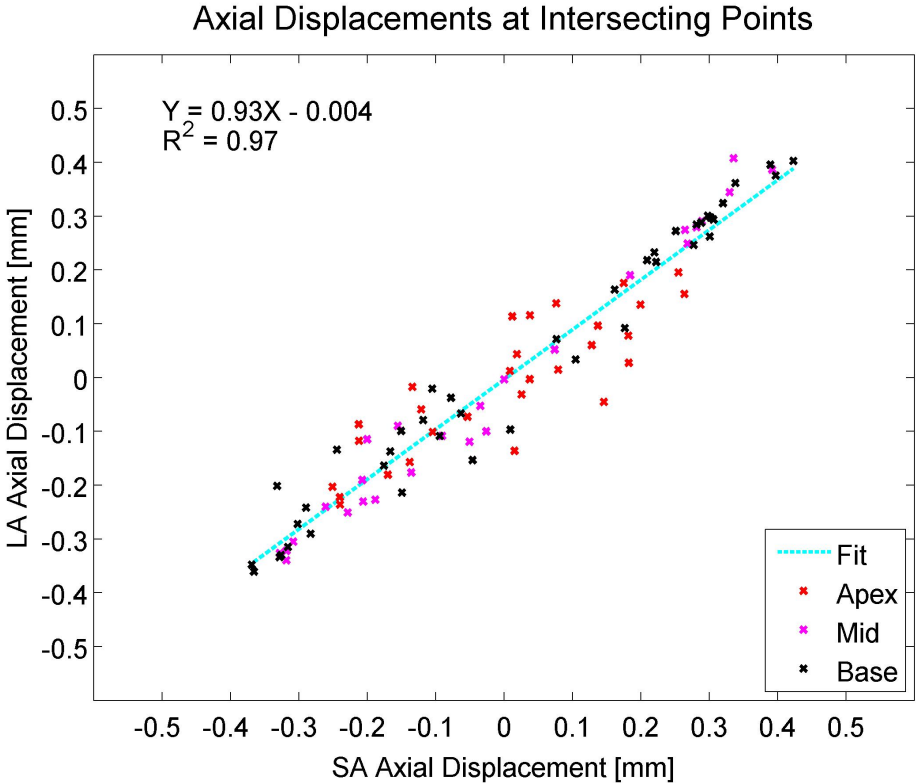


Figure 2.3: The scatter plot above shows the correlation between axial displacements from SA and LA data at intersection points. Displacements near the in the apex are more disperse.

3D Displacement error was computed based on the ratio of the length of final displacement vector, through the entire heart cycle (Li 2008), to the length of the trajectory (i.e. scalar distance traversed). For a complete cardiac cycle, from ED to ES and back to ED, the final displacement should be zero. (This requires that respiratory-related abdominal displacements are “gated out” during the acquisition process.)

## **2.3 RESULTS**

Figure 2.4 shows 3D trajectory of points in the entire LV myocardium. The trajectory is velocity coded, where each red and green segment represents the distance traveled between 2 frames (approximately 6 ms). While the magnified view of the trajectory shows that the starting point and ending point (ED to ED cardiac cycle) of the path are not the same, the distance between them is small. The tracking displacement error is  $8.4 \pm 1.4\%$ . Most of the tracking error originates at the apex due to out of plane motion, and regions near the endocardial and epicardial walls, where blood and surrounding tissue motion can interfere with myocardium tracking. A reduced displacement error ( $5.6 \pm 1.2\%$ ) is observed when displacement data is corrected using the kinematic model.

Displacement components in polar coordinate system at different levels of the LV are illustrated in Figure 2.5. Average displacement for the first 2 basal slices are plotted for the basal section, the middle 2 slices for the mid-ventricular section, and the last 2 slices for the apical section. The black curves in Figure 2.5 show the

displacements in a healthy mouse heart. It can be observed in the third column that longitudinal motion at the base is the largest, it then decreases through the mid-ventricular section, and reverses in direction at the apex. This motion pattern corresponds to longitudinal shortening during LV contraction from ED to ES. Data for Day-2 post infarcted mice are shown in red curves. Displacement magnitudes decreased significantly at Day-2. Displacements taken at the anterolateral region, the infarct zone, reveal that radial, circumferential and longitudinal motion are decreased by  $45.1\pm 9.8\%$ ,  $43.5\pm 8.2\%$ , and  $52.4\pm 9.2\%$ , respectively. Additionally, a delay in time to peak displacement,  $11.2\pm 3.4$  ms, in the radial component is also observed in the infarcted heart.

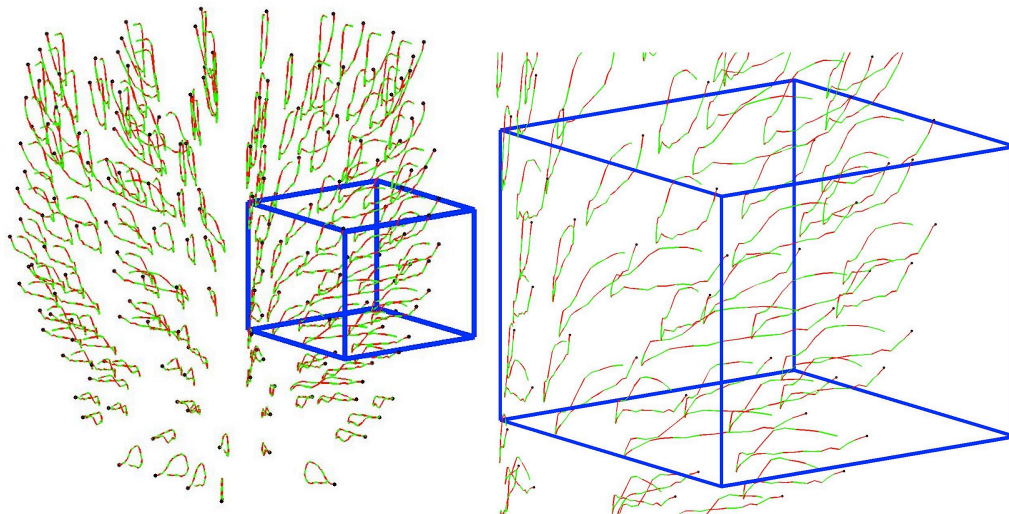


Figure 2.4: 3D trajectory the points in the LV. Magnified view of region in the cube on the right shows loops that are not completed enclosed, this corresponds to the error in tracking. Each red and green segment represents the distance traversed in every 2 frames.

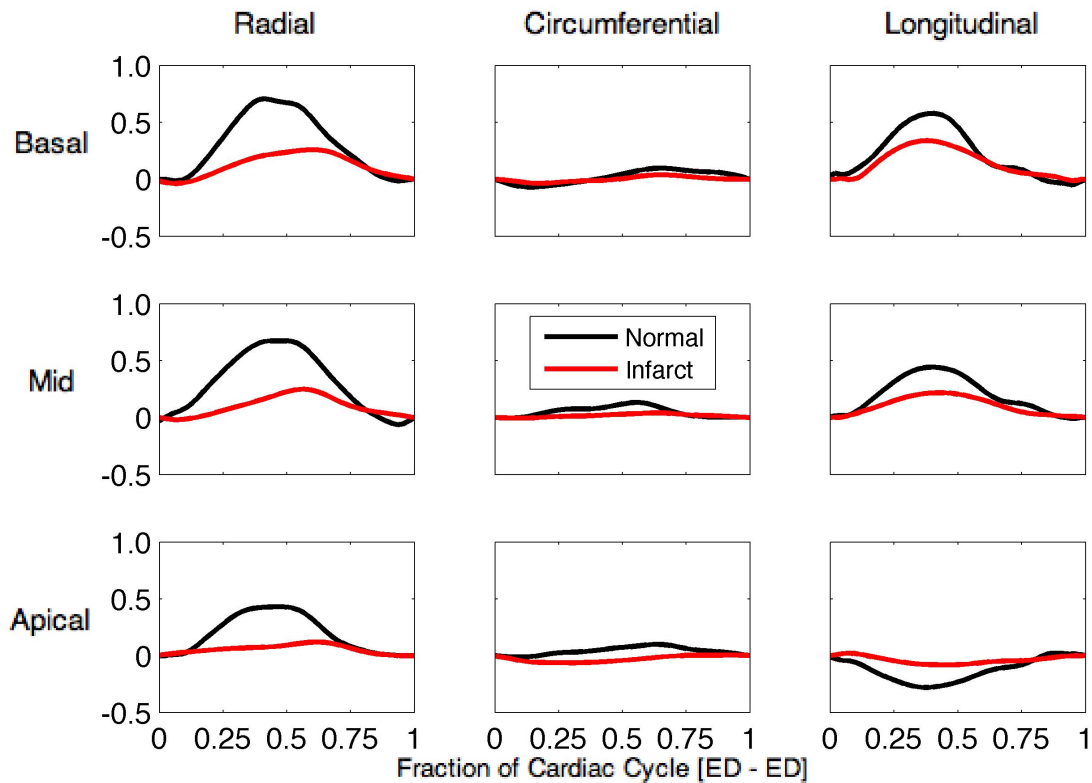


Figure 2.5: Displacement components in the basal (top row), mid (middle row), and apical (bottom row) regions of the LV. Contrasts between displacement from normal (black curves) and infarcted (red curves) hearts are shown. Unit is in millimeter.

## 2.4 DISCUSSION

A method for reconstructing 3D displacement data from orthogonal stacks of 2D images has been presented. Comprehensive 3D analyses of cardiac displacements provide a more thorough assessment of infarcted LV. Using 3D displacement data, measurements of torsion, twist, and strain, including principal

and shear strains, can be calculated using a finite element method. This can provide clearer delineation of infarct zone and its relative size with respect to the size of the LV.

The inclusion of a kinematic model was important in improving displacement estimates, especially in data corrupted by acquisition related artifacts. It should be noted that the current kinematic model is limited to the healthy mouse LV. The framework can be extended for diseased hearts. Due to the presence of dyssynchronous and highly dissimilar regional motion, higher order polynomials or other forms of function may be necessary for fitting circumferential and longitudinal motions in order to describe the intricate coupled motion in the radial direction.

# Chapter 3: Kinematic Model for Deformation of the Infarcted Mouse Left Ventricle Incorporating A Near-Incompressibility Constraint

## 3.1 INTRODUCTON

Despite significant achievements being made in diagnosing and treating cardiovascular disease (CVD), it remains a major global health concern. In the United States, heart disease is the leading cause of death, accounting for 32.3% of all deaths in 2009 (Roger 2013). Ultrasound is routinely used to diagnose patients with suspected heart disease, including Doppler-based ultrasound such as Tissue Doppler Imaging assessing cardiac function based on myocardial velocities (Sutherland 1994; Sebag 2005), and M-mode echocardiography to analyze the time delay between septal and posterior wall motion (Pizalis, 2005). Post image formation techniques using B-mode ultrasound images, such as speckle tracking, can assess myocardial mechanics using regional tissue tracking (Li 2007; Nesser 2009). These measurements are important to the understanding of normal heart function and CVD. However, motion estimates using speckle tracking techniques are often noisy (Bansal 2008; Hjertaas 2013). For example, in mouse heart imaging, high heart rate (400 – 600 bpm) and out of plane motion can result in significant decorrelation between frames. In small animal imaging, relatively low spatial resolution is a major concern, especially in motion tracking applications. Recent advances in high frequency ultrasound have made it possible to capture high frame rate cine sequences with of approximately 50  $\mu\text{m}$  axial and 110  $\mu\text{m}$

lateral spatial resolutions (Foster 2009). Additionally, signal dropout, attenuation and anatomically related artifacts (e.g., sternum, rib or lung related multipath reverberation or shadowing) can degrade image quality. To partially compensate for these artifacts, several groups have developed image processing techniques that include clutter and artifact reduction using finite impulse response (FIR) filters (Lediju 2009) and principal component analysis (Gallippi 2002; Mauldin 2011).

Another approach to compensate for artifacts in cardiac motion estimation is the use of mathematical models. Using this approach, mathematical models can operate as filters by imposing geometric constraints on allowed myocardial motion. This can be used to discard and correct improbable motion estimates derived from motion tracking techniques. For example, models using tissue incompressibility as a constraint have been used to improve both automated segmentation (Hansegard 2007; Garson 2008; Zhu 2007; Zhu 2010) and motion estimation (Bistoquet 2008; Mansi 2010; Touil 2010; Wang 2010).

Models using simple geometric shapes appropriate to the LV have been influential in studying cardiac mechanics. Cylindrical models have been used to predict distributions of stress and strain around the myocardium (Humphrey 1989; Costa 1996), and to estimate material properties of the myocardium (Guccione 1991). While these models have been instrumental in understanding ventricular mechanics, they are generally assumed to represent only a mid-ventricular section of the LV and are inadequate for modeling the apical region. In addition, they frequently assume that deformation is axisymmetric, limiting their application in

applications involving, for example, myocardial infarction, where ventricular remodeling and dyssynchrony give rise to substantial regional variation in cardiac deformation. Other models using prolate spheroidal and realistic heart geometries have had better success in describing motion near the apex as well as regional ischemia and dyssynchrony (Arts 1992; Kerckhoffs 2009). However, increasing anatomic fidelity in such models comes at the cost of steeply increasing computation time and the need to employ highly specialized modeling software, limiting their routine use in fitting and interpreting imaging data. In this paper, I derive a kinematic model in cylindrical polar coordinates. The models allow radial ( $r$ ), circumferential ( $\theta$ ) and longitudinal ( $z$ ) displacements to vary as polynomial functions of initial position  $R$ ,  $\theta$ , and  $Z$  within a realistic initial geometry, incorporating the additional constraint of near incompressibility within the myocardium. This formulation allows more freedom in describing cardiac motion while retaining the advantages of enforcing incompressibility in enhancing physical consistency of the reported displacements. The myocardial incompressibility property is an important constraint. While blood flow through the myocardium can change myocardial volume during the cardiac cycle, the change is less than 4% (Judd 1991). By invoking the incompressibility constraint, analytic mathematical models become tractable and can be used to describe myocardial deformation.

## 3.2 METHODS

### 3.2.1 Mouse Heart Imaging and Motion Estimates

Our mathematical heart model was validated using *in vivo* ultrasound mouse data. The animal experiments in this study followed a protocol approved by the University of Virginia Animal Care and Use Committee. Short-axis (SA) and long-axis (LA) cine B-mode images of 6 healthy male C57BL/6 mice (10- to 12-wk old, 24 to 26 g) were acquired using a VisualSonics Vevo 2100 scanner (Toronto, Ontario, Canada) with a MS400 transducer operating at 30 MHz, with 50  $\mu\text{m}$  axial and 110  $\mu\text{m}$  lateral resolutions (Foster 2009). Imaging frame rate was approximately 350 fps, and the average heart rate of mice under anesthesia was  $462 \pm 14$  bpm. Electrocardiogram (ECG) signals were obtained by taping mouse limbs with electrically conductive cream to ECG electrodes integrated into a heating platform. To achieve this frame rate, frame of view (FOV) is approximately 7mm x 7mm with standard line density and a single focal zone centered at the mouse left ventricle. During scanning, the mouse was carefully maintained under anesthesia using isoflurane at approximately 1.5 – 1.8% mixed with atmospheric air. Body temperature was maintained at  $37 \pm 0.2^\circ\text{C}$  by a heated platform under the animal and an incandescent lamp, and the body temperature monitored with the aid of a digital thermometer. A constant body temperature was important in maintaining a consistent heart rate. Serial SA images were acquired at 0.5 mm intervals, with 10 to 12 slices throughout the LV, and 6 to 8 LA images of the LV were acquired for each mouse. All mice underwent myocardial infarction (MI) via 1-hour occlusion of

the left anterior descending (LAD) coronary artery followed by reperfusion (Yang 2002). Post-infarct mice were assessed using ultrasound 28 days after MI with the same acquisition parameters (1 mouse died after surgery, and another mouse was excluded due to poor ultrasound data). Average heart rate for MI mice was  $561 \pm 54$  bpm. Displacement fields across the myocardium were determined by speckle tracking with approximately  $0.2 \text{ mm} \times 0.2 \text{ mm}$  pixel block size using a minimum sum absolute difference (MSAD) algorithm and parabolic fit-based sub-pixel resolution (Li 2007). The MSAD algorithm provides approximately equivalent performance to more computationally intensive tracking algorithms (e.g. normalized cross correlation) in representative B-Mode images (including realistic levels of noise) (Friemel 1995). However, MSAD is based on absolute signal difference and is more susceptible to image degradation, particularly at signal to noise ratio (SNR) less than 5 dB.

### ***3.2.2 Myocardial Incompressibility***

The myocardium is generally assumed to be nearly incompressible, since it is composed of 80% water (Aliev 2002; Vinnakota 2004). This assumption is supported by studies showing that changes in cardiac muscle volume due to movement of blood into and out of the coronary blood vessels during the cardiac cycle are less than 4% (Judd 1991). The change in volume is even smaller in ischemic regions of the heart, since blood perfusion and motion in these regions are limited. I considered two different approaches to enforcing incompressibility: a simple model for normal hearts in which incompressibility is assumed in order to

derive an analytic expression for radial deformation as a function of circumferential and axial deformation; and a more general approach where the incompressibility constraint is weighted against measured displacements to achieve a balance between enforcing incompressibility and matching measured deformation.

### 3.2.3 General Model Formulation

I began with a general description of deformation of the heart from end systole (ES) to end diastole (ED) in cylindrical coordinates as expressed in Equation (1), where  $(R, \Theta, Z)$  are (radial, circumferential, longitudinal) undeformed myocardial positions at ES, and  $(r, \theta, z)$  are deformed myocardial positions at ED (Adkins 1955).

$$r = r(R, \Theta, Z), \theta = \theta(R, \Theta, Z), \text{ and } z = z(R, \Theta, Z) \quad (1)$$

In cylindrical polar coordinates, the deformation gradient matrix,  $F$ , describing deformation from ES to ED is then (Spencer 1980):

$$F = \begin{bmatrix} \frac{\partial r}{\partial R} & \frac{1}{R} \frac{\partial r}{\partial \Theta} & \frac{\partial r}{\partial Z} \\ r \frac{\partial \theta}{\partial R} & \frac{r}{R} \frac{\partial \theta}{\partial \Theta} & r \frac{\partial \theta}{\partial Z} \\ \frac{\partial z}{\partial R} & \frac{1}{R} \frac{\partial z}{\partial \Theta} & \frac{\partial z}{\partial Z} \end{bmatrix} \quad (2)$$

For an incompressible material the determinant of the deformation gradient matrix is equal to unity:

$$\frac{r}{R} \left[ \begin{aligned} & \left( \frac{\partial r}{\partial R} \frac{\partial \theta}{\partial \Theta} \frac{\partial z}{\partial Z} \right) + \left( \frac{\partial r}{\partial \Theta} \frac{\partial \theta}{\partial Z} \frac{\partial z}{\partial R} \right) + \left( \frac{\partial r}{\partial Z} \frac{\partial \theta}{\partial R} \frac{\partial z}{\partial \Theta} \right) \\ & - \left( \frac{\partial r}{\partial R} \frac{\partial \theta}{\partial Z} \frac{\partial z}{\partial \Theta} \right) - \left( \frac{\partial r}{\partial \Theta} \frac{\partial \theta}{\partial R} \frac{\partial z}{\partial Z} \right) - \left( \frac{\partial r}{\partial Z} \frac{\partial \theta}{\partial \Theta} \frac{\partial z}{\partial R} \right) \end{aligned} \right] = v = 1 \quad (3)$$

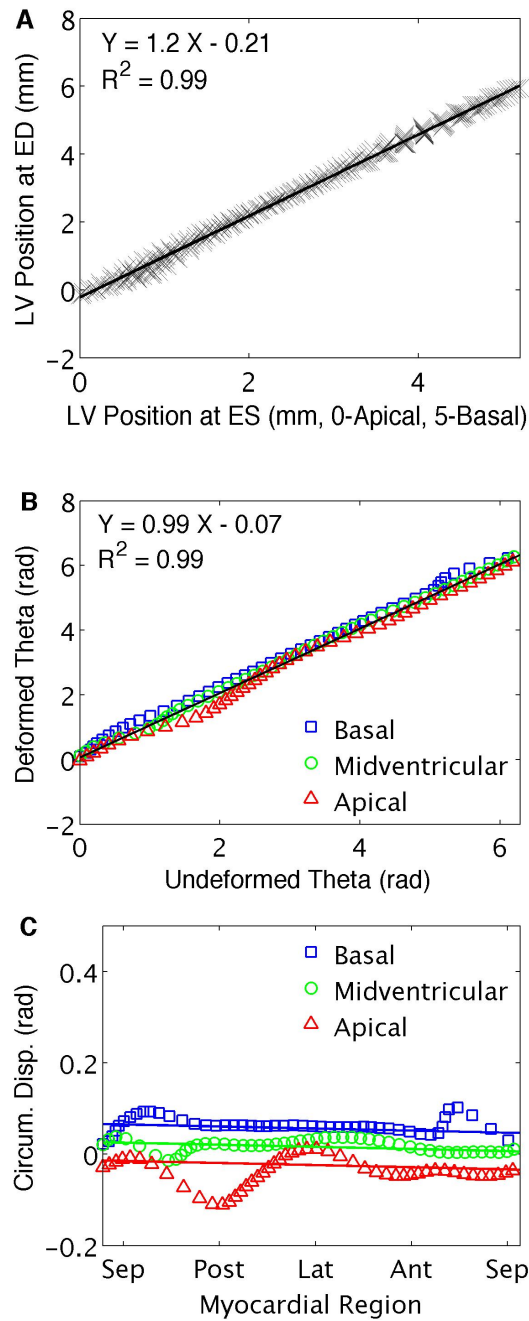


Figure 3.1: Linear regression of LV deformed longitudinal (A) and circumferential (B) positions and circumferential displacement (C) in a representative normal mouse heart. LV extension (slope > 1.0 in panel A) and torsion (different signs of mean circumferential displacement in panel C) are apparent in both raw and fitted data.

Cylindrical models of the left ventricle generally assume an axisymmetric initial geometry and a simple form for the functions  $r$ ,  $\theta$ , and  $z$  in Equation (1), such that most of the partial derivatives in the deformation gradient matrix are either zero or constant. Seeking a more general formulation, I plotted measured deformed versus undeformed positions from the mouse hearts I studied and sought the simplest polynomial functions that adequately described regional variations in deformation in both control and infarcted hearts.

### **3.2.4 Linear Model of Deformation in the Normal Mouse Heart**

For normal mouse hearts, deformed longitudinal position  $z$  was a linear function of undeformed longitudinal position  $Z$  but independent of  $R$  or  $\Theta$  (Figure 3.1A). Deformed circumferential position  $\theta$  was a nearly linear function of undeformed circumferential position  $\Theta$  and independent of  $R$ , but did vary with undeformed longitudinal position  $Z$  (Figure 3.1B). Accordingly, I used the following first-order polynomial functions to describe circumferential and longitudinal motion, respectively:

$$\theta(\Theta, Z) = a\Theta + \tau Z + b, \text{ and } z(Z) = cZ + d \quad (4)$$

Since the derivatives of  $\theta$  and  $z$  are independent of  $R$  and  $\Theta$ , respectively, I can simplify the deformation matrix in (2) to (5):

$$F = \begin{bmatrix} \frac{\partial r}{\partial R} & \frac{1}{R} \frac{\partial r}{\partial \Theta} & \frac{\partial r}{\partial Z} \\ r \frac{\partial \theta}{\partial R} & \frac{r}{R} \frac{\partial \theta}{\partial \Theta} & r \frac{\partial \theta}{\partial Z} \\ \frac{\partial z}{\partial R} & \frac{1}{R} \frac{\partial z}{\partial \Theta} & \frac{\partial z}{\partial Z} \end{bmatrix} = \begin{bmatrix} \frac{\partial r}{\partial R} & \frac{1}{R} \frac{\partial r}{\partial \Theta} & \frac{\partial r}{\partial Z} \\ 0 & \frac{r}{R} \frac{\partial \theta}{\partial \Theta} & r \frac{\partial \theta}{\partial Z} \\ 0 & 0 & \frac{\partial z}{\partial Z} \end{bmatrix} \quad (5)$$

Similarly, Equation (3) can be simplified to (6):

$$\det(F) = \left( \frac{\partial r}{\partial R} \right) \left( \frac{r}{R} \frac{\partial \theta}{\partial \Theta} \right) \left( \frac{\partial z}{\partial Z} \right) = 1 \quad (6)$$

By integrating Equation (6) I arrive at an expression for the deformed radius at any point:

$$r(R, \Theta, Z) = \sqrt{\frac{R^2 - R_0^2}{f(\Theta, Z)} + r_0^2}, f(\Theta, Z) = \left( \frac{\partial \theta}{\partial \Theta} \right) \left( \frac{\partial z}{\partial Z} \right) = ac \quad (7)$$

where  $R_0$  is the undeformed endocardial radius and  $r_0$  the deformed endocardial radius.

To optimize these constants, the normalized root mean square error (NRMSE) between observed,  $(r_i, \theta_i, z_i)$ , and predicted,  $(\hat{r}_i, \hat{\theta}_i, \hat{z}_i)$ , positions after deformation is calculated, where  $i$  denotes the  $i^{\text{th}}$  observation, where  $i$  denotes the  $i^{\text{th}}$  observation:

$$NRMSE = \frac{1}{3\sqrt{n}} \sum_{i \in (r, \theta, z)} \frac{\sqrt{\sum_i^n (t_i - \hat{t}_i)^2}}{t_{\max} - t_{\min}} \quad (8)$$

The combination of parameter values that yields the minimum NRMSE are considered optimal:

$$(a, b, c, d, \tau) = \arg \min(NRMSE(a, b, c, d, \tau)) \quad (9)$$

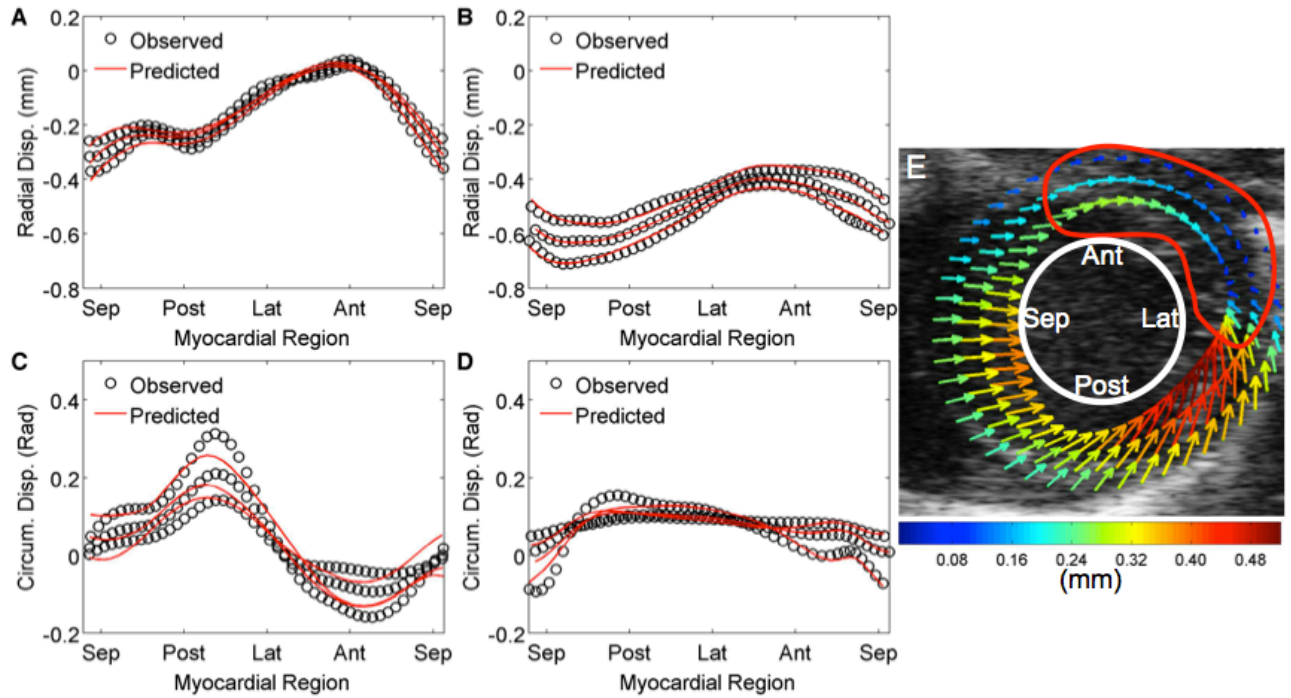


Figure 3.2: Radial (panels A and B) and circumferential (panels C and D) observed (circles) and polynomial model predicted (triangles) displacement of points throughout the myocardium as derived from speckle tracking using SA B-mode images for infarcted (panels A and C) and normal (panels B and D) hearts. X-axes in panels A and B are myocardial position in SA view as defined in panel E. Region in the enclosed red contour is the infarcted zone, with minimal radial displacement and clockwise circumferential motion.

### 3.2.5 Polynomial Model of Deformation in Normal and Infarcted Mouse Hearts

Not surprisingly, given the regional nature of the insult, in infarcted mouse hearts I found substantial regional variations in displacements: radial and circumferential motion varied with radial, circumferential, and longitudinal position in the heart wall (Figure 3.2), while longitudinal motion varied significantly in the

circumferential and longitudinal directions only. Therefore, the deformation matrix in (2) could be simplified only slightly to (10), with the determinant expressed in (11):

$$F = \begin{pmatrix} \frac{\partial r}{\partial R} & \frac{1}{R} \frac{\partial r}{\partial \Theta} & \frac{\partial r}{\partial Z} \\ r \frac{\partial \theta}{\partial R} & \frac{r}{R} \frac{\partial \theta}{\partial \Theta} & r \frac{\partial \theta}{\partial Z} \\ \frac{\partial z}{\partial R} & \frac{1}{R} \frac{\partial z}{\partial \Theta} & \frac{\partial z}{\partial Z} \end{pmatrix} = \begin{pmatrix} \frac{\partial r}{\partial R} & \frac{1}{R} \frac{\partial r}{\partial \Theta} & \frac{\partial r}{\partial Z} \\ r \frac{\partial \theta}{\partial R} & \frac{r}{R} \frac{\partial \theta}{\partial \Theta} & r \frac{\partial \theta}{\partial Z} \\ 0 & \frac{1}{R} \frac{\partial z}{\partial \Theta} & \frac{\partial z}{\partial Z} \end{pmatrix} \quad (10)$$

$$\frac{r}{R} \left[ \left( \frac{\partial r}{\partial R} \frac{\partial \theta}{\partial \Theta} \frac{\partial z}{\partial Z} \right) - \left( \frac{\partial r}{\partial R} \frac{\partial \theta}{\partial Z} \frac{\partial z}{\partial \Theta} \right) - \left( \frac{\partial r}{\partial \Theta} \frac{\partial \theta}{\partial R} \frac{\partial z}{\partial Z} \right) + \left( \frac{\partial r}{\partial Z} \frac{\partial \theta}{\partial R} \frac{\partial z}{\partial \Theta} \right) \right] = \nu = 1 \quad (11)$$

I selected polynomials containing terms that captured the nature and polynomial order of observed variations:

$$\begin{aligned} r(R, \Theta, Z) &= R_c + \sum_{i=1}^m g_i R^i + \sum_{i=1}^n h_i \Theta^i + x_1 R \Theta + x_2 R^2 \Theta + x_3 R \Theta^2 + x_4 R^2 \Theta^2 + \nu_1 Z + \nu_2 \Theta Z \\ \theta(R, \Theta, Z) &= \Theta_c + \sum_{i=1}^m s_i R^i + \sum_{i=1}^n t_i \Theta^i + y_1 R \Theta + y_2 R^2 \Theta + y_3 R \Theta^2 + y_4 R^2 \Theta^2 + w_1 Z + w_2 \Theta Z \\ z(\Theta, Z) &= Z_c + u_1 \Theta + u_2 Z + u_3 \Theta Z \end{aligned} \quad (12)$$

For this more complicated model, I could not simply integrate to determine radial deformation as for the linear model. Instead, I obtained coefficients for Equation (12) for both control and infarcted hearts by minimizing mean square error (MSE) between measured and model deformations:

$$MSE = \frac{1}{n} \sum_{i=1}^n \left[ w_r (r_i - \hat{r}_i)^2 + w_\theta (\theta_i - \hat{\theta}_i)^2 + w_z (z_i - \hat{z}_i)^2 + w_\nu (1 - \hat{\nu}_i)^2 \right] \quad (13)$$

where  $w_r$ ,  $w_\theta$ ,  $w_z$ , and  $w_\nu$  are weighting factors for radial, circumferential, longitudinal and the incompressibility constraint, respectively. The weights sum to unity, and can be chosen based on the confidence of tracking accuracy in each direction, and the desired level of incompressibility (i.e. tolerance for volume

change during contraction).  $(r_i, \theta_i, z_i)$  are the actual displacement data and  $(\hat{r}_i, \hat{\theta}_i, \hat{z}_i)$  are the polynomial model-predicted values.

### 3.3 RESULTS

#### ***3.3.1 Linear Model of Deformation in the Normal Mouse Heart***

Longitudinal motion was obtained using lateral displacement data derived from tracking LA cine loops. The 0 mm-position was defined at the apex at ES. As shown in Figure 3.1A, tissues at the basal level moved upward relative to the apex, resulting in LV extension (slope of fitted line  $> 1.0$ ). Circumferential motion is illustrated in Figure 3.1B. The 0-rad reference was defined at the section between the papillary muscles, increasing in the counterclockwise direction. A shift in the  $\theta(\Theta)$  curve was observed at different levels of the LV. Using the midventricular layer as a reference, the basal and apical layers were observed to rotate in opposite directions, reflecting LV torsion. The small differences between deformation at the different axial levels shown in Figure 3.1B are more readily apparent when plotting predicted versus observed circumferential displacements (Figure 3.1C), as are small local variations about the linear fits within each short-axis section.

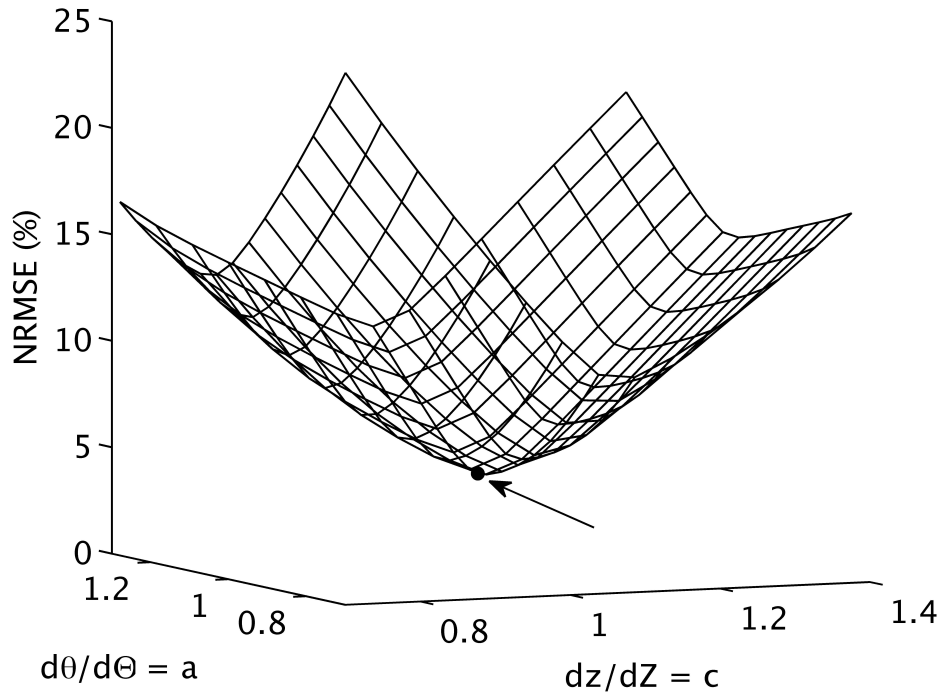


Figure 3.3: Linear model simulations for normal hearts using different combinations of  $a$  and  $c$ . The NRMSE is calculated for each simulation and the combination with the minimum NRMSE (*arrow*) represents the optimal parameter values.

The slope of the regression lines shown in Figure 3.1 provided an initial estimate of the coefficients  $a$  and  $c$  in the linear deformation model (Equations 4,7). I then simulated a range of values in the neighborhood of the regression coefficients  $a$  and  $c$ , and determined the combination that minimized NRMSE (Figure 3.3). I determined the remaining coefficients  $b$ ,  $d$ , and  $t$ , which do not affect model-predicted radius, from a best fit to the data using Equations (4) and optimized values for  $a$  and  $c$ . All coefficients were determined individually for each mouse. A statistical summary of the mean and standard deviation of the values for these coefficients is reported in Table 1.

**Table 1.** Optimized values for linear model parameters:

Parameter	Value
$a$	$1.03 \pm 0.12$
$b$	$-0.09 \pm 0.04$ rad
$c$	$1.12 \pm 0.08$
$d$	$-0.18 \pm 0.03$ mm
$r$	$-0.01 \pm 0.004$ rad/mm

The NRMSE of the optimized models was  $4.4 \pm 1.2\%$ , represented by the minimum value of the surface in Figure 3.3. Figure 3.4 shows predicted radial motion at different levels of the LV. The fact that the model captures radial motion throughout the normal mouse LV with a single choice of parameters for  $\partial\theta/\partial\Theta$  and  $\partial z/\partial Z$  suggests that most of the variation in radial motion in the normal mouse heart arises from spatial variation in geometry ( $R_0$  and  $r_0$  in Equation (7)). As shown in Figure 3.4C, the apical section contributes most of the error; this error near the apex is largely due to tracking error.

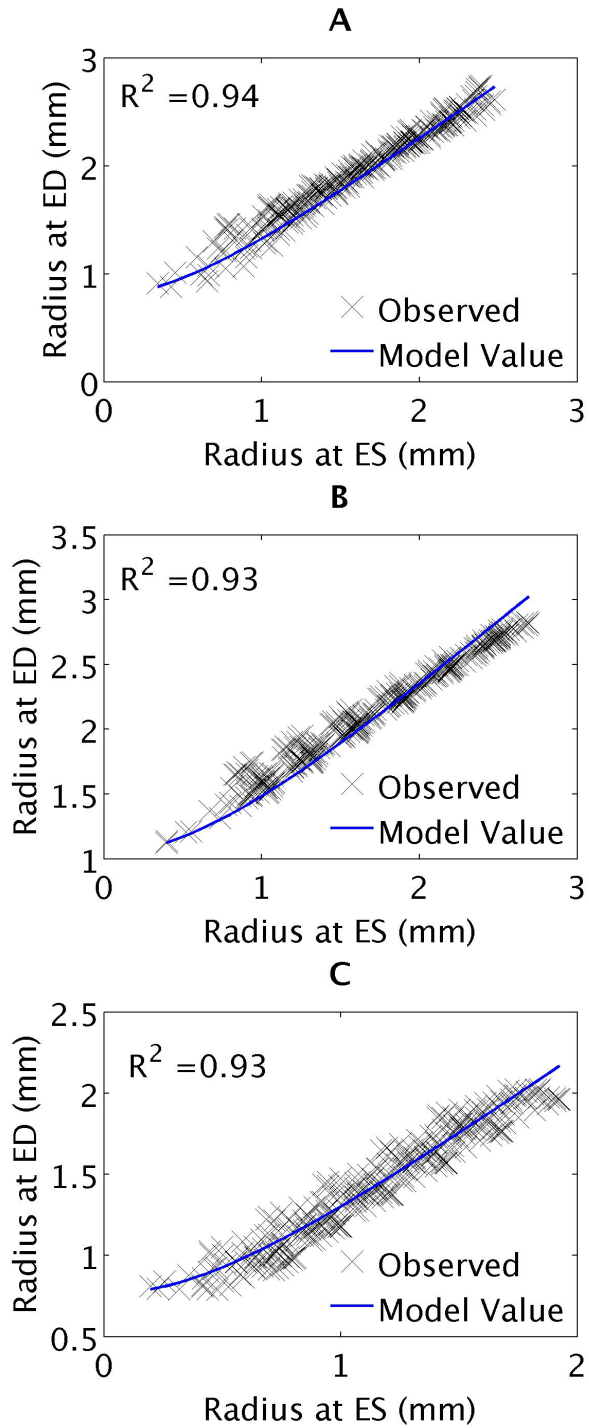


Figure 3.4: Observed and linear model-predicted radial motion at the basal (A), midventricular (B) and apical (C) levels of a normal LV.

### ***3.2.2 Polynomial Model of Deformation in Normal and Infarcted Mouse Hearts***

LAD occlusion created a myocardial infarction in the apical antero-lateral region of the LV. Speckle tracking for a typical SA cine is shown in Figure 3.2E; the infarct region is located in the enclosed red contour. Compared to normal hearts, there was higher regional variability in both radial and circumferential motion in the infarcted heart (Figures 3.2A-D). Equal weighting factors for longitudinal, circumferential and radial components were chosen for the objective function, and the weighting factor for the incompressibility constraint was 4 times greater. Reflecting the greater regional variation in the presence of infarction, coefficient values in Table 2 show larger contributions from coupling and higher order terms in infarcted hearts than in normal hearts. Normalized MSE for predicted motion in the polynomial model was  $7.4 \pm 2.1\%$  for infarcted hearts, and  $8.2 \pm 2.3\%$  for normal mouse hearts.

**Table 2.** Normalized coefficient values for polynomial model:

	Parameter	Normal Heart	Infarcted Heart
	$R_c$	-0.53±0.12	-0.88±0.22
	$g_i$	1.35±0.19	1.24±0.21
	$h_i$	0.91±0.18	0.09±0.02
		-4.15±1.35	4.18±2.37
		10.29±5.21	-5.81±2.19
		-28.21±6.61	-0.82±17.26
		5.41±2.17	2.20±1.52
$r(R,\Theta)$	$x_1$	-1.42±0.21	-3.42±0.32
	$x_2$	0.06±0.02	2.28±0.21
	$x_3$	1.25±0.31	3.94±1.14
	$x_4$	0.02±0.12	-2.27±0.32
$r(\Theta,Z)$	$v_1$	0.26±0.07	-0.24±0.08
	$v_2$	0.01±0.12	0.27±0.17
$\theta(\Theta)$	$\Theta_c$	.09±0.05	-0.65±0.19
	$s_i$	-0.24±0.11	0.82±28
	$t_i$	0.76±0.18	6.59±0.82
		2.42±0.91	-3.12±2.94
		-9.81±3.26	-30.25±12.52
		12.59±6.27	45.19±17.85
-7.48±3.46	-29.27±7.27		
$\theta(R,\Theta)$	$y_1$	-0.11±0.05	-11.52±4.7
	$y_2$	0.45±0.13	-10.31±3.1
	$y_3$	0.14±0.08	8.12±0.89
	$y_4$	-0.03±0.12	-8.79±3.2
$\theta(\Theta,Z)$	$w_1$	0.11±0.14	-0.52±0.31
	$w_2$	-0.09±0.10	0.81±0.27
$z(\Theta,Z)$	$Z_c$	-0.14±0.05	-0.23±0.11
	$u_1$	0.04±0.02	1.21±0.41
	$u_2$	1.15±0.06	1.12±0.37
	$u_3$	-0.01±0.06	-0.89±0.29

### 3.2.3 Impact of the Incompressibility Constraint

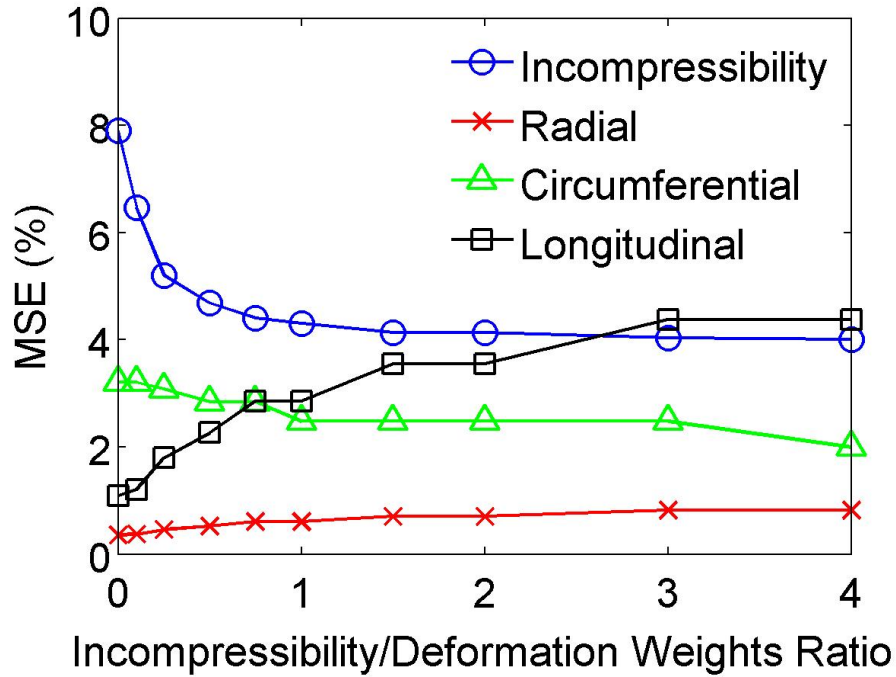


Figure 3.5: Mean Squared Error (MSE) in the polynomial model for each component of the optimization Equation (13) for a representative infarcted heart.

Higher incompressibility weights push the determinant value closer to 1, decreasing incompressibility error (blue curve). The tradeoff for increasing incompressibility weights is the increase in error in the longitudinal (black curve) and radial (red curve) deformation components.

Figure 3.5 shows the effects of tolerating different levels of myocardial volume change on the match between model-predicted and measured deformations using the generalized model. As expected, increasing the weight for the incompressibility constraint in the objective function reduced volume changes while increasing the mismatch between measured and predicted deformed

positions. Increasing the weight for the incompressibility constraint had more effect on predicted longitudinal and circumferential motion than on radial motion. This trade-off between incompressibility and measured deformation may be particularly useful in the presence of locally incompatible deformations due to acquisition artifacts or limitations of speckle tracking algorithms. Figure 3.6 shows a SA image where myocardial displacement from end-diastole to end-systole were derived using MSAD speckle tracking. In Figure 3.6A, improbable displacements are observed in the septal and posterior regions of the endocardial wall (outlined by white circles), where initially square elements appear to collapse or overlap in the deformed state. By incorporating a near incompressibility constraint using my kinematic polynomial model, improbable displacements are corrected as shown in Figure 3.6B.

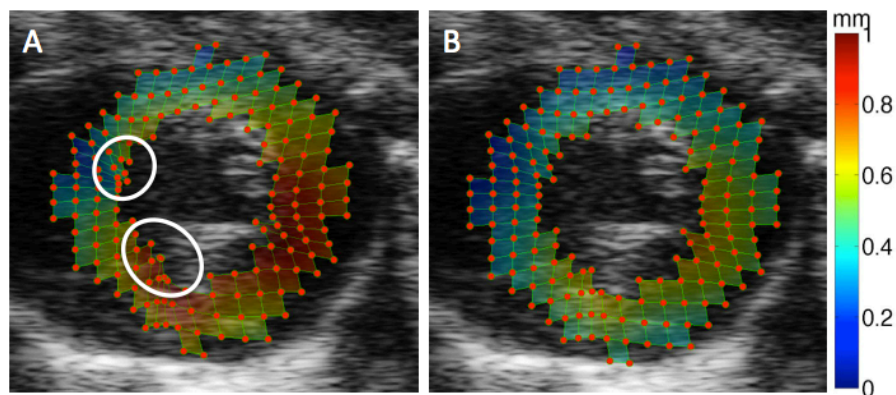


Figure 3.6: Color map of myocardial displacement derived from using MSAD speckle tracking only (A), and corrected displacement map using the polynomial kinematic model (B). Color represents relative magnitude of displacement. In (A), improbable displacements are observed where myocardial regions appear to collapse or overlap as shown inside the white circle.

### 3.4 DISCUSSION

Ultrasound imaging is commonly used to image myocardial motion in patients and in animal models of heart disease. Techniques, such as speckle tracking, provide valuable information about deformation throughout the myocardium, which can be particularly valuable in diagnosing regional abnormalities such as ischemia or infarction. However, motion estimates from techniques such as speckle tracking are also susceptible to noise and artifacts, particularly at the rapid heart rates present in small animals. Mathematical models that incorporate other known information about myocardial deformation can be used as a filter to correct errors in raw displacement or deformation data. In this chapter, I presented a simple kinematic model that incorporates three important aspects of myocardial deformation: the fact that myocardium is nearly incompressible; the fact that adjacent pieces of myocardium are physically connected, so that deformed positions vary smoothly in space; and regional variation in undeformed geometry. I found that a model based on relatively simple polynomial functions could capture deformation even in the setting of severe regional dysfunction due to myocardial infarction, matching measured deformations from speckle tracking well overall while correcting locally incompatible deformations that clearly reflected errors in the underlying data.

The incompressibility constraint has been widely used in cardiac image processing to improve segmentation and motion tracking (Bistoquet 2008; Garson 2008; Mansi 2010; Wang 2010; Zhu 2010). Geometric models of the left ventricle

inherently incorporate both incompressibility and local smoothness of deformation, in addition to other prior information, but have been less widely used in image processing. At the simplest extreme, models that treat the equatorial region of the left ventricle (LV) as an axisymmetric, thick-walled cylinder are easy to implement, solve quickly, and have provided important insights into aspects of heart mechanics such as the impact of material properties on deformation and the genesis of LV torsion (Humphrey 1989; Guccione 1991; Costa 1996). Unfortunately, assumptions such as axisymmetry have limited the utility of these simpler models in real-world medical imaging settings. By contrast, sophisticated finite-element models that incorporate not only incompressibility and smoothness of deformation but also realistic geometries, fiber anatomy, activation patterns, etc. have proven very useful in extracting 3D displacement fields from tagged MRI image sequences (Young 1995; Young 1999; Aelen 1999). The primary limitation of these more sophisticated models is that they are time-consuming to construct and run. The kinematic approach proposed here attempts to strike a balance – incorporating incompressibility through a penalty in the objective function and local smoothness and geometric variations in undeformed geometry through the chosen polynomial functions (Equation 12) – while limiting computational costs of fitting the model to each dataset. One of the most surprising findings of this study was that deformation throughout the normal mouse heart can be so accurately described with a very simple linear model (Equations 4,7) that assumes that most components of the deformation gradient tensor are constant everywhere. In fact,

while the nonzero components of the deformation gradient tensor identified from plotting displacement data here are not the same as those typically assumed in cylindrical models, the expression for radial deformation in Equation 7 is identical to that used by Guccione et al. in their classic cylindrical model of LV deformation (Guccione 1991). The success of this model in my study suggests that much of the regional variation in deformation in a normal heart must be due to regional variation in anatomy ( $R_0$  and  $r_0$  in Equation 7). This finding may explain in part why cylindrical models have provided so much insight into normal heart mechanics despite their obvious geometric limitations.

I introduced an objective function that allows the weight of the incompressibility constraint to be varied relative to measured deformations. As I increased the weight for the incompressibility constraint relative to the deformations (Figure 3.5), I found that the MSE in the incompressibility term converged to 4%, reflecting an overall change in myocardial volume of 4%. While consistent with previous studies (Judd 1991), this number also accounts for roughly half the overall NRMSE in the fitted data, which could be reduced by using a different target value for the determinant of the deformation gradient tensor. My objective function also allowed individual deformation components to be weighted differently according to confidence in their measurement, a capability we did not utilize in this study. However, this formulation could be particularly attractive in situations where confidence in measurements of individual deformation components varies. For example, if deformation information at a point in the heart wall were derived from

two intersecting views, one of which had an artifact or speckle tracking error that could be recognized by a quality metric, then de-weighting the flawed deformation information would allow the model to locally replace the missing component based on the high-quality components in the perpendicular view and the incompressibility constraint. In the case of MSAD, the actual minimum difference, versus the mean difference across all search observations, provides a convenient quality metric that is applicable in conditions appropriate for MSAD – i.e. all but very low SNR imaging.

One limitation of the modeling approach presented here is that weights for all deformation components and locations were not exactly equal. I did choose units that gave approximately equal numerical ranges for each variable (approximately 0-3 mm for radius, 0-5 mm for axial position, 0- 6 radians for circumferential position). However, additional scaling of individual deformation measures in the objective functions could further improve the method, such as introducing weighting schemes that vary by component or by region. I also note that I modeled deformation from end systole to end diastole, when the LV is expanding and extending, while most models use end diastole as a reference state and examine deformations between end diastole and end systole. These two approaches provide equivalent deformation information, and can be inter-converted by taking the inverse of the deformation gradient tensor  $F$ .

In summary, I developed a kinematic model intended to offer a compromise between incorporating prior information about left ventricular deformation and

limiting computational expense, assuming only that displacements in the left ventricle are polynomial functions of initial position and that the myocardium is nearly incompressible, while allowing myocardial motion to vary spatially as would be expected in an ischemic or dyssynchronous left ventricle. This model accurately represented the motion of both normal and infarcted mouse left ventricles during the cardiac cycle, with normalized root mean square errors in predicted deformed positions of only  $8.2 \pm 2.3\%$  and  $7.4 \pm 2.1\%$  for normal and infarcted hearts, while correcting physically unrealistic local deformation components arising from errors in speckle tracking.

# **Chapter 4: High Frequency Ultrasound Reveals Reduced Left Ventricular Dyssynchrony and Remodeling in Inducible Nitric Oxide Synthase Knockout Mice**

## **4.1 INTRODUCTION**

Nitric oxide (NO) is a ubiquitous intracellular signaling molecular involved in many physiological processes. One of its prominent roles is its effectiveness as a vasodilator via the activation of secondary messenger: cyclic guanosine monophosphate (cGMP). NO, therefore, also plays an important role in the pathological processes of many vascular related diseases. For example, significant increase in NO has been measured in rat brains after occlusion of the cerebral artery (Malinski, 1993). Presence of NO in the vasculature is also known to promote angiogenesis by recruiting new cells for blood vessel growth, and therefore, it plays an important role in cancer development (Fukumura, 2006). In one study, patients with lung cancer exhibited higher levels of NO than healthy volunteers (Liu, 1998). Furthermore, inhibition of NO production has been shown to attenuate the development of lung tumor in a mouse model (Kisley, 2002), giving insights to new methods for cancer therapy.

Many studies have also focused on the roles of NO in cardiovascular diseases, particular myocardial infarction (MI). Under normal conditions, NO is necessary for normal cardiac function, and mediates several beneficial effects in the cardiovascular system including anti-remodeling, cell survivability, vasodilation, and inhibition of platelet accumulation (Massion, 2003). On the other hand, under

pathological conditions, the presence of NO can be deleterious to heart function. Immediately after an ischemic event, inflammatory cytokines stimulate the production of NO through increased expression of inducible NO synthase (iNOS). Increased production of NO, in conjunction with reactive oxygen species such as superoxide, contribute to the pathophysiology of post-MI left ventricular (LV) remodeling, and eventually cardiac dysfunction (Pacher, 2007).

Numerous studies have reported that lack of NO, through iNOS gene knockout (KO), is beneficial to heart function after ischemia in mice (Guo, 1999; Sam, 2001; Feng, 2001; Li, 2003; Luo, 2005). At least one study has reported that iNOS KO mice do not exhibit improved cardiac function after MI, and survivability, infarct size, and systolic function were not significantly different from wild type (WT) mice after 1 month (Jones, 2005). It has previously been shown that mice lacking iNOS exhibit both attenuated left ventricular remodeling and circumferential extent of wall thinning late after MI using MR imaging (Gilson 2007). Here, I applied non-invasive imaging techniques using high-frequency ultrasound to show that these beneficial late effects in iNOS knockout (KO) mice. Furthermore, early myocardial dyssynchrony is quantified using novel metrics to distinguish differences in heart motion, and predict late phase LV remodeling. Specifically, I introduced Contraction Index (CI) to describe dyskinetic bulging during systolic contraction, where motion in the infarct region is out of sync with motion in the remote myocardium. Similarly, Diskinesia Index (DI) is introduced to quantify motion irregularity after MI. Consistent with other dyssynchrony metrics, such as circumferential/radial

uniformity ratio estimate (CURE and RURE), DI is a Fourier-based metric that detects non-uniform myocardial motion. However, compared to CURE and RURE, DI is robust against motion noise, which is persistent in ultrasound speckle tracking. I showed that CI and DI are sensitive quantifiers for early myocardial dyssynchrony and dysfunction, and potentially quicker prognosis and recommendation of cardiovascular resynchronization therapy to LV remodeling.

## **4.2 METHODS**

### ***4.2.1 Animal Model and Myocardial Infarction***

The animal experiments in this study conformed to a protocol approved by the University of Virginia Animal Care and Use committee. Age matched (12-14 wks old) wild type C57BL/6 (n = 11, Jackson Labs) and iNOS KO (n = 9, Victor E. Laubach Lab) mice were employed in this study. MI induction was surgically performed via 1-hour occlusion-reperfusion of the left anterior descending (LAD) coronary artery (Yang, 2002).

### ***4.2.2 Ultrasound Image Acquisition.***

Prior to MI surgery, all mice were imaged at baseline (Bsl) using a 30 MHz ultrasound linear array transducer (VisualSonics, Toronto, Canada). The transducer has a spatial resolution of 50  $\mu\text{m}$  axially and 110  $\mu\text{m}$  laterally. Anesthetic induction was performed with 2% isoflurane mixed with oxygen in a closed chamber. Once sedated, mice were placed in supine position on a heated platform with the appendages taped to electrocardiogram (ECG) sensors to

monitor heart rate and respiration (Figure 4.1A). Anesthesia was administered continuously with 1.5 – 1.8% isoflurane through a nose cone. Body temperature was maintained at  $37\pm 0.2^{\circ}\text{C}$  with the aid of a digital rectal thermometer, the heated platform on which the animal lay, and an external lamp for extra heat source. Chest hairs were depilated with an electrical shaver followed by dime size application of Nair. A generous dollop of ultrasound gel was applied over the shaved chest for imaging.

A series of parallel short-axis (SA) cines were acquired at 0.5mm intervals from apex to base through a millimeter-adjustable motion stage. The transducer was rotated exactly  $90^{\circ}$  within a pivoting mount and a single long-axis (LA) cine was acquired. Frame rate was optimized at approximately 350 Hz for SA and 300Hz for LA. Imaging time per mouse was approximately 30 minutes, including mouse preparation.

Ultrasound data were also acquired on days 2, 4, 7, 14, and 28 post MI using the same protocol.

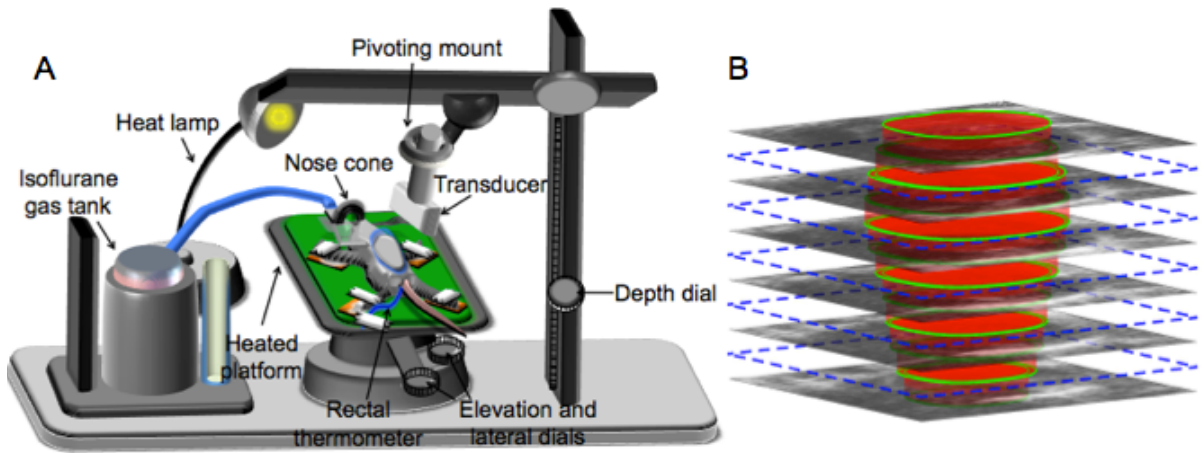


Figure 4.1: (A) Mouse setup during imaging (not drawn to scale). Mouse is kept sedated through constant infusion of anesthesia from an isoflurane gas tank.

Sensors on the platform monitor both heart rate and respiration, while also providing heat to help maintain normal body temperature. An external lamp provides additional source of heat, and body temperature is monitored using a digital rectal thermometer. (B) Acquisition of parallel SA B-mode cines along the length of the ventricle. Adjacent B-mode cines are 0.5 mm apart. For display purpose, B-mode cines for every other slice are omitted (dotted blue outline). ESV and EDV volumes are quantified using Simpson's disc method, where endocardial contours (green) defined at ES and ED are used to derive at cylindrical discs (red) at 0.5 mm thickness.

#### 4.2.3 Quantifications of Cardiac Function

LV remodeling was quantified using end-systolic (ES) and end-diastolic volumes (EDV) from endocardial contours in SA cines. The ESV and EDV were measured using the Simpson's disc method, with a 0.5mm thickness for each SA

slice (Figure 4.1B). To ensure contours are traced consistent at the same time point for all mice at different time points, ECG signals were used to locate ED and ES frames, where peak R-wave denotes ED frame, and ES frame was determined based on the closing of the aortic valves, which can be detected from the LA cines and basal SA cines.

Infarct size is a strong predictor of subsequent LV remodeling, which in turn predicts morbidity and mortality. Radial strain, fractional shortening (FS) and circumferential extent of wall thinning were used as indicators for infarct size. FS is defined as the difference in endocardial wall radius at ED and ES over the endocardial wall radius at ED. Wall thinning was defined based regions with thickness less than 50% of the baseline thickness (Gilson, 2007). Therefore, circumferential extent of wall thinning is a measure of the angle encompassing the myocardium with wall thickness less than 50%. Area at risk exhibits low strain values due to lack of motion. Computed radial strains from speckle tracking were also used to assess infarct size. A threshold of 16% was selected based on comparison with MRI contrast enhanced imaging protocol. For each SA slice, percent infarct size was determine to be ratio of the largest contiguous area of the myocardium where radial strain is less than 16% to the total area of the myocardium. The final value is determined from summing over the SAs for each mouse.

Many of the existing dyssynchrony metrics rely on myocardial strain measurements, including CURE, RURE and standard deviation of time to peak

strain (Cho 2005; Bilchick 2008; Delgado 2008; Li 2011; Budge 2012). Since strain is a derivative of displacement, amplification of noise in strain calculation due of noisy displacement estimation is common, and this can lead to unreliable strain-based dyssynchrony metrics. Two novel metrics, robust to noisy displacement estimation, of LV dyssynchrony were explored.

The first metric is CI, which was previously developed in my lab (Li, 2011), and is defined as the ratio of positive radial displacement to total radial displacement. A low CI value is associated with dyskinetic bulging in the infarct zone during systolic contraction. A CI of unity would represents completely uniform myocardial displacement, while a CI value approaching zero would indicate the degree of anti-phase displacement during paradoxical wall thinning.

The second metric is DI. DI values were computed as the square root of the ratio of the zero-order to the sum of the zero-order and first order terms derived from Fourier transform of the radial displacement spatially distributed along the endocardial wall. It's computationally similar to RURE, but instead of using strain estimates, displacement results are used. Numerically, it is calculated as the square root of the ratio of the zero-order power term to the sum of zero-order and first order power terms:

$$DI = \sqrt{\frac{A_0^2}{A_0^2 + \alpha A_1^2}}$$

The  $\alpha$  multiplier is added to increase the sensitivity of the first-order term that describes myocardial dyssynchrony, where a higher value will improve detection of dyssynchrony.

To quantify the significance of differences between WT and KO mice, Student t-tests were performed. Plotted values are reported as mean  $\pm$  standard deviation.

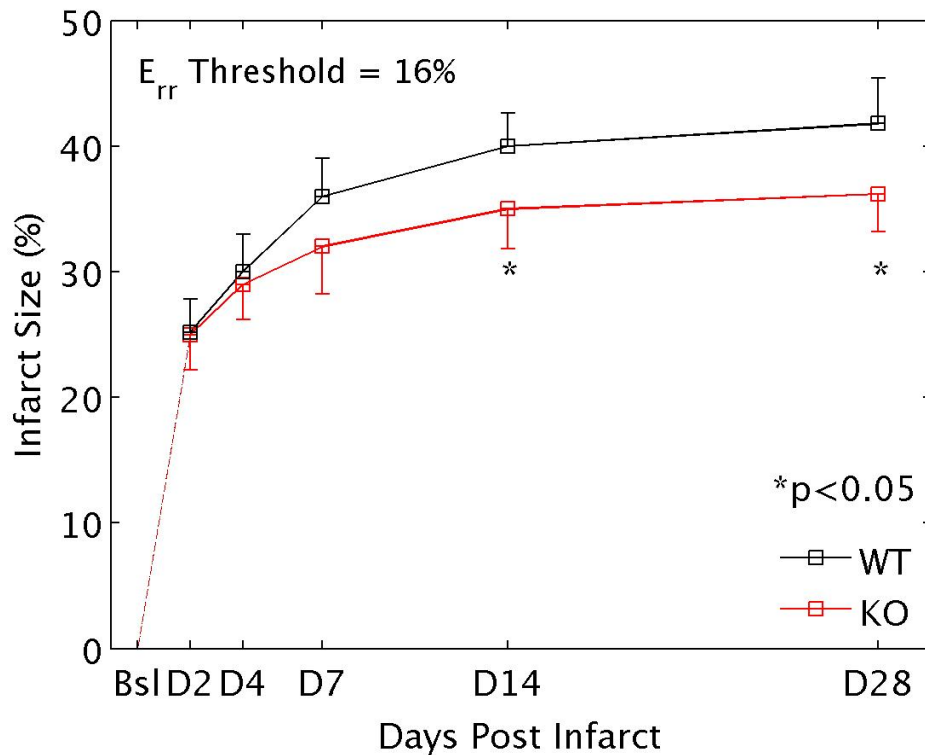


Figure 4.2: Radial strain data derived from ultrasound speckle tracking in SA B-mode cines were used to determine infarct size after MI. Infarct sizes were similar between KO and WT on days 2 and 4 after MI. Significant differences in infarct sizes were observed on days 14 and 28 after MI.

### 4.3 RESULTS

All mice survived until day 28 post MI, and were euthanized after imaging on day 28. Infarct size determined from radial strain data also confirmed that the difference in LV remodeling arises from lack of iNOS as opposed to surgery (Figure 4.2). WT and iNOS KO mice exhibited similar infarct sizes on D2 ( $26.6\pm 3.1\%$  and  $26.3\pm 3.5\%$ , respectively). D4 and D7 sizes were also not significantly different. This confirms that ischemic reperfusion surgeries were performed consistently between the groups. Infarct sizes for WT and iNOS at D14 are  $38.1\pm 2.9\%$  and  $33.1\pm 3.1\%$  ( $p < 0.05$ ), and at D28 are  $40.3\pm 4.1\%$  and  $36.2\pm 2.7\%$  ( $p < 0.05$ ), respectively.

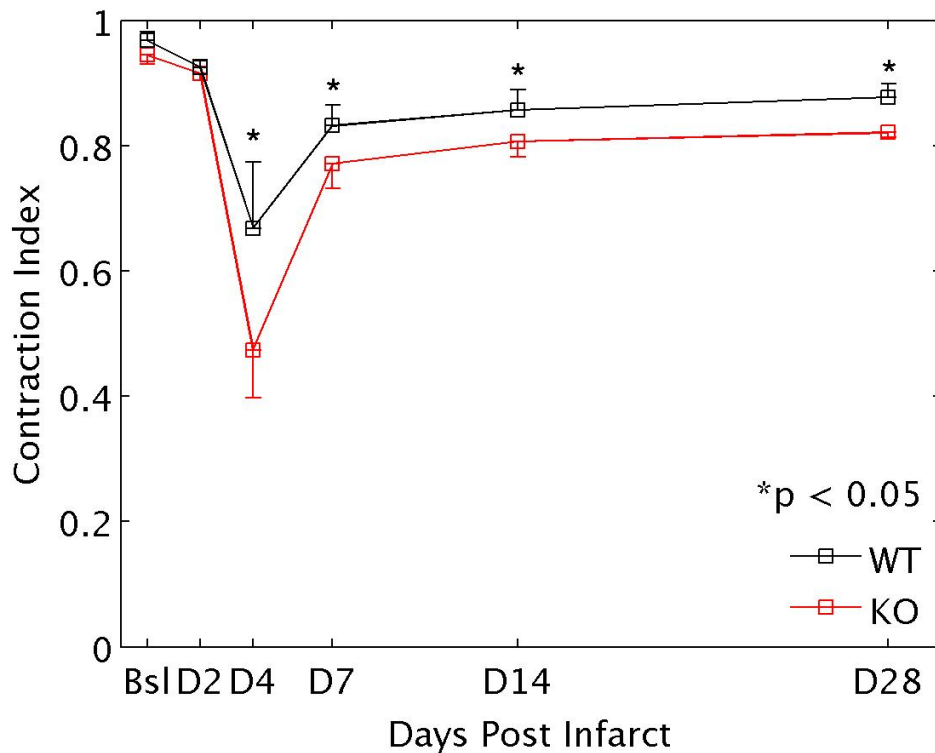


Figure 4.3: Time course of CI values show reduced dyskinetic systolic bulging in KO mice after 4 days post MI ( $p < 0.05$  compared to WT mice). Myocardial dyskinesia occurs early after MI for both groups.

Similarly, reduced dyskinesia was observed in KO mice, particularly at day 4 ( $p < 0.05$ , but also significant at day 28), as shown in Figure 4.3. Thus, dyskinetic bulging during systole was found to be most pronounced during the early phase after MI. Baseline CIs were near unity for both groups, indicating near uniform displacement throughout the myocardium. After the first week, scar formation increased the stiffness of the infarct zone and motion became more akinetic. This evolving pattern of partial recovery is evidenced by the rebound in the CI curves at day 7 post-MI.

It has been shown that early LV dyssynchrony predicts eventual LV remodeling after MI (Mollema, 2007). LV remodeling is assessed using ESV, EDV and EF. Both WT and KO groups have significant increases in ESV and EDV from baseline after D7 as shown in Figure 4.4. Significant attenuation of LV remodeling was apparent in iNOS KO mice as shown by the reduced ESV and EDV at days 7, 14, and 28 post MI ( $p < 0.05$ ). ESV and EDV were similar between the groups at baseline and days 2 and 4 post MI. This further reaffirms that age-matched mice have similar LV geometry and MI surgeries were performed consistently throughout the mice. Additionally, decreases in ejection fraction (EF) were observed in both groups. In Figure 4.5, EF dropped from approximately 68  $\mu\text{L}$  at baseline to approximately 49  $\mu\text{L}$  at D2 post-MI. Significant differences in EF are observed between KO and WT mice at D14 and D28 post-MI. As predicted by higher CI

value at D4, KO mice have attenuated LV remodeling at D7, D14, and D28 post-MI as indicated by lower ESV and EDV (Figure 4.4), and higher EF (Figure 4.5).

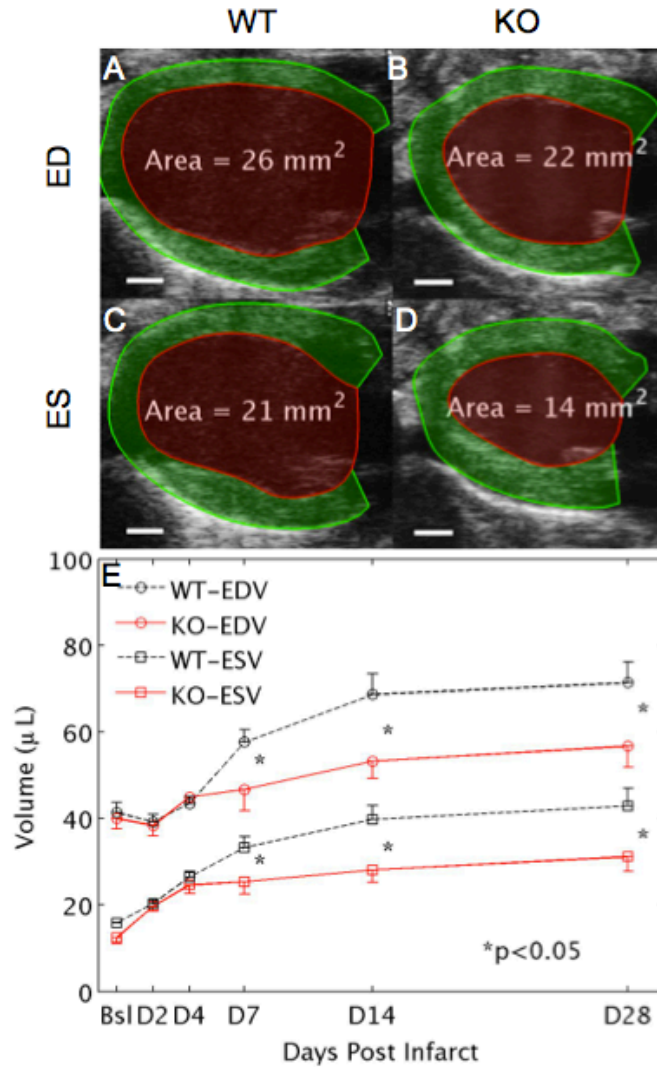


Figure 4.4: Time course of ESV and EDV (E) shows similar volumes at baseline, D2, and D4 between WT and KO mice. Volumes diverge after D4 and are significantly different between WT and KO at D7, D14, and D28 ( $p < 0.05$ ). Panels A-D are examples of LA B-mode images, A, WT at ED; B, KO at ED; C, WT at ES; and D, KO at ES). LV cavity areas based on endocardial wall tracing (shaded red region) are also shown. While not the actual volume measurements, these area

measurements showed attenuated LV remodeling for iNOS KO mice late after MI.

Scale bar in each B-mode image is 1mm.

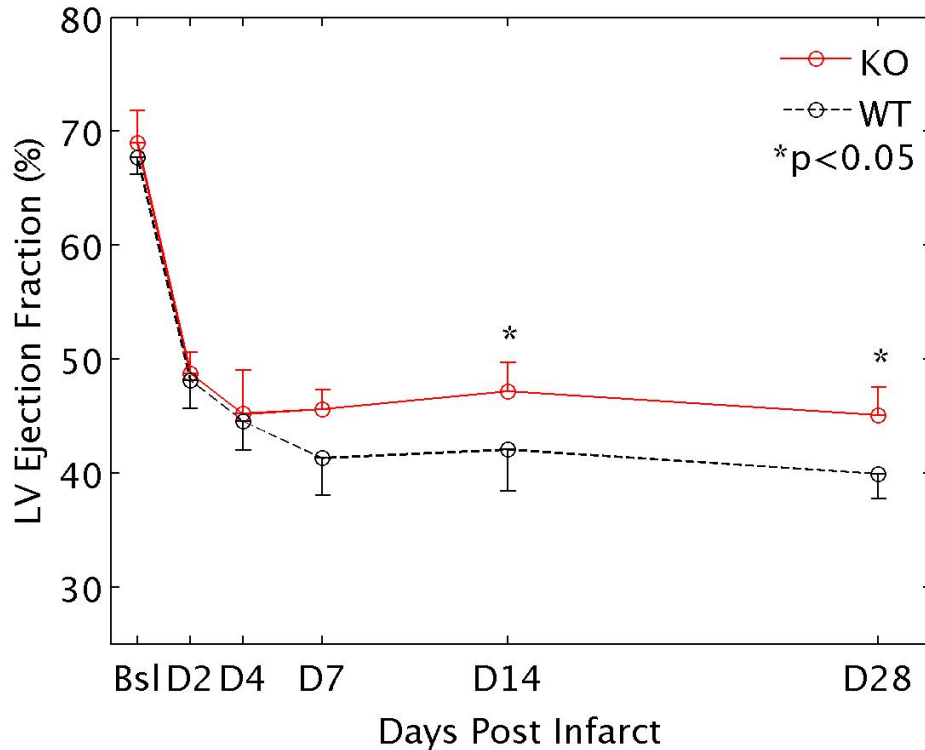


Figure 4.5: Time course of EF computed as the ratio of the difference between EDV and ESV to EDV. Both groups have similar EF on Baseline, and D2 and D7 post-MI. Significant differences in EF between KO and WT mice are observed D7 and D29 post-MI.

Dyssynchrony values using DI are plotted in Figure 4.6. Values range from 0 (pure dyssynchrony) to 1 (perfectly synchronous). Dyssynchrony values at baseline are consistently close to 1 ( $0.98 \pm 0.01$ ), and decrease dramatically early after MI due to dyskinesia, reaching a minimum at D4 ( $0.47 \pm 0.11$ ). Consistent with

CI, a similar argument can be made that myocardial motion becomes more akinetic due to stiffer myocardium from scar formation in the infarct zone, and therefore there is a rebound in dyssynchrony values and until reaching a plateau in late MI. Dyssynchrony values for 5 time-points post MI are all significantly different from baseline ( $p < 0.05$ ).

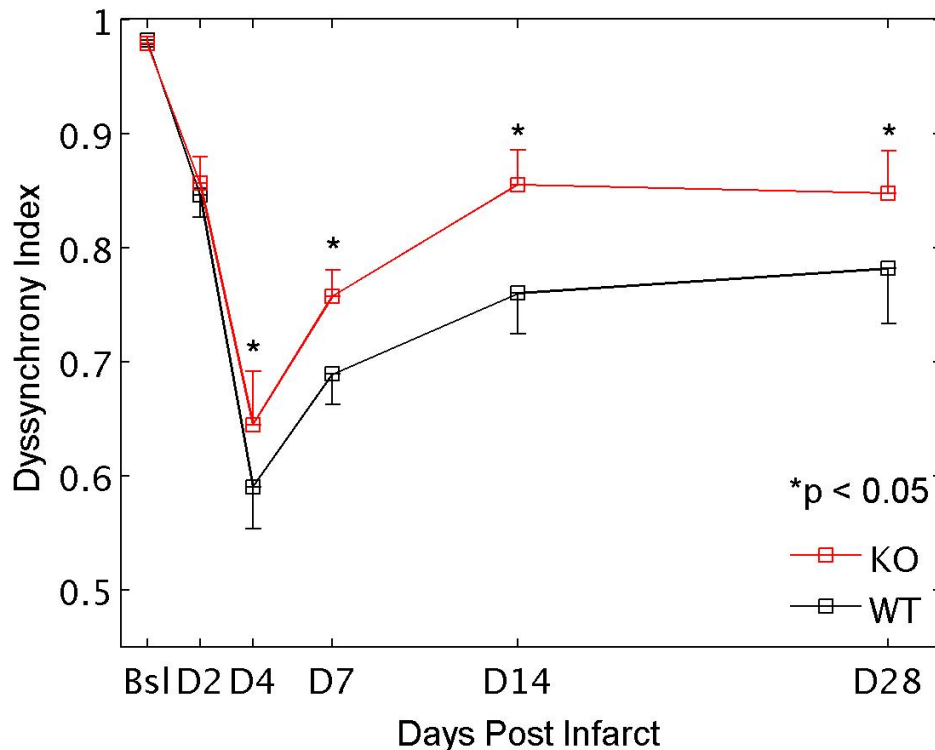


Figure 4.6: Time course of DI shows increased dyssynchronous myocardial motion after MI for both groups. Dyssynchrony was most apparent at D4, with KO mice exhibiting less dyssynchrony than WT mice ( $p < 0.05$ ).

The circumferential extent of wall thinning was reduced in KO mice. Examples of wall thinning are shown in Figure 4.7 using SA B-mode images at ES. Intramyocardial thickness for pre-MI mice (Figure 4.7A and 4.7B) is approximately

0.8-1.0mm. For post-MI mice, significantly thinned wall is defined as myocardial thickness less than 0.4-0.5mm. Figures 4.7C and 4.7D are D14 SA B-mode images acquired 2mm from the apex. In Figure 4.7C, thinned wall are visibly distinguishable in WT mice: circumferentially, more than one-third of the heart showed significant decreased in wall thickness. Whereas in KO mice, less than one-fourth of the heart showed decreased wall thickness. Circumferential extent of wall thinning for the 6 time points are plotted in Figure 4.8 for the basal (8A), mid (8B), and apical (8C) levels of the LV, and also the average total for the entire heart (8D). Divergence in data occurs as early as D4 between the 2 groups.

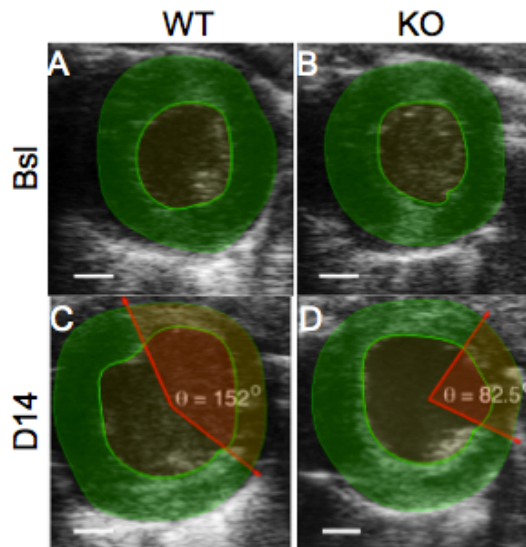


Figure 4.7: Epicardial and endocardial were manually traced at ES phase of the cardiac cycle for all time points. Circumferential extent of wall thinning is defined as the extent (in degrees) of myocardium where thickness is less than 50% of baseline values. Panels A and B above are baseline SA B-mode images (acquired 2mm from apex) for WT and KO mice, respectively. Myocardial region is shown in green. Panels C and D are SA B-mode images acquired at D14 for WT and KO

mice, respectively. Regions of significant wall thinning is shown between red arrows. Scale bars are 1mm.

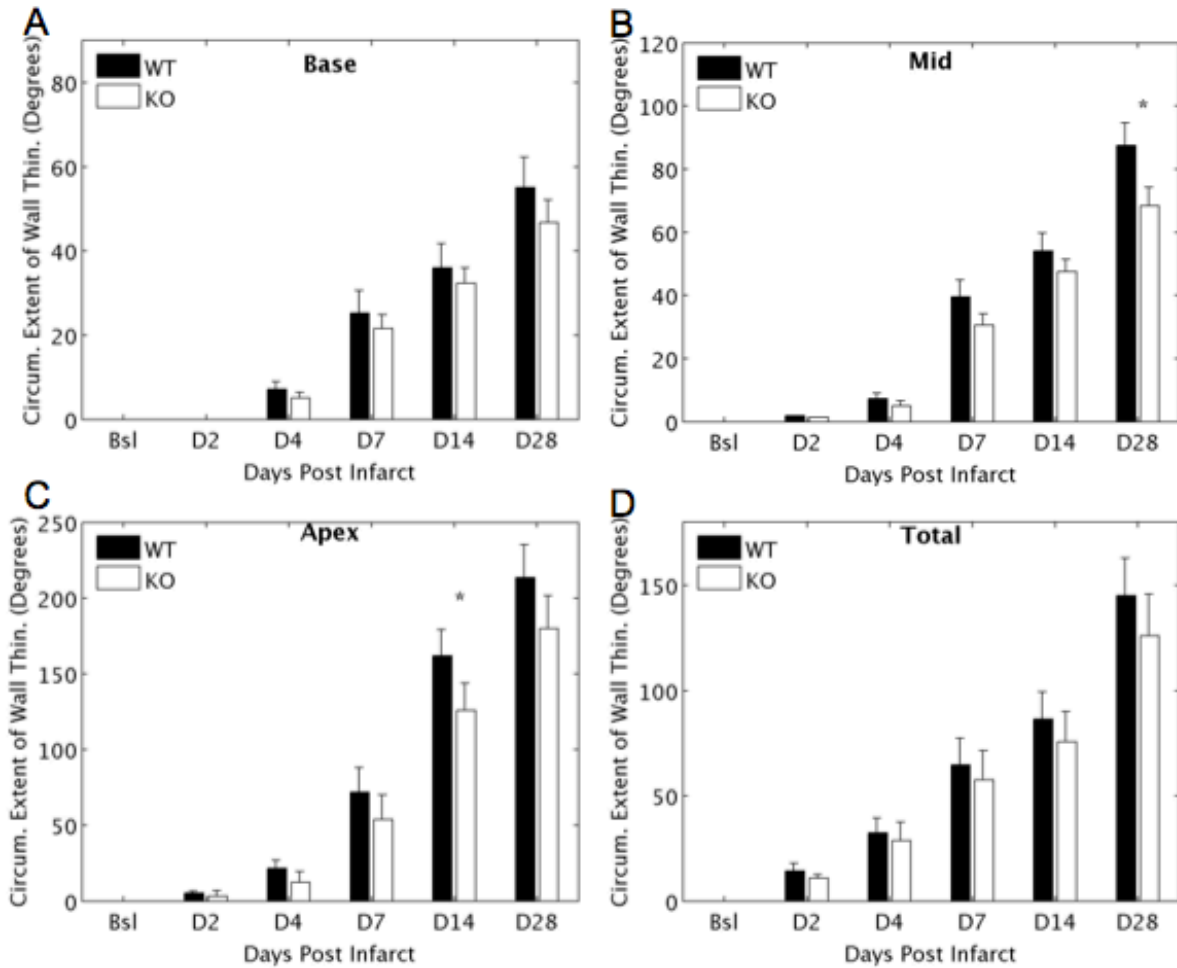


Figure 4.8: Time course of wall thinning between KO and WT mice acquired at the basal (A), mid (B), and apical (C) levels of the LV, and the average total (D) across all acquired SA slices. As a result of LAD ischemic-reperfusion surgery, apical slices have greater extent in wall thinning.

#### 4.4 DISCUSSION

Inducible nitric oxide synthase plays an important role in left ventricular remodeling and dysfunction after myocardial ischemia. Myocardial remodeling and function were assessed using ultrasound periodically for a month after reperfusion of myocardial infarction between iNOS KO and wild type control mice. Anatomically, KO and WT mice showed similar LV remodeling early after MI. Infarct size assessed using ultrasound-based radial strain show no significant differences between KO and WT mice ( $26.3 \pm 3.5\%$  and  $26.6 \pm 3.1\%$ , respectively) 4 days after MI. On the other hand, myocardial motion analyses revealed that dyssynchrony occurred early after MI, and significant differences were observed between KO and WT mice. For late phase MI patterns, dyssynchronous motion has mostly dissipated in KO and WT mice, whereas differences in LV remodeling becomes more apparent between them. Infarct size measured at day 28 were  $33.1 \pm 3.1\%$  and  $38.1 \pm 2.9\%$  for KO and WT mice ( $p < 0.05$ ), respectively. While the role of iNOS after MI still needs to be elucidated, we showed that the lack of iNOS during and after MI attenuates LV remodeling and dyssynchrony.

This work has demonstrated that iNOS KO mice have reduced LV remodeling and dyssynchrony, thus improved cardiac function, late after MI. However, this work does not show that iNOS plays an important role in LV remodeling and function, rather it is the lack of iNOS that has beneficial effect to cardiac function after ischemia. The actual role of iNOS early after MI and whether

iNOS is only detrimental during MI in the presence of other reactive oxygen species still need to be elucidated. Several other studies (Guo 1999, Sam 2001, Feng 2001, Li 2003, Liu 2005, Gilson 2007,) have also showed improved cardiac function in iNOS KO mice, however this is the first study where differences in cardiac function are delineated using high frequency ultrasound.

Infarct size determination did not show a difference in ischemic-reperfusion surgeries between the KO and WT mice. This is to rule out any effects that can arise from differences in the initial sizes of the infarction. As previously mentioned, many cellular and molecular events occur during early phases of an MI that dictate late phase LV remodeling. Image acquisition time points included 2, 4, and 7 days post MI in order to capture the important changes that occur early after MI. More days can be added between days 2 and 7 for acquiring data to better reveal the changes that occur during early post-MI. This would also entail careful monitoring of rodent health through the first week as it recovers from surgery.

Myocardial motion analyses based on contraction and dyssynchrony indices, CI and DI, reveal that significant changes occur early after MI. In both WT and KO mice, dyskinetic bulging during systole was most pronounced at D4 (Figures 4.3 and 4.6). LV structural remodeling results (Figure 4.4B) show that significant divergence in ES and ED volumes between KO and WT mice occurs after D4, signifying the important molecular and cellular events that occur during the early phase of MI leading to LV remodeling. Additionally, rebound in contraction and dyssynchrony index curves occur on D7 for both groups. This rebound does

necessarily mean a return to normal myocardial motion, but is most probably due to stiff myocardium from scar formation, and cardiac motion becomes akinetic rather than dyskinetic.

CI and DI are also robust to noise because it utilizes displacement data as opposed to strain. Strain-based measures of dyssynchrony, such as CURE and RURE, are error-susceptible without proper filtering of displacement data, since noisy displacement data are often amplified after taken spatial derivatives to get strain. In ultrasound mouse imaging, rib shadowing, reverberation, and out of plane motion decorrelation impede accurate speckle tracking. I used a mathematical heart model to correct motion estimation based on incompressibility; however, correction is minimal for infarcted hearts. Both CI and DI showed low standard mean error at baseline, revealing consistent motion uniformity in healthy hearts.

CI and DI also detect early LV dysfunction. Both CI and DI reveal LV dyssynchrony as early as D4 post-MI (Figures 4.3 and 4.6). Compared to LV remodeling metrics, ESV, EDV and EF, divergence in these metrics are only apparent at D7 post-MI (Figures 4.4 and 4.5). This also infers that early LV dyssynchrony predicts late phase LV remodeling. The ability for CI and DI to predict eventual LV remodeling, and their ability to distinguish severity of LV dyssynchrony, for example between WT and iNOS KO mice, could potentially become valuable diagnostic tools to assess early LV dyssynchrony after MI and recommendation for cardiovascular resynchronization therapy.

# Chapter 5: Ultrasound Molecular Imaging For Ischemic Mouse Myocardium Using Targeted Microbubbles

## 5.1 INTRODUCTION

Misdiagnosis of acute coronary syndrome is common in patients with ambiguous symptoms. More than 2% of patients with unstable angina were mistakenly discharged from the emergency room, resulting in higher risk of mortality (Pope 2002). Molecular imaging using targeted ultrasound microbubbles (MB) has provided the capability to identify previously-ischemic regions of myocardium by molecularly targeting cell adhesion molecules that are displayed on the activated endothelial surface after ischemia/reperfusion injury (Linder 2001; Linder 2000; Kaufmann 2007; Davidson 2012).

Microbubbles (1-4 micron diameter) form the basis of an ultrasound contrast agent that is injected intravenously and flows freely within the cardiovascular circulatory system. Microbubbles have been used as an ultrasound contrast agent for border delineation and perfusion imaging in the heart (Lindner 1999). Microbubbles possess a thin shell, consisting of polymer, protein, or lipid monomolecular layers. Furthermore, biotinylated polyethylene glycol (PEG)-phosphatidylethanolamine (PE) can be added to the surface allowing attachment of biotinylated ligands via a streptavidin bridge (Klibanov 2005). For selective targeting of microbubbles, specific ligands can be attached to the microbubble shell that binds to a selected receptor that is displayed on the endothelial surface during

the course of the disease of interest. At the onset of ischemia/reperfusion injury, cellular adhesion molecules start to be displayed on the endothelial surface. Microbubbles targeted to these cell adhesion molecules can be used to locate the region of injury. In this way, microbubble targeting can mimic the behavior of leukocytes during inflammation (Figure 5.1). *In vivo*, ligand-specific microbubbles have been successfully targeted to P-selectin in models ischemia/reperfusion injury (Kaufman 2007, Lindner 2001, Ji 2009, Klibanov 2006, Rychak 2006, Weller 2003) and other adhesion molecules such as ICAM (Weller 2003, Weller 2005). *In vitro* experiments using parallel flow chambers have shown that microbubbles conjugated with multiple ligands have increased binding affinity (Ferrante 2009).

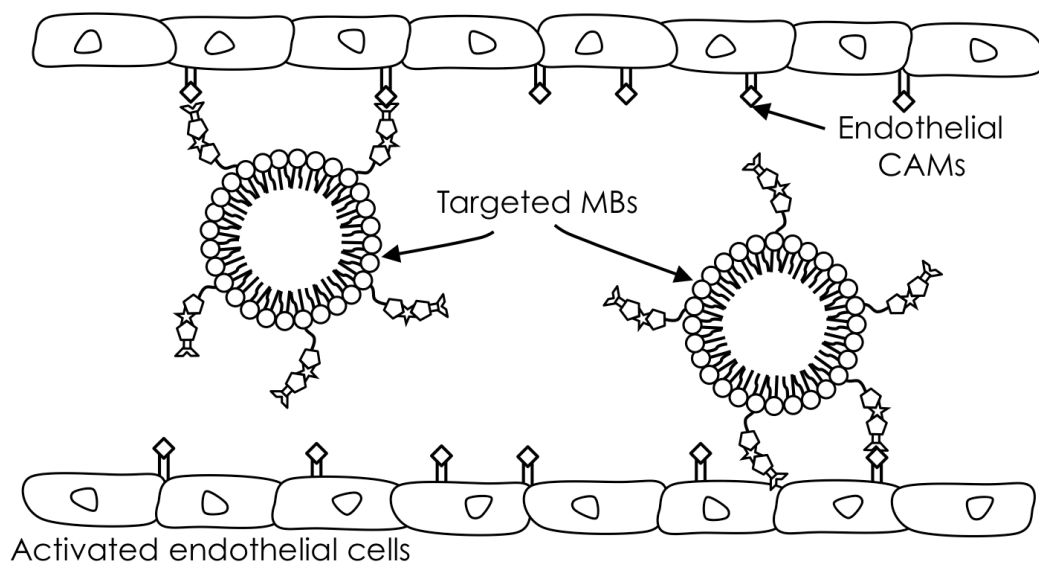


Figure 5.1: Specific ligands can be attached to the microbubble shell that binds to a selected receptor that is displayed on the activated endothelial cells during the course of the disease of interest. Microbubble targeting can mimic the behavior of leukocytes during inflammation.

Current methods for detection of targeted microbubbles mainly rely on injecting an initial bolus and waiting for untargeted microbubbles to clear out of the system while targeted microbubbles remain attached in the regions of interest (Lindner 2001, Villanueva 2002, 2007, Ji 2009, Klibanov 2006 Warram 2011, Weller 2003, Weller 2005, Willman 2009). However, in high blood flow environments, such as in the coronary arteries, high shear stress can cause detachment of microbubble from receptors on the endothelial wall (Talkakar 2004). Furthermore, acoustic shadowing can occur due to microbubble saturation and regional signal bias using bolus injection. Bolus injection frequently creates an initial microbubble saturation effect resulting in severe acoustic shadowing (Schlosser 2003). When using targeted microbubbles, acoustic shadowing can result in regional signal bias, where microbubble signals farther away from the transducer are shadowed by signals near the transducer. Generally, when using targeted microbubbles, it is usual to wait 8-10 minutes after initial bolus for unbound bubbles to clear and adequately isolate the signal originating from the remaining targeted bubbles attached in the regions of interest. An improved method for targeted microbubbles delivery using constant infusion is presented to remedy acoustic shadowing, and to allow better characterization of microbubble interaction with activated endothelium. Furthermore, dual targeted microbubbles design is also explored to increase binding efficiency of targeted microbubbles to its targets.

## 5.2 METHODS

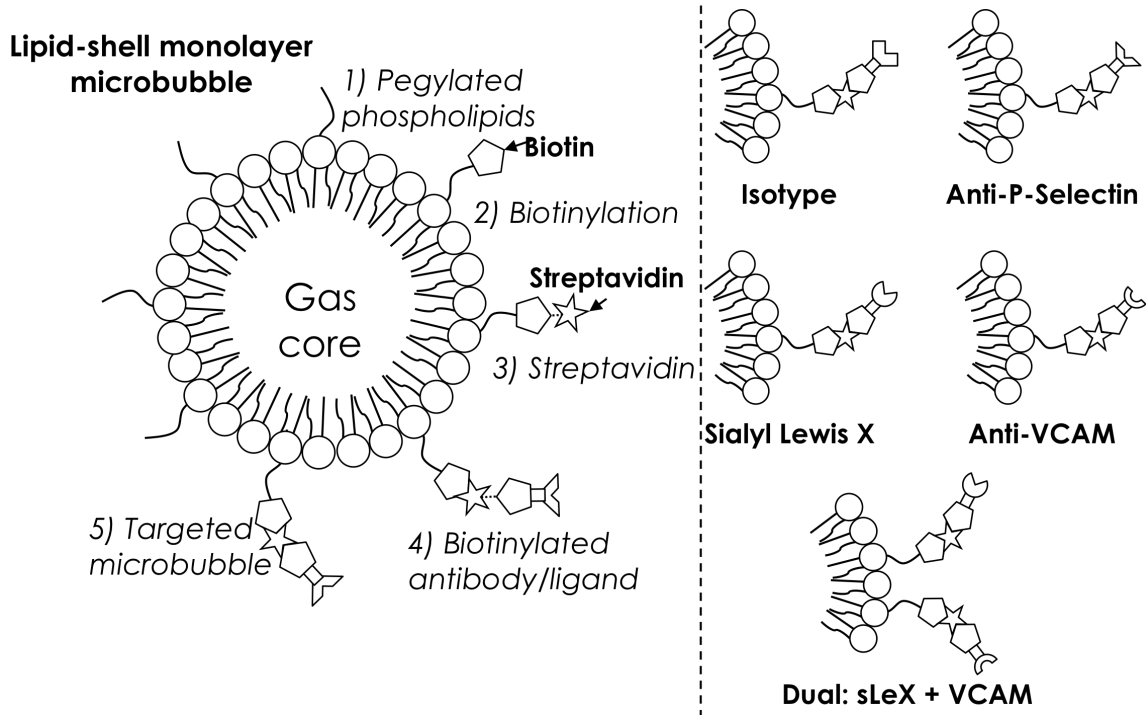


Figure 5.2: Conjugation of targeted ultrasound microbubble. Specific ligand of interest are conjugated to microbubble via a biotin-streptavidin bridge. The targeted microbubble design consists of single targeted microbubbles using control anti-VCAM isotype, anti-P-Selectin, Sialyl Lewis X, anti-VCAM, and dual targeted microbubbles using Sialyl Lewis X and anti-VCAM.

### 5.2.1 Microbubble Preparation

All microbubbles used for the study were manufactured by Dr. Klibanov at the University of Virginia. The ultrasound contrast agent was prepared from decafluorobutane gas coated with a lipid monolayer of 1,2-dioctadecanoyl-sn-glycero-3-phosphocholine (DSPC) and PEG stearate stabilizer (Figure 5.2). The process of conjugating ligands to microbubble has been described previously

(Ferrante 2009). Briefly, biotinylated PEG-PE was added to the bubble shell. A streptavidin bridge technique was used for biotinylated ligand of interest: Sialyl Lewis X (Glycotech, Gaithersburg, MD), anti-P-Selectin (CD62P, BD Pharmingen), anti-VCAM (CD106, BD Pharmingen), and anti-VCAM isotype (IgG2a k Isotype Control, BD Pharmingen).

### **5.2.2 Animal Imaging**

All animal experiments in this study followed a protocol approved by the University of Virginia Animal Care and Use Committee. Ten C57BL/6 mice (Jackson lab, Male, 8- to 12-wk old, 22 to 26 g) were used in the experiment. All mice underwent ischemia/reperfusion injury via 15 minutes occlusion of the left anterior descending (LAD) coronary artery followed by 2 hours reperfusion. After 2 hours of reperfusion, hearts of the closed-chest mice were imaged in long-axis with a Siemens Sequoia 15L8 transducer at 14 MHz. Imaging was performed in Contrast Pulse Sequences (CPS) mode with mechanical index of 0.2. Each mouse received 3 of 5 microbubble preparations in random order: anti-P-selectin (MB<sub>P</sub>), Sialyl Lewis X MB (MB<sub>X</sub>), anti-VCAM MB (MB<sub>V</sub>), Sialyl Lewis X + anti-VCAM MB (MB<sub>D</sub>), and isotype control MB (MB<sub>I</sub>). Microbubble concentrations were approximately  $200 \times 10^6/\text{mL}$ . Each microbubble administration consisted of 4 minutes of constant infusion of 100  $\mu\text{L}$  at a rate of 25  $\mu\text{L}/\text{min}$  via a 27 gauge needle tail vein catheter. After 4 minutes, the microbubble were allowed to circulate for another 3 to 4 minutes in the system, and finally the microbubbles were destroyed in burst mode with a bursting mechanical index of 1.9 for 1 minute. After imaging,

mouse hearts were excised and stained with triphenyltetrazolium chloride (TTC)/Phthalo blue dye to assess area at risk. An outline of data acquisition is shown in Figure 5.3 (panels 1 to 3).

Video cines were post-processed in MATLAB (Mathworks, Natick, MA). Regions of interest were placed around the myocardium and signal intensities were retrieved to determine regional time intensity curves of the myocardium. Myocardial intensity profiles during infusion was compared to histological staining results. Under TTC/Phathlo blue stain, normal myocardium produces a blue hue, while ischemic area at risk exhibits a red hue. To assess area at risk, red intensity level is plotted from the staining results and a threshold is selected to distinguish normal myocardium from ischemic myocardium (see Figure 5.3, panel 3). Histological stains were treated as “gold standard”, and used to assess the accuracy of the targeted microbubble signal as the basis of a diagnostic method using a receiver-operating characteristic (ROC) analysis (Figure 5.3, panel 6).

To quantify the significance of differences between control isotype microbubble and targeted microbubbles, Student t-tests and one-way analysis of variance (ANOVA) were performed. Normalized intensity values are reported as mean  $\pm$  standard deviation.

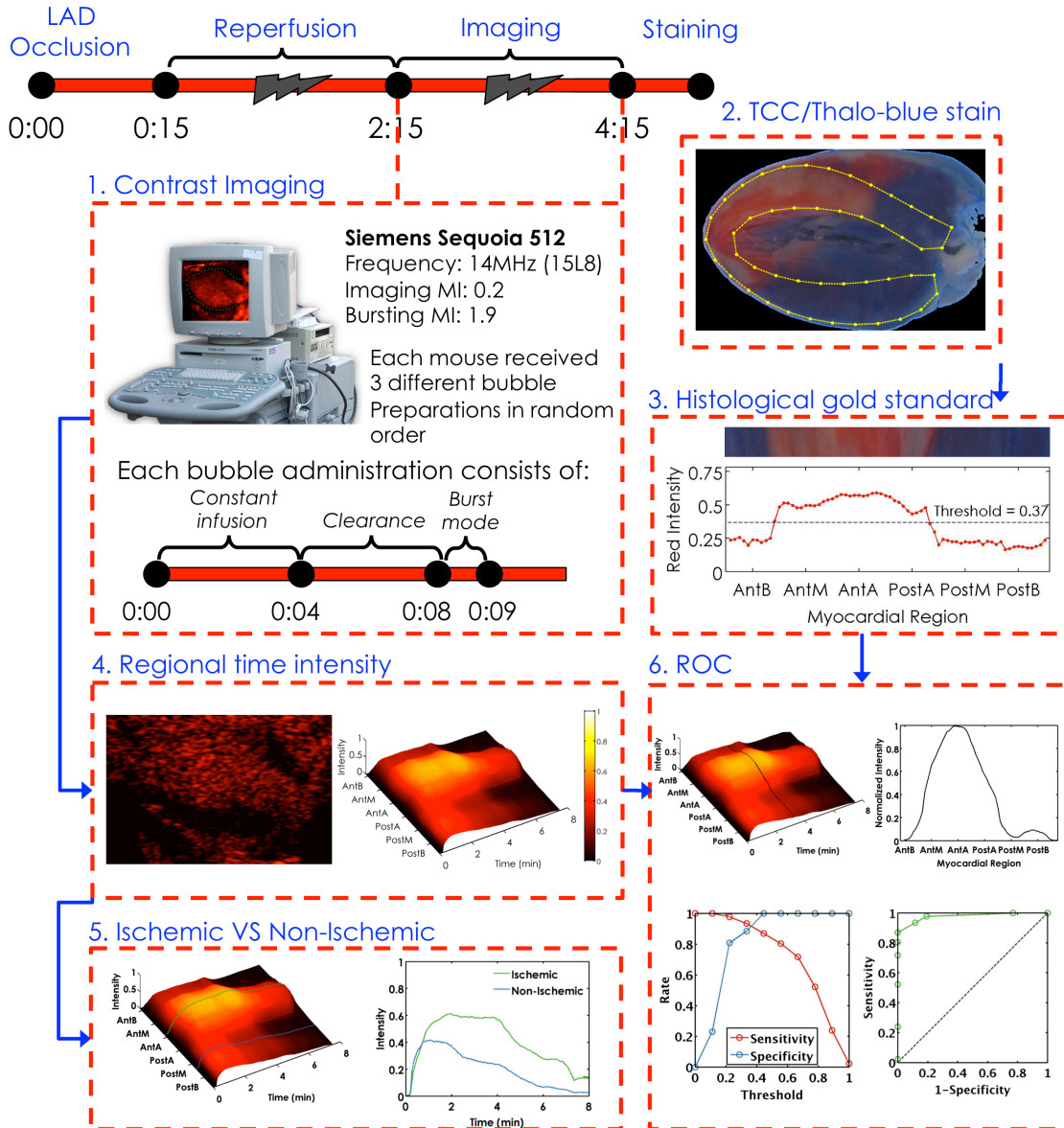


Figure 5.3: Timeline and signal processing of molecular imaging experiment. Mice underwent ischemia/reperfusion injury via 15 minutes occlusion of the left anterior descending (LAD) coronary artery followed by 2 hours reperfusion. Mice were imaged with a Sequoia 15L8 transducer at 14 MHz (panel 1) and video data were processed offline to arrive at regional time intensity curve (panels 4 and 5). Video data were compared to histological stains (panels 2 and 3) to assess the accuracy of targeted microbubbles using ROC analysis (panel 6).

### 5.3 RESULTS

All ten mice survived the 15 minutes LAD occlusion followed by 2-hours reperfusion, and recovered from surgery for ultrasound contrast imaging after the 2-hour reperfusion. While TTC/Phthalo blue stains indicate significant ischemic myocardial injury from the 15 minutes LAD occlusion, there were also infarcted myocardial tissues. However, infarcted myocardial tissues were small when compared with the ischemic area at risk.

One concern over constant infusion is the change in microbubble concentration and diameter during the duration of infusion. Microbubbles suspended in a syringe will float to the top due to its buoyancy, thus leading to change in concentration. Additionally, gas exchange with surrounding medium can result in reduction in microbubble diameter. Both microbubble concentration and diameter can affect image intensity during imaging. An *in vitro* experiment was carried to determine whether the changes in microbubble concentration and diameter were significant during constant infusion. Figure 5.4 plots the microbubble concentration and diameter over several constant infusion trials, where microbubbles were being released from a syringe at a constant rate (25  $\mu\text{L}/\text{min}$ ) over 15 minutes. Microbubble concentration and diameters were measured several times using a Coulter Counter (Beckman Coulter, Brea, CA). Over the course of constant infusion, both microbubble concentration and diameter decreased. However, within the initial first 4 minutes of the infusion, corresponding to the protocol for *in vivo* animal imaging, the decrease was insignificant and both

microbubble concentration and diameter were within 90% of their original measurements.

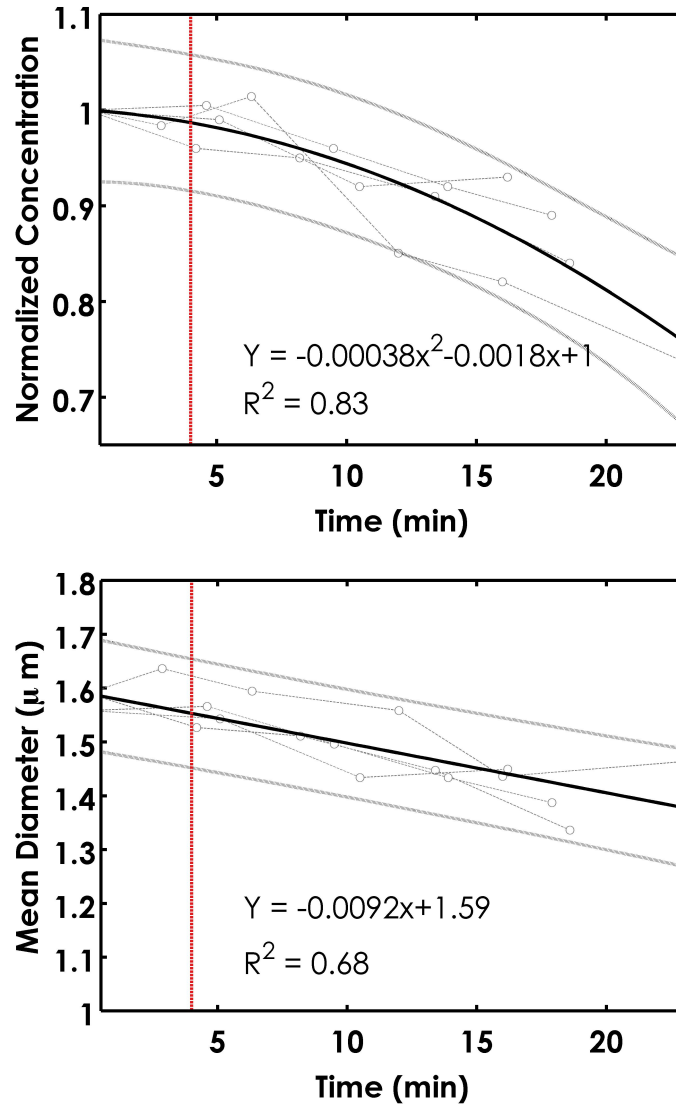


Figure 5.4: Normalized microbubble concentration (top) and mean diameter (bottom) from *in vitro* constant infusion experiments. Both microbubble concentration and diameter decreases over time but the change is insignificant over the first 4-minute of the infusion.

Normalized intensities, plotted as the ratio of intensity in the ischemic region to the intensity in the non-ischemic region, are shown in Figure 5.5. Normalized intensities are significantly higher for MB<sub>D</sub>, MB<sub>X</sub>, MB<sub>P</sub>, and MB<sub>V</sub>, compared to MB<sub>I</sub> (p<0.05). Furthermore, normalized intensity for MB<sub>D</sub> is higher than MB<sub>X</sub>, MB<sub>P</sub>, and MB<sub>V</sub> (p<0.05). For MB<sub>I</sub>, normalized intensity ratio is close to 1.0, signifying that the ischemic and non-ischemic regions of the myocardium were equally perfused with microbubble, and there was no sign of microbubbles binding in the ischemic regions. Using MB<sub>D</sub>, microbubbles signals in the ischemic regions were two times greater than signals in the non-ischemic regions.

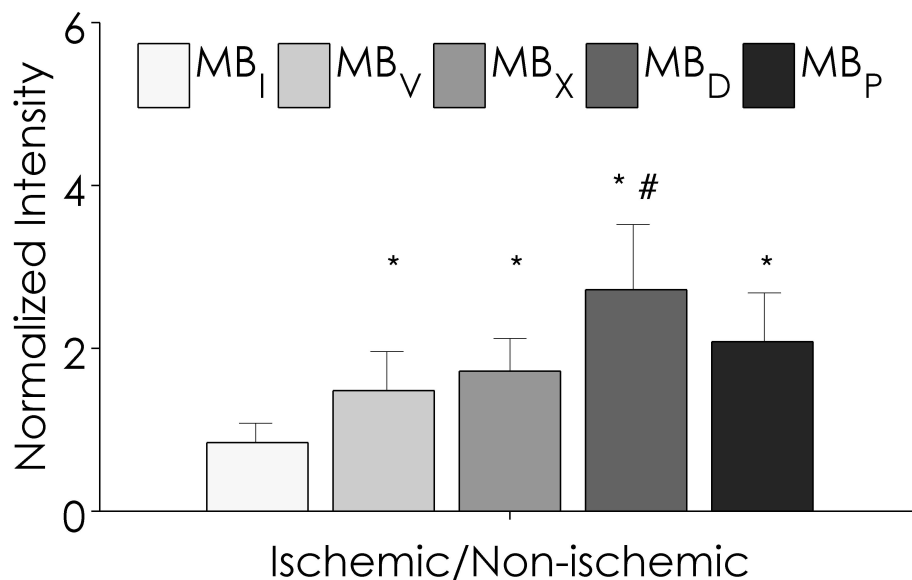


Figure 5.5: Normalized intensities, plotted as the ratio of intensity in the ischemic region to the intensity in the non-ischemic region. (\* P < 0.05 compared to MB<sub>I</sub>, # P < 0.05 compared to MB<sub>V</sub>, MB<sub>X</sub>, and MB<sub>P</sub>)

Receiver operating characteristic curves are illustrated in Figure 5.6. Using TTC/Pthalo dye as the “gold standard”, MB<sub>V</sub> produced the best performance in terms of accurately describing both ischemic and non-ischemic regions, possessing an area under the curve (AUC) of 0.97. MB<sub>D</sub> (AUC = 0.90), MB<sub>X</sub> (AUC = 0.89), and MB<sub>P</sub> (AUC = 0.87), yielded similar AUC performances and all were significantly less than MB<sub>V</sub>.

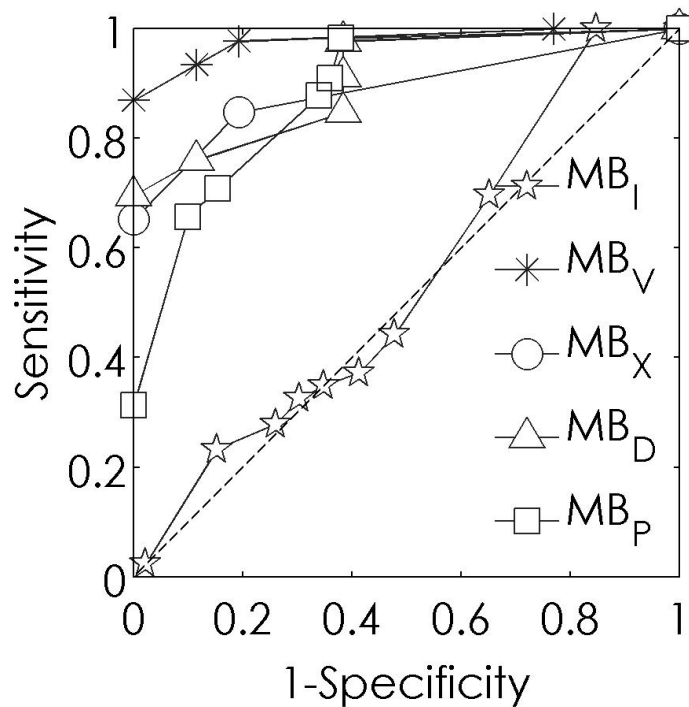


Figure 5.6: ROC curves using histological stain as the gold standard showed accurate detection of both ischemic and non-ischemic regions using MB<sub>D</sub> (AUC = 0.90), MB<sub>X</sub> (AUC = 0.89), MB<sub>P</sub> (AUC = 0.87), and MB<sub>V</sub> (AUC = 0.97).

## 5.4 DISCUSSION

The use of ultrasound contrast agents as molecular biomarkers not only assists in the improved understanding of the biological processes during inflammation, but also has the potential for early detection of disease. In this work, modified microbubbles targeted to single and dual biomarkers enables ultrasound-mediated molecular imaging via constant infusion. The main finding of this study is that myocardial ischemic/reperfusion injury can be identified with ultrasound microbubbles. It has been shown that microbubble targeted to the P-Selectin and VCAM adheres to inflamed endothelium after ischemic/reperfusion injury in the myocardium, and therefore can detect ischemic area at risk. This is the first work showing targeting of ischemic area at risk using dual targeted microbubbles mice using ultrasound, and imaged closed-chest.

For small animal coronary high resolution arterial imaging, microbubble signals must be detectable in the higher frequency range, and transducers would need to be able to detect microbubble response at these higher frequencies. Optimization of targeted microbubble design is needed to increase binding to the target and maximize contrast signal. In this work, we studied a dual targeted microbubble motif to increase binding efficiency of microbubbles to its targets. The relative proportions of ligands in dual targeted microbubble were previously studied *in vitro* (Ferrante 2009), and used for *in vivo* study for this project.

Another approach to increase binding efficiency of microbubble is to utilize ultrasound acoustic radiation force to push microbubbles to their target (Zhao 2004;

Lum 2006; Frinking 2012; Gessner 2012). In high blood flow environments, such as the coronary arteries, high shear stress can cause detachment of microbubble from receptors on the endothelial wall (Talkakar 2004). Acoustic radiation force can push microbubble to the endothelial wall and slow down microbubble velocity to increase binding efficiency (Zhao 2004; Frinking 2012). Another limitation of our study was the difficulty in inducing ischemia/reperfusion injury without causing myocardial infarction. TTC staining results showed noticeable, but limited, area of infarction in the myocardium. Reduction in duration of LAD occlusion, from 15 minutes to 10 minutes, may help mitigate this limitation.

Molecular imaging of endothelial cell adhesion molecules in closed-chest mice is possible using constant infusion of microbubbles. Dual-targeted microbubbles yield greater microbubbles signals than single-targeted microbubbles when delivered using constant infusion, improving both the sensitivity and accuracy of this technique to measure risk regions in intact mice. The performance of single-targeted microbubbles depends on the ability of the targeted microbubble to bind a single receptor, whereas the performance of multi-targeted microbubbles is based on the combination of receptors and the ratios of ligands attached to the microbubbles. Another advantage of dual targeted microbubbles is the improved potential for microbubble binding when endothelial receptor expression is unknown. One explanation for the improved signal of dual targeted microbubbles is the mechanism of leukocyte rolling and adhesion as mediated by P-Selectin and VCAM. For example, Sialyl Lewis X ligand bound to the microbubble can bind to P-

Selectin quickly, however the binding strength is weak, resulting in a rolling mechanism. To stabilize the microbubble, anti-VCAM is added to the microbubble to provide firm binding (Tamatani 1995; Weller 2005; Beauharnois 2005; Ferrante 2009).

Identification ischemic/reperfusion injury in the myocardium using ultrasound will enable not only the identification of previously ischemic myocardium but also provide an estimate of the location and spatial extent of the ischemia. The proven ability to detect myocardial ischemia, using ultrasound contrast molecular imaging, in patients with ambiguous symptoms would be a useful contribution to clinical practice.

# Chapter 6: Modeling Human Arterial Wall Motion With *In Vivo* Validation Using High Frequency Ultrasound

## 6.1 INTRODUCTION

Arterial stiffness has been shown to be a predictor of cardiovascular events and pulse wave velocity, a measure of arterial stiffness, has been shown to be correlated with clinical outcomes (Howard 1993; O'Leary 1999; Gibbons 2008; Juonala 2008). The ability to measure changes in the mechanical properties of an arterial vessel wall may therefore enable detection of early manifestations of cardiovascular disease. In this study, high frequency (30MHz) ultrasound was used to scan human common carotid arteries, in order to determine arterial wall motion as a measure of arterial stiffness.

Atherosclerosis is characterized by the deposition of fats and cholesterol in the arterial wall. This causes hardening of the vessel and the formation of plaques, which narrow the vessel lumen. Ultimately, these plaques are at risk of rupture and erosion leading to luminal thrombosis and ischemia of downstream tissue beds. While there are many risk factors for plaque formation, local hemodynamics have been shown to play an important role as it has been shown that atherosclerotic lesions tend to develop in regions near arterial bifurcations, where turbulent flow results in low shear stress (Malek 1999; Sho 2004). Unfortunately, the coronary and carotid arteries are common sites for plaque formation resulting in the high incidence of ischemic heart and brain disease. Consequently, the ability to

noninvasively diagnose atherosclerosis at an early stage is highly desirable in order to provide time to intervene.

Arterial intima-media thickness (IMT) is a known marker for atherosclerosis and has been used to assess patient risk for cardiovascular diseases (O'Leary 1999). Arterial IMT can be measured using high-resolution B-mode ultrasonography and can evaluate the physical properties of blood vessels *in vivo* (Howard 1993). B-mode images are normally used to measure lumen diameter, IMT, and the presence of arterial plaque. Thickness of arteries naturally increases with age and significant differences in IMT are observed between men and women (Juonala 2008). Furthermore, the magnitude of the relationship between IMT and cardiovascular disease risk significantly decreases when more traditional risk factors (diabetes, hypertension, smoking) are taken into account (Bots 2007).

The development of atherosclerosis stiffens an artery via an increased breakdown of elastin, and an overproduction of collagen, neither of which cause an immediate change in IMT (Zieman 2005). As a result, arterial stiffness may be more desirable than IMT as an early indicator for atherosclerotic disease, since changes in arterial physical properties generally occur before geometrical remodeling. While there are many *in vivo* ultrasound imaging techniques for quantifying arterial stiffness, they are not widely used as clinical tools for patient diagnosis and follow-up. This is probably due to the fact that existing methods rely on pulse pressure and changes in lumen diameter over the cardiac cycle, which

can be difficult to measure, to estimate stiffness (Dart 2001; McEniery 2006; Mannucci 2006).

In this work, high frequency ultrasound is used to acquire high-resolution images of the carotid artery wall over multiple cardiac cycles. By applying speckle tracking algorithms to the images, arterial wall motion can be estimated, which in turn can be used to derive mechanical properties such as arterial wall stiffness. Several studies have reported on the viscous and elastic properties of arterial wall in both humans and animals (Bauer 1979; Armentano 1995a; Armentano 1995b). In this chapter, a mathematical model of wall motion based on viscoelastic properties of the carotid arterial wall is used to describe the motion dynamics derived from the ultrasound images.

## **6.2 METHODS**

### ***6.2.1 Ultrasound Estimation of Wall Motion***

A 30 MHz linear array transducer connected to a high frequency ultrasound scanner (VEVO 2100, VisualSonics, Ontario, Canada) was used to image human common carotid arteries. In addition, the human common carotid is approximately 1.5 cm below the skin and is well within the penetration depth of the ultrasound scanner at this frequency. Ultrasound gel was applied on the lateral side of the subject's neck, approximately 4cm above the collarbone. The imaged regions correspond to the common carotid just prior to the bifurcation into external and internal carotids. All ultrasound images were captured while the subjects were

standing. The focus of the transducer was placed at the distal carotid wall in order to minimize image artifacts, such as reverberation (Figure 6.1). Two dimensional B-mode cines were captured at approximately 200 frames per second. The cine images were stored for offline processing. Speckle tracking was performed using MATLAB (Mathworks, Natick, MA) on the raw RF data via a normalized cross correlation method. A 0.1 mm x 0.4 mm (axial by lateral) tracking block size was used.

$$\frac{d^2r}{dt^2} = \left( P_w + \frac{E}{r_0} \right) \left( \frac{r_0}{\rho r^2} \right) - \frac{1}{\rho r^2} \left[ \eta \frac{dr}{dt} + E + \frac{\eta_w h}{r} \frac{dr}{dt} \right] - \frac{1}{r} \left( \frac{dr}{dt} \right)^2 - \frac{1}{\rho r} [P_w + P(t)] \quad (1)$$

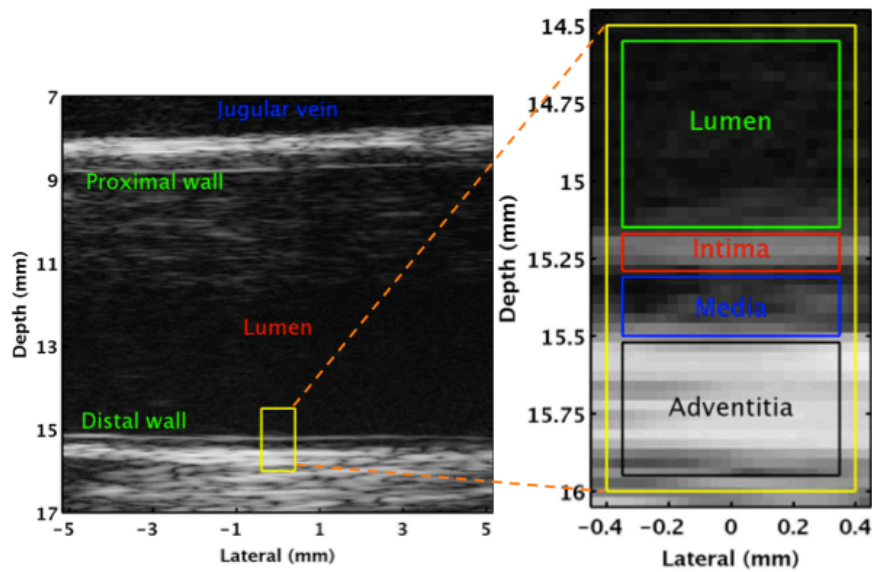


Figure 6.1: B-mode image of the common carotid artery. Image on the right is a magnified view of the yellow rectangular region, showing the intima (the bright band touching the vessel lumen), the media (the dark band below the intima), and the adventitia/surrounding tissue. The transducer was focused at the distal wall, as tracking of the proximal wall was impeded by signal artifacts.

### 6.2.2 Viscoelastic Model of Wall Motion

Since the arterial wall is mostly composed of smooth muscle, elastin fibers, and collagen, a viscoelastic model (Zamir 2000) of wall motion was determined to be most appropriate. With this model, radial motion dynamics ( $r$ ) are simulated as (1), where  $E$  is the wall elastic modulus,  $\eta_w$  is wall viscosity,  $\eta$  and  $\rho$  are the viscosity and density of blood, and  $P(t)$  is the pressure waveform due to blood flow. The pressure waveform was generated by fitting a series of Gaussian functions with varying delays ( $\tau_i$ ), amplitudes ( $A_i$ ) and spread ( $\varpi_i$ ), over the blood velocity profile obtained from pulsed wave Doppler (Figure 6.2).

$$P(t) = \sum_{i=1}^n \left\{ A_i \text{Exp} \left[ \left( \frac{t - \tau_i}{\varpi_i} \right)^2 \right] \right\} \quad (2)$$

The mean error between the speckle tracking results ( $r_s$ ) and the simulated results ( $r_m$ ) were computed as:

$$\text{error} = \frac{\int_{t_i}^{t_f} \frac{|r_s - r_m|}{r_{\max}} dt}{t_f - t_i} \quad (3)$$

where  $r_{\max}$  is the maximum speckle tracking result, and  $t_i$  and  $t_f$  are the starting

and ending time of the tracked cardiac.

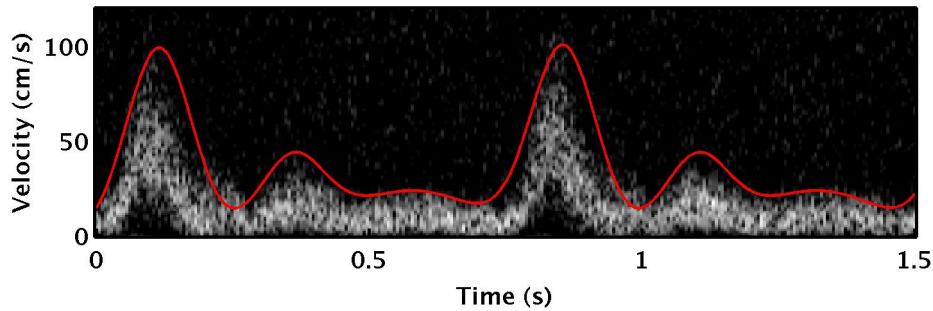


Figure 6.2: Blood flow velocity measured in the center of common carotid artery using pulse wave Doppler. The red curve is a representative pressure waveform derived from a series of Gaussian functions over the velocity profile.

### 6.3 RESULTS

The common carotid artery of a 25-year-old, male was selected for the example summarized below. The subject had no prior history of cardiovascular disease and was normotensive. During imaging, the subject's heart rate was approximately 78 beats per minute.

Arterial wall motion was tracked from end-diastole (when lumen diameter is at its smallest) to end-systole (when vessel is dilated) and back to end-diastole. Radial displacement peaked slightly above 3mm at end-systole in the intima, and it is not significantly different from peak radial displacement in the adventitia. However, the magnitude of displacement vectors along the intima was  $0.54 \pm 0.03$  mm, and  $0.46 \pm 0.04$  mm along the adventitia. Figure 6.3 illustrates the displacement vectors along different layers of the distal carotid wall, with the background B-mode image of the carotid taken at end-systole.

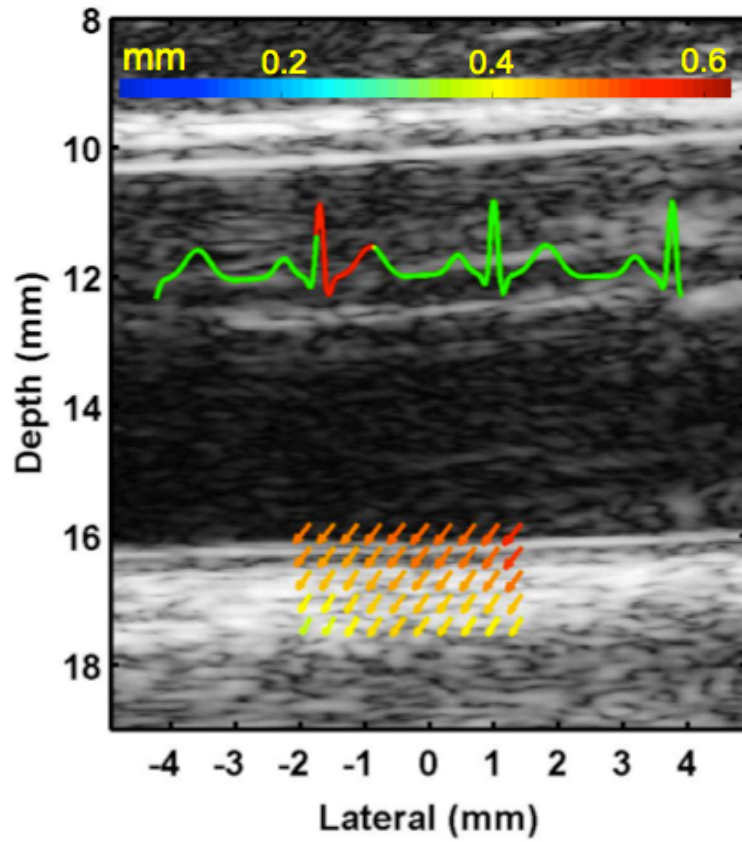


Figure 6.3: Displacement field of distal carotid wall derived using 2D RF speckle tracking. Displacement vectors are color-coded based on magnitude (scale bar shown at the top). The green curve is the ECG trace and tracking was performed from end-diastole to end-systole (portion of the ECG curve shown in red).

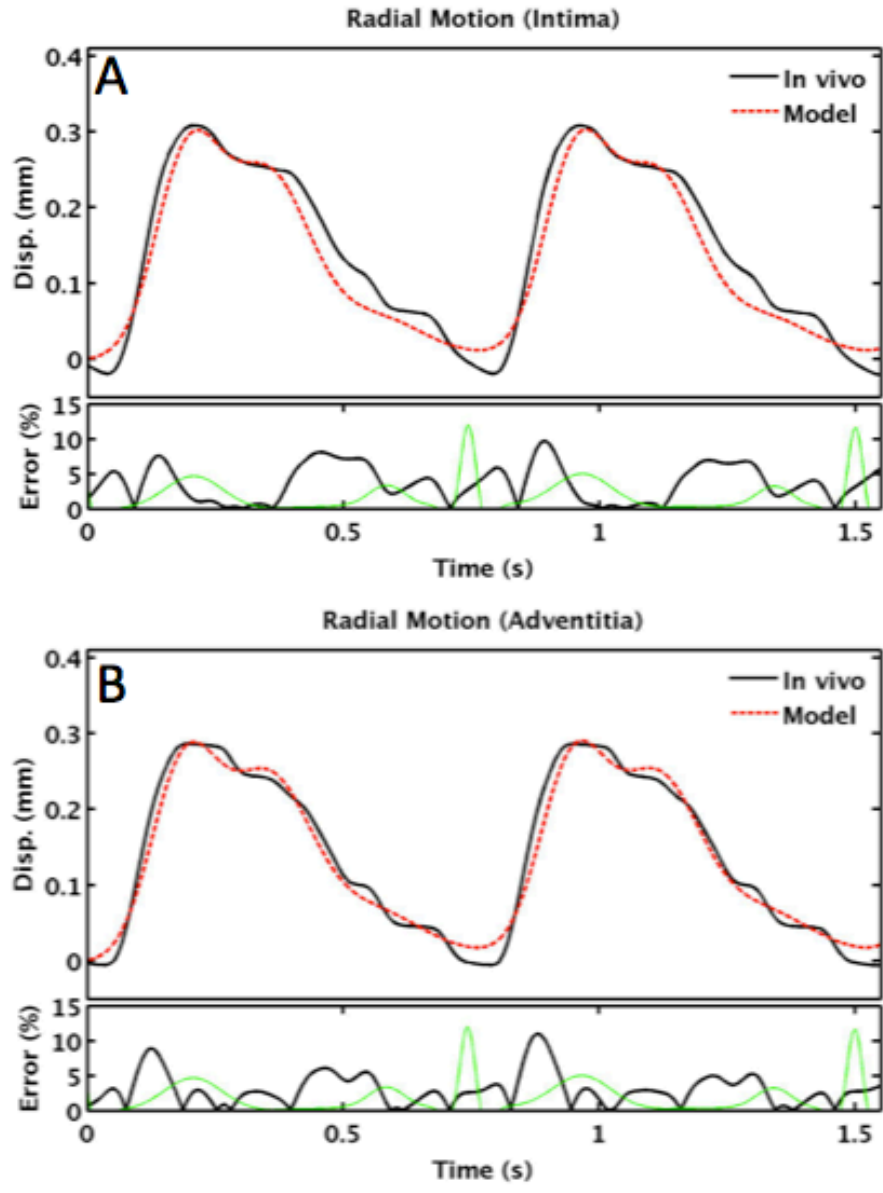


Figure 6.4: Comparison of arterial radial displacement using speckle tracking (black lines) and model simulation (dotted red lines) for points in the intima (top) and adventitia (bottom). Subpanel below each graph shows the absolute percent error (black), and ECG tracing in green.

The wall motion model was solved numerically using MATLAB. Simulation results closely matched *in vivo* speckle tracking results for motion within the intima (Figure 6.4a) and adventitia (Figure 6.4b). The input pressure waveform comprised a series of 3 Gaussian functions based on the blood velocity profile obtained using pulsed wave Doppler (Equation 2). Percent absolute error, calculated based on the ratio of absolute difference between model and *in vivo* results to the peak displacement obtained from *in vivo* tracking, is less than 10% along all points in the cardiac cycle. Mean absolute error over the two cardiac cycles was less than 4% for points in the intima (Figure 6.4a) and adventitia (Figure 6.4b). No significant difference in radial motion magnitude was observed between the intima and adventitial layers.

## 6.4 DISCUSSION

A model for arterial radial motion has been described and an initial validation with *in vivo* speckle tracking results is presented. While the model accurately predicts wall motion as estimated by speckle tracking, no difference in radial motion was seen between the intima and adventitia, suggesting a lack of radial strain in arterial wall motion.

Currently, the model utilizes a pressure waveform consisting of a series of 3 Gaussian functions as its input. The large diameter of the human common carotid makes it susceptible to turbulent flow, particularly near the carotid bifurcation. Furthermore, flow reversal near the end of diastole results in slight negative

displacement. As may be observed in Figure 6.4, displacement immediately following the R-wave is slightly negative, but the model does not capture this phenomenon. This might be improved in future implementations by using a more accurate tracing of velocity profile, instead of the functional approximation used here.

Arterial stiffness is associated with cardiovascular risk (O'Leary 1999; Howard 1993; Juonala 2008); however, only a few studies have investigated the prognostic value of stiffness in the radial direction (Blacher 1998; Dijk 2005; Stork 2004). The ability to model radial motion and derive mechanical properties, such as the parameters shown in equation (1), can provide valuable information on the health of the arterial wall. In response to cardiovascular risk factors, it has been shown that longitudinal stress decreased in large extent, and might be an earlier and more sensitive measure of vascular remodeling than radial motion (Humphrey 2009). However, longitudinal motion has been previously neglected as the motion was below the resolution limit of earlier ultrasound scanners (Nichols 2005). Recent advances in high frequency ultrasound, however, have allowed longitudinal motion to be detected and measured (Cinthio 2005). An extension of the model to include longitudinal motion would provide a comprehensive understanding of the arterial motion dynamics in diseased arteries.

# Chapter 7: A Phase-based Motion Estimation Technique for Mouse cardiac Function Using Monogenic Signal and High Resolution Ultrasound

## 7.1 INTRODUCTION

Regional tissue motion estimation using medical ultrasound images is an important first step in solving many problems with significant clinical applications that include non-invasive assessments of myocardial function in echocardiography. Many existing techniques for estimating motion are based on block-matching using B-mode image intensity, and phase information is often neglected. In digital image processing, it is widely accepted that the information carried in the image phase is more important than information carried by its amplitude. In this work, I implemented a phase-based tracking technique using the monogenic signal to estimate cardiac motion in both synthetic and *in vivo* mouse heart data.

Despite the sophistication of modern imaging techniques, they are sometimes unreliable due to system limitations and/or physical and physiological limitations of the subjects. Quantification of mouse cardiac function via ultrasound speckle tracking is often compromised due to fast respiration (~100-160 bpm under anesthesia) that introduces motion artifacts; rapid heart rate (~400-600 bpm under anesthesia) that requires high temporal resolution; and a small heart size (approximately 5 mm x 6 mm for the mouse left ventricle) that requires high spatial resolution. High temporal and spatial resolutions can be achieved with current state-of-the-art high-resolution ultrasound scanners. However, there is

always a trade-off between spatial and temporal resolutions. Combined respiration and ECG gating is not always reliable, and acquisition of multiple heart cycles is often necessary to minimize motion artifacts.

Furthermore, signal shadowing due to the sternum and signal reverberation due to the ribs are persistent challenges in mouse echocardiography. Existing methods for motion estimation via ultrasound speckle tracking are often noisy and are error-susceptible due to the aforementioned image artifacts. Several approaches have been proposed to increase the accuracy of cardiac motion estimations. One approach is to introduce mathematical models that impose geometric constraints (e.g. myocardial incompressibility) to correct for improbable tracked motion (Lin 2011; Bistoquet 2008; Mansi 2010; Wang 2010). As discussed in chapter 3, another category of approach is by decreasing signal artifact via finite impulse response filters (Lediju 2009) or isolating stationary signals (e.g. reverberation) from moving myocardial signals via principal component analysis (Mauldin 2011).

While these methods have been shown to improve tracking accuracy, conventional traditional speckle tracking analysis methods are innately susceptible to error because they are based on block-matching using image pixel amplitudes, and disregard phase information. It is widely appreciated that image signal phase carries additional information beyond that available using only signal amplitude. There is also evidence that the human visual system uses phase information for detection and discrimination of objects (Fechler 2002). Phase-based motion

estimation techniques have shown promise for cardiac application using magnetic resonance imaging (Xiaomei 2010), and have been used to estimate tissue elasticity in ultrasound elastography (Tanguy 2010). In this work, I will show a phase-based estimation technique for tracking myocardial motion using the monogenic signal and high frequency ultrasound.

## 7.2 METHODS

### 7.2.1 The Monogenic Signal

The analytic signal, a complex representation, of a real signal is important for signal processing where amplitude and phase information can be retrieved. For a 1D signal, the analytic representation is obtained by calculating the Hilbert transform. Analytic representation for 2D or higher dimensional signals is not trivial. Felsberg *et al.* (Felsberg 2001) have developed a generalized approach for n-dimension analytical signal via the monogenic signal.

A monogenic signal has three components and is obtained by designing a spherical quadrature filter (SQF). The SQF obtained by a composite of a radial bandpass filter (RBF), which is an even filter that yield the real part of monogenic signal, and a Riesz transform of the bandpass filter to yield the two imaginary parts of the monogenic signal.

The RBF is constructed using a 2D difference of Gaussian functions (an even filter  $H_e$ , Figure 7.1) in the spatial frequency domain ( $u_1, u_2$ ):

$$r^2 = u_1^2 + u_2^2, H_e(u_1, u_2) = \exp\left(-\frac{(r-r_0)^2}{\sigma_0^2}\right) - \exp\left(-\frac{(r-r_1)^2}{\sigma_1^2}\right) \quad (1)$$

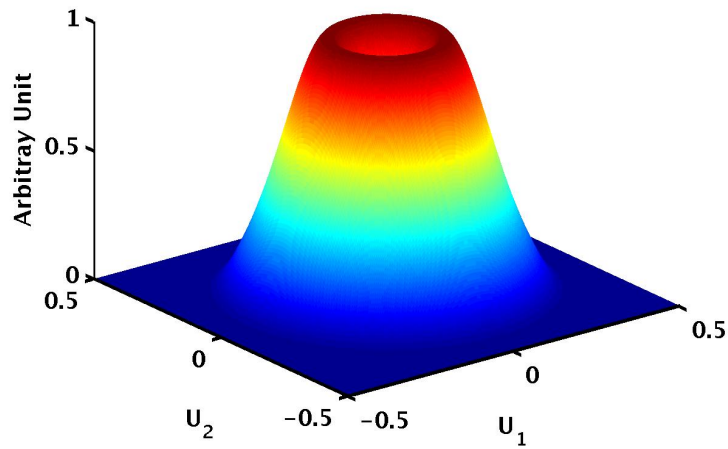


Figure 7.1: Surface of the RBF constructed using difference of Gaussian functions. RBF is an even filter and radially symmetric. The goal of this filter is to maintain the main characteristics of the image structure within a defined range of frequency.

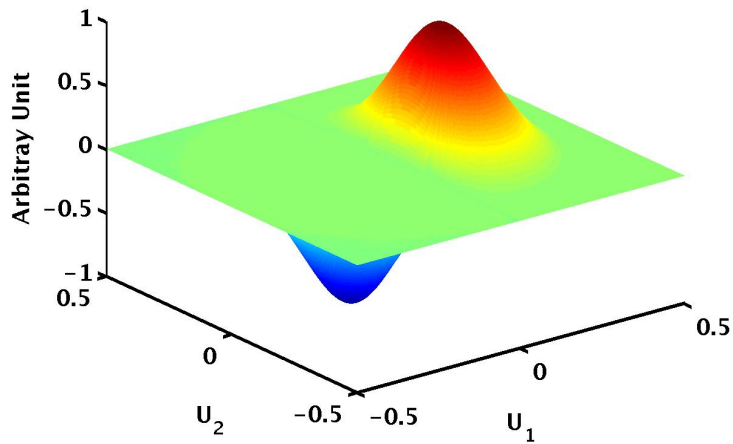


Figure 7.2: The Riesz transform of the RBF is an odd filter that yields two monogenic components important to calculating phase. The real part of the filter is shown in the surface above.

The goal of RBF is to localize the image structure to a certain frequency range as defined by the centroids,  $r_0$  and  $r_1$ , and the spreads,  $\sigma_0$  and  $\sigma_1$ .

To complete the SQF (Figure 7.2), the Riesz transform of RBF is computed using an odd filter ( $H_o$ )

$$H_o(u_1, u_2) = \frac{u_1 + ju_2}{r} \quad (2)$$

The monogenic signal of an image ( $I$ ) in the frequency domain has the following components:

$$\begin{aligned} p &= H_e I \\ q_1 &= \text{real}(H_o H_e I) \\ q_2 &= \text{imag}(H_o H_e I) \end{aligned} \quad (3)$$

Valuable information can be extracted from this monogenic signal. Its amplitude  $A$  is calculated using:

$$A = \sqrt{p^2 + q_1^2 + q_2^2} \quad (4)$$

Orientation,  $\theta$  and phase,  $\varphi$ , data are calculated using:

$$\theta = \tan^{-1}\left(\frac{q_2}{q_1}\right) \quad (5)$$

$$\varphi = \tan^{-1}\left(\frac{q_1 \cos(\theta) + q_2 \sin(\theta)}{p}\right) \quad (6)$$

The relationships between amplitude, orientation and phase from equations 4 to 6 can be simplified using:

$$\begin{aligned}
 p &= A \cos(\varphi) \\
 q_1 &= A \sin(\varphi) \cos(\theta) \\
 q_2 &= A \sin(\varphi) \sin(\theta)
 \end{aligned}
 \tag{7}$$

### 7.2.2 Synthetic Mouse Heart Data

Synthetic mouse heart data are simulated using Field II. Short-axis mouse heart geometry is generated using 2 concentric circles. Random scatterers are assigned between the circles and are designated as myocardium (Figure 7.3). To apply myocardial motion, an incompressible constraint is enforced (Lin 2011) for a single 50-frame heart cycle starting from end-diastole (Figure 7.4).

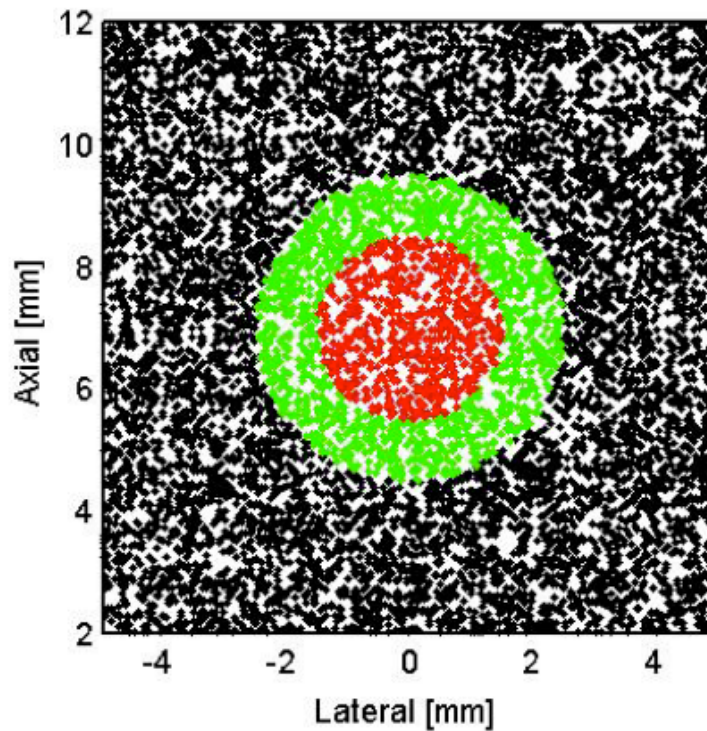


Figure 7.3: Random scatterers used for simulating a short-axis view of the left ventricle (Black = surrounding tissues, green = myocardium, red = blood).

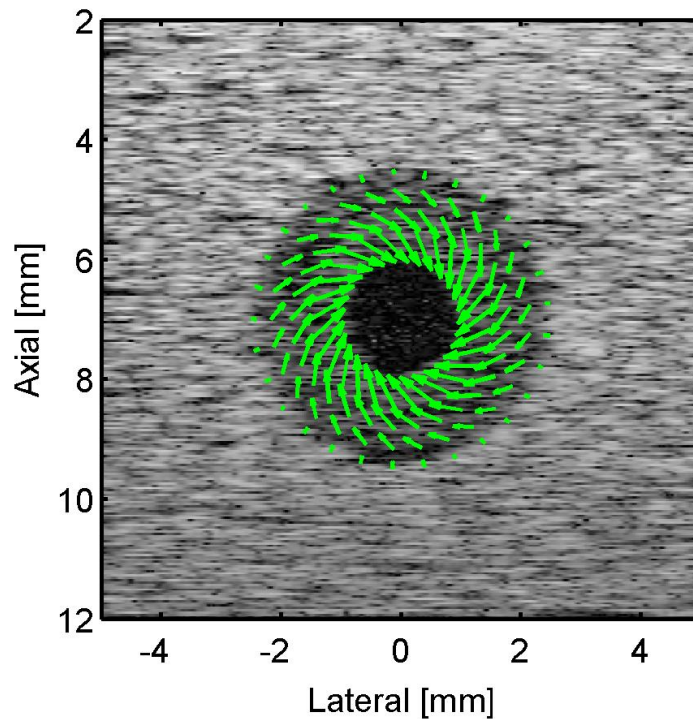


Figure 7.4: Synthetic B-mode image simulated with Field II. Green displacement vectors is shows motion from end-diastole to end-systole, and is enforced using an mathematical model based on myocardial incompressibility.

### ***7.2.3 In Vivo Mouse Heart Data Acquisition***

Short-axis cine B-mode images of C57BL/6 mice were acquired using VisualSonics Vevo2100 scanner with a transducer operating at 30MHz. The transducer has a spatial resolution of  $50 \mu\text{m}$  axially and  $110 \mu\text{m}$  laterally. During scanning, body temperature was maintained at  $37 \pm 0.2^\circ\text{C}$  with the aid of a digital rectal thermometer, a heated plate on which the animal lay, and an external lamp heat source.

#### 7.2.4. Speckle Tracking (MSAD)

Myocardial displacements were estimated between 2 subsequent image frames by translating pixel block over a predefined search region using MSAD algorithm (Li 2009) as previously described in chapter 2.

#### 7.2.5 Displacement Estimation via the Monogenic Signal

Displacement between two frames is estimated using optical flow method based on the phase difference between the two frames (Felsberg 2004). To relate two adjacent images ( $I_1$  and  $I_0$ ) using displacement ( $d$ ) for each pixel at coordinate  $x$ :

$$I_1(x) = I_0(x - d(x)) \quad (8)$$

Equation (8) can be expanded by substituting in phase information:

$$\begin{aligned} \Psi_1(x) &= \Psi_0(x - d(x)) \\ \Psi &= \varphi \cdot n \\ n &= (\cos(\theta), \sin(\theta)) \end{aligned} \quad (9)$$

Assuming small displacement field between two adjacent frames, first order series expansion leads to:

$$\Psi_1(x) = \Psi_0(x) - (n^T) d(x) \nabla \Psi_0 \quad (10)$$

Rearranging equation (10) will yield:

$$d(x) = [\Psi_0(x) - \Psi_1(x)] [(n^T) \nabla \Psi_0]^{-1} \quad (11)$$

### 7.3 RESULTS

A mathematical model was used to prescribe cardiac motion for the synthetic heart data. Circumferential and radial motions were uniformed circumferentially; however radial motion varied in the radial direction. Motion determined using MSAD tracking algorithm is shown in Figure 7.5. Displacement vectors are color-coded based on displacement magnitude. Similarly, Figure 7.6 shows the displacement vectors obtained from phase-based tracking. Tracking errors were  $3.2\pm 1.1\%$  and  $3.4\pm 1.2\%$  for phase-based and MSAD block-matching techniques, respectively. Comparing figures 5 and 6, tracked displacements on the epicardial border are noisier, and should be zero based on the model. Additionally, there is greater variability in displacement circumferentially in Figure 7.5.

Figure 7.7 compares tracking displacement through a single heart cycle using MSAD (gray) and phase-based (black) tracking techniques. Tracking error for *in vivo* mouse heart data is calculated based on the ratio of the length of final displacement vector to the length of the trajectory, and were  $5.3\pm 1.6\%$  and  $7.1\pm 2.1\%$  for phase-based and block-matching techniques, respectively.

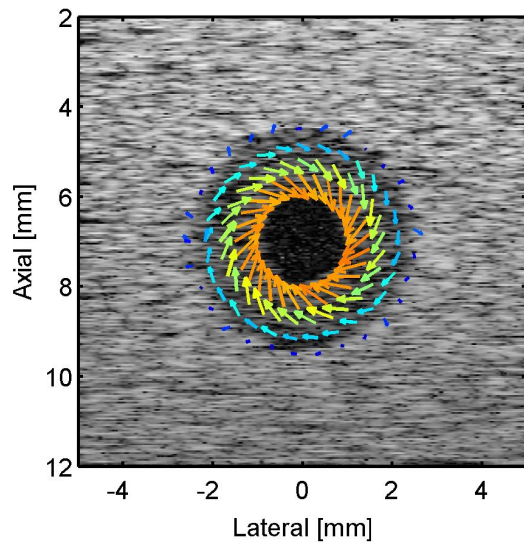


Figure 7.5: Tracked displacement vector using MSAD speckle tracking algorithm.

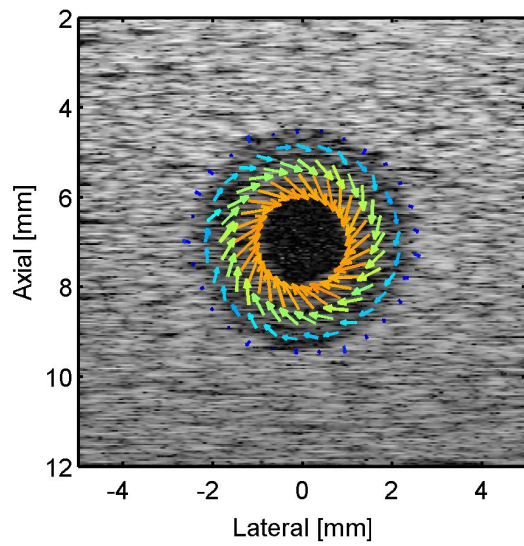


Figure 7.6: Phase-based tracking technique yields more uniform displacement vectors over MSAD block-matching technique.

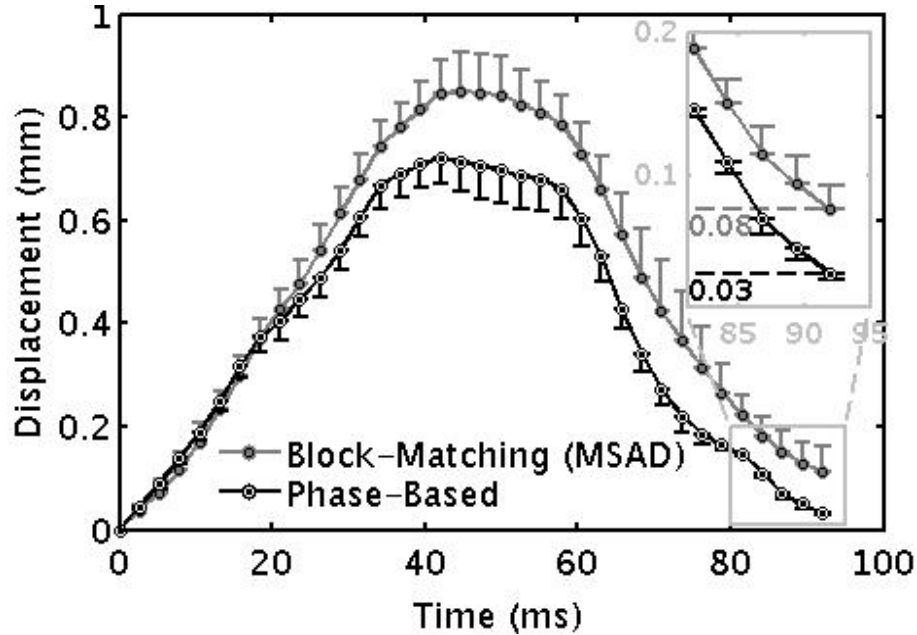


Figure 7.7: Displacement magnitude of mouse left ventricular wall at the mid-papillary level shown through a complete heart cycle. Phase-based tracking show lower tracking error as shown by lower displacement at the end of the cardiac cycle (inset, upper right), where the final displacement should be zero.

Phase-based tracking technique also has the potential to track direction of blood flow in the LV cavity. Figure 8 shows the trajectories in a mouse left ventricle from end-diastole to end-systole in long-axis view. Orientation of blood motion in the LV cavity near the late stage of systole is accurately depicted with phase-based tracking.

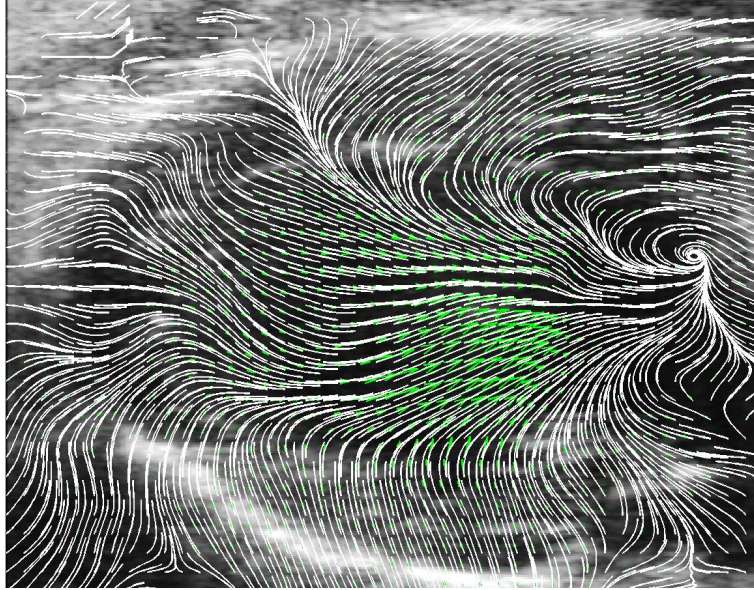


Figure 7.8: Displacement of mouse left ventricle in long-axis view from end-diastole to end-systole. Green arrows on the cavity show orientation of blood flow during late systole.

#### 7.4 DISCUSSION

We have presented a method for tracking myocardial motion using phase information via the monogenic signal. Similar results were presented for simulated data using both block-matching and phase-based tracking methods. However, computation time for phase-based tracking is at least twice as fast as block-matching, where for 1cm x 1cm region of interest tracked over 50 frames took approximately 42 seconds to compute in MATLAB (on a 2.66 GHz Intel Core i7 processor) for the phase-based approach, the computation time for block-matching was over 90 seconds. Similarly, for *in vivo* mouse heart data, computation time for

a single heart cycle consisting of 46 frames was 18 and 40 seconds for phased-based and block-matching, respectively. Tracking error for phase-based tracking is also significant lower than MSAD block-matching techniques. Post-processing of tracked displacement data when using block-matching, such as spatial average or temporal smoothing, is often applied to smooth displacement data. In phased-based tracking, spatial smoothing is built into SQF. Further investigation in SQF design can shorten computation time by removing post-processing of tracked displacement. Phase-based displacement estimation is an improved alternative to classical block-matching techniques as it utilizes important image information. As shown using phantom and *in vivo* data sets, phase-based motion tracking using the monogenic signal is accurate and computationally inexpensive.

## Chapter 8: Conclusions

In this dissertation, several methods for quantifying ischemic myocardium functions in mice using high frequency ultrasound were examined. Quantitative assessment of regional cardiac function serves as a valuable tool for diagnosis of heart disease. Heart disease remains the leading cause of death worldwide, with myocardial infarction being the major contributing factor to the high morbidity and mortality rates, and echocardiography remains a vital role in the evaluation of patients with suspected heart disease.

### ***8.1.1 Kinematic Models of Left Ventricle Using Near Incompressibility***

An approach for reconstructing 3D motion, throughout the mouse LV, that combines orthogonal stacks of 2D imaging planes to arrive at a finely sampled 3D displacement mapping through the entire heart cycle is presented. A unique kinematic model of the mouse LV has been shown to accurately predict the motion of the myocardium by enforcing near myocardial incompressibility and using reconstructed 3D motion. Compared to a standard cylindrical model, my model allows sufficient spatial variation in radial motion to model diseased hearts. In summary, a kinematic model is developed by incorporating prior information about left ventricular deformation, and assuming only that displacements in the left ventricle are polynomial functions of initial position and that the myocardium is

nearly incompressible, while allowing myocardial motion to vary spatially as would be expected in an ischemic or dyssynchronous left ventricle.

### ***8.1.2 Improved Cardiac Function in iNOS KO Mice***

Numerous studies have reported that lack of NO, through iNOS gene knockout, is beneficial to heart function after ischemia in mice (Guo, 1999; Sam, 2001; Feng, 2001; Li, 2003; Luo, 2005). In contrast at least one study has reported that iNOS KO mice do not exhibit improved cardiac function after MI, and that survivability, infarct size, and systolic function were not significantly different from wild type (WT) mice after 1 month (Jones, 2005). My work has shown that mice lacking iNOS exhibit both attenuated left ventricular remodeling and circumferential extent of wall thinning late after MI. Using the metrics developed in Chapter 4, LV remodeling and dyssynchrony are quantified to test the hypothesis that the attenuation in LV remodeling in iNOS KO mice would be accompanied by an attenuation in LV dyssynchrony.

Chapter 4 has demonstrated that iNOS KO mice have reduced LV remodeling and dyssynchrony, thus improved cardiac function, late after MI. However, this work does not show that iNOS plays an important role in LV remodeling and function; rather, it is the lack of iNOS that has beneficial effect to cardiac function after ischemia.

### **8.1.3 Ultrasound-Mediated Molecular Imaging Using Targeted Microbubbles**

The ability for ultrasound to detect recent ischemic myocardium is demonstrated in Chapter 5. The use of contrast agents as molecular biomarkers not only helps to further understand the biological processes during inflammation, but also has the potential for early detection of cardiovascular diseases. In Chapter 5, modified microbubbles as targeted contrast agents with single and dual targets enables molecular imaging using ultrasound. I studied a dual targeted microbubble motif to increase binding efficiency of microbubbles to its targets. Furthermore, a constant infusion method is employed to mitigate bubble-induced acoustic shadowing by gradually introducing microbubbles into the circulatory system. Early detection of myocardial ischemia using ultrasound contrast agents would be a powerful clinical tool, especially for patients with ambiguous symptom of coronary heart diseases.

## References:

1. J. E. Adkins, "Some general results in the theory of large elastic deformation," *Proc. R. Soc.* 231, 75-90, 1955.
2. M. K. Aliev, P. D. Santos, J. A. Hoerter, S. Soboll, A. N. Tikhonov, V. A. Saks, "Water content and its intracellular distribution in intact and saline perfused rat hearts revisited," *Cardio. Res.* 53, 48-58, 2002.
3. R. L. Armentano, J. G. Barra, J. Levenson, A. Simon, and R. H. Pichel, "Arterial wall mechanics in conscious dogs: Assessments of viscous, inertial, and elastic moduli to characterize aortic wall behavior," *Circulation Research*, 73, 468–378, 1995.
4. R. Armentano, J. L. Megnien, A. Simon, F. Bellenfant, J. Barra, and J. Levenson, "Effects of hypertension on viscoelasticity of carotid and femoral arteries in humans," *Hypertension*, 26, 48–54, 1995.
5. R.D. Bauer, R. Busse, A. Schabert, Y. Summa, and E. Wetterer. "Separate determination of the pulsatile elastic and viscous forces developed in the arterial wall in vivo," *European Journal of Physiology*, 380, 221–226, 1979.
6. M. E. Beauharnois, K. C. Lindquist, D. Marathe, P. Vanderslice, J. Xia, K. L. Matta, S. Neelamegham, "Affinity and kinetics of sialyl Lewis-X and core-2 based oligosaccharides binding to L- and P-selectin," *Biochemistry*, 44, 9507–9519, 2005.

7. K. C. Bilchick, V. Dimaano, K. C. Wu, R. H. Helm, R. G. Weiss, J. A. Lima, R. D. Berger, G. F. Tomaselli, D. A. Bluemke, H. R. Halperin, T. Abraham, D. A. Kass, A. C. Lardo, "Cardiac magnetic resonance assessment of dyssynchrony and myocardial scar predicts function class improvement following cardiac resynchronization therapy," *JACC Cardiovasc Imaging*, 1, 561 – 568, 2008.
8. J. Bistoquet, J. Oshinski, O. Skrinjar, "Myocardial deformation recovery from cine MRI using a nearly incompressible biventricular model," *Med. Image Analysis*, 12, 69-85, 2008.
9. J. Blacher, B. Pannier, A. P. Guerin, S. J. Marchais, M. E. Safar, and G. M. London, "Carotid arterial stiffness as a predictor of cardiovascular and all-cause mortality in end-stage renal disease," *Hypertension*, 32, 570–574, 1998.
10. M. L. Bots, D. Baldassarre, A. Simon, E. de Groot, D. H. O’Leary, W. Riley, J. J. Kastelein, and D. E. Grobbee, "Carotid intima-media thickness and coronary atherosclerosis: weak or strong relations?" *European heart journal*, 28, 398–406, 2007.
11. L. P. Budge, A. S. Helms, M. Salerno, C. M. Kramer, F. H. Epstein, K.C. Bilchick, "MR cine DENSE dyssynchrony parameters for the evaluation of heart failure: comparison with myocardial tissue tagging," *JACC Cardiovasc Imaging*, 5, 789-97, 2008.

12. P. Carmeliet, R. K. Jain, "Angiogenesis in cancer and other diseases," *Nature*, 407, 249-257, 2000.
13. X. Chen, H. Xie, R. Erkamp, K. Kim, C. Jia, J. Rubin, M. O'Donnell, "3-D correlation-based speckle tracking," *Ultrasonic Imaging*, 27, 21-36, 2005.
14. G. Y. Cho, J. K. Song, W. J. Park, S. W. Han, S. H. Choi, Y. C. Doo, D. J. Oh, Y. Lee, "Mechanical dyssynchrony assessed by tissue Doppler imaging is a powerful predictor of mortality in congestive heart failure with normal QRS duration," *J Am Coll Cardiol*, 46, 2237–2243, 2005.
15. M. Cinthio, A. R. Ahlgren, J. Bergkvist, T. Jansson, H. W. Persson, and K. Lindström, "Longitudinal movements and resulting shear strain of the arterial wall," *American journal of physiology. Heart and circulatory physiology*, 291, H394–402, 2006.
16. K. D. Costa, P. J. Hunter, J. M. Rogers, J. M. Guccione, L. K. Waldman, A. D. McCulloch, "A three-dimensional finite element method for large elastic deformations of ventricular myocardium: I – cylindrical and spherical polar coordinates," *J. Biomech. Eng.* 118, 452-463, 1996.
17. J. Crosby, B. Amundsen, T. Hergum, E. Remme, S. Langeland, H. Torp, "3-D speckle tracking for assessment of regional left ventricular function," *Ultrasound in Medicine and Biology*, 35, 458-471, 2009.
18. A. M. Dart and B. A. Kingwell, "Pulse pressure—a review of mechanisms and clinical relevance," *Journal of the American College of Cardiology*, 37, 975–984, 2001.

19. B. P. Davidson, B. A. Kaufmann, T. Belcik, A. Xie, Y. Qi, J R. Lindner, "Detection of antecedent myocardial ischemia with multiselectin molecular imaging," *JACC*, 60, 1690-1697, 2012.
20. J. S. de Jong, P. J. van Diest, P. van der Valk, J. P. Baak, "Expression of growth factors, growth-inhibiting factors, and their receptors in invasive breast cancer. II: Correlations with proliferation and angiogenesis," *J Pathol*, 184, 53-57, 1998.
21. V. Delgado, C. Ypenburg, R. J. van Bommel, L. F. Tops, S. A. Mollema, N. A. Marsan, G. B. Bleeker, M. J. Schalij, J. J. Bax, "Assessment of left ventricular dyssynchrony by speckle tracking strain imaging: Comparison between longitudinal, circumferential, and radial strain in cardiac resynchronization therapy," *J Am Coll Cardiol*, 51,1944–1952, 2008.
22. J. D'hooge, D. Thijs, K. Sipido, P. Claus, B. Bijnens, J. Thoen, F. Van de Werf, G. R. Sutherland, P. Suetens, "Ultrasonic strain and strain rate imaging for the assessment of regional myocardial function in mice," *IEEE Ultrasonics Symp Proc*, 470-473, 2004.
23. J. M. Dijk, A. Algra, Y. van der Graaf, D. E. Grobbee, and M. L. Bots, "Carotid stiffness and the risk of new vascular events in patients with manifest cardiovascular disease. the SMART study," *European heart journal*, 26, 1213–1220, 2005.

24. A. Elen, H. Choi, D. Loeckx, H. Gao, P. Claus, P. Suetens, F. Maes, J. D'hooge, "Three-dimensional cardiac strain estimation using spatio-temporal elastic registration of ultrasound images: a feasibility study," *Transaction on Medical Imaging*, 27, 1580-1591, 2008.
25. M. Felsberg, G. Sommer, "The Monogenic Signal," *IEEE Trans. Signal Process*, 49, 3136-3144, 2001.
26. M. Felsberg, "Optical Flow Estimation From Monogenic Phase," *First International Workshop, IWCM*, 2004.
27. Q. Feng, X. Lu, D. L. Jones, J. Shen, J. M. Arnold. "Increased inducible nitric oxide synthase expression contributes to myocardial dysfunction and higher mortality after myocardial infarction in mice," *Circulation*, 104, 700-704, 2001.
28. E. A. Ferrante, J. E. Pickard, J. J. Rychak, A. L. Klibanov, K. Ley, "Dual targeting improves microbubble contrast agent adhesion to VCAM-1 and P-selectin under flow," *Journal of Controlled Release*, 100-107, 2009.
29. P. J. A. Frinking, I. Tardy, M. Théraulaz, M. Arditi, J. Powers, S. Pochon, F. Tranquart, "Effects of Acoustic Radiation Force on the Binding Efficiency of BR55, a VEGFR2-Specific Ultrasound Contrast Agent," *Ultrasound in Medicine & Biology*, 38, 1460–1469, 2012.
30. F. S. Foster, M. Y. Zhang, Y. Q. Zhou, G. Liu, J. Mehi, E. Cherin, K. A. Harasiewicz, B. G. Starkoski, L. Zan, D. A. Knapik, S. L. Adamson. "A new ultrasound instrument for in vivo microimaging of mice," *Ultrasound Med Biol*, 28,1165–1172, 2002.

31. F. S. Foster, J. Mehi, M. Lukacs, D. Hirson, C. White, C. Chaggares, A. Needles. "A new 15-50 MHz array-based micro-ultrasound scanner for preclinical imaging," *Ultrasound Med Biol*, 35,1700-1708, 2009.
32. C. D. Garson, B. Li, J. A. Hossack, "The application of the principle of conserved myocardium volume in guiding automated chamber estimation in mouse cardiac imaging," *SPIE International symposium of Medical Imaging*, 6513, 2007.
33. C. Garson, Y. Li, J. Hossack, "3D cardiac motion estimation using RF signal decorrelation," *Ultrasonics Symposium*, 471-474, 2008.
34. C. D. Garson, B. Li, S. T. Acton, J. A. Hossack, "Guiding automated left ventricular chamber segmentation in cardiac imaging using the concept of conserved myocardial volume," *Comp. Med. Imag. Graph*, 32, 321-330, 2008.
35. R. C. Gessner, J. E. Streeter, R. Kothadia, S. Feingold, P. A. Dayton, "An In Vivo Validation of the Application of Acoustic Radiation Force to Enhance the Diagnostic Utility of Molecular Imaging Using 3-D Ultrasound," *Ultrasound in Medicine & Biology*, 38, 651–660, 2012.
36. R. J. Gibbons, D. W. Jones, T. J. Gardner, L. B. Goldstein, J. H. Moller, and C. W. Yancy, "The american heart association's 2008 statement of principles for healthcare reform," *Circulation*, 118, 2209–2218, 2008.

37. W. D. Gilson, F. H. Epstein, Z. Yang, Y. Xu, K. R. Prasad, M. Toufektsian, V. E. Laubach, B. A. French. "Borderzone contractile dysfunction is transiently attenuated and left ventricular structural remodeling is markedly reduced following reperfused myocardial infarction in inducible nitric oxide synthase knockout mice," *JACC*. 50, 1799-1807, 2007.
38. J. Gorcsan III, "Echocardiographic strain imaging for myocardial viability: an improvement over visual assessment?" *Circulation*, 112, 3820-3822, 2005.
39. J. M. Guccione, A. D. McCulloch, L. K. Waldman, "Passive Material Properties of Intact Ventricular Myocardium Determined From a Cylindrical Model," *J. Biomech. Eng.* 113, 42-55, 1991.
40. Y. Guo, W. K. Jones, Y. Xuan, X. Tang, W. Bao, W. Wu, V.E. Laubach, P. Ping, Z. Yang, Y. Qiu, R. Bolli. "The late phase of ischemic preconditioning is abrogated by targeted disruption of the inducible NO synthase gene," *PNAS*, 96, 11507-11512, 1999.
41. D. Hanahan, G. Bergers, E. Bergsland, "Less is more, regularly: metronomic dosing of cytotoxic drugs can target tumor angiogenesis in mice," *J Clin Invest*, 105, 1045-1047 2000.
42. V. Harding, L. Jones, R. Lefkowitz, W. Koch, H. Rockman, "Cardiac beta ARK1 inhibition prolongs survival and augments beta blocker therapy in a mouse model of severe heart failure," *Proceeding of the National Academy of Sciences*, 98, 5809-14, 2001.

43. S. L. Herz, C. M. Ingrassia, S. Homma, K. D. Costa, J. W. Holmes, "Parameterization of left ventricular wall motion for detection of regional ischemia," *Ann. Biomed. Eng.* 33, 912–919, 2005.
44. S. L. Herz, T. Hasegawa, A. N. Makaryus, K. M. Parker, S. Homma, J. Wang, J. W. Holmes, "Quantitative three-dimensional wall motion analysis predicts ischemic region size and location," *Ann Biomed Eng.* 38, 1367-1376, 2010.
45. G. Howard, A. R. Sharrett, G. Heiss, G. W. Evans, L. E. Chambless, W. A. Riley, and G. L. Burke, "Carotid artery intimal-medial thickness distribution in general populations as evaluated by b-mode ultrasound," *Stroke*, 24, 1297–1304, 1993.
46. J. D. Humphrey, F. C. Yin, "Constitutive relations and finite deformations of passive cardiac tissue II: stress analysis in the left ventricle. *Cir. Res.* 65, 805-817, 1989.
47. J. D. Humphrey, J. F. Eberth, W. W. Dye, and R. L. Gleason, "Fundamental role of axial stress in compensatory adaptations by arteries," *Journal of biomechanics*, 42, 1–8, 2009.
48. C. M. Ingrassia, T. P. Usyk, R. C.P. Kerckhoffs, A. D. McCulloch, K. D. Costa, J. W. Holmes, "Model-based development of four-dimensional wall motion measures," *Comput. Methods Appl. Mech. Engrg.* 196, 3061–3069, 2007.
49. Institute for Health Metrics and Evaluation. "Global Burden of Disease," Available online: <http://www.healthmetricsandevaluation.org/tools/data-visualizations>, 2013.

50. S. P. Jones, J. J. M. Greer, P. D. Ware, J. Yang, K. Walsh, D. J. Lefer. "Deficiency of iNOS does not attenuate severe congestive heart failure in mice," *APJHeart*. 288, H265-H370, 2005.
51. R. M. Judd, B. I, Levy, "Effects of Barium-induced Cardiac Contraction on Large- and Small-Vessel Intramyocardial Blood Volume," *Circulation*. 68, 217-225, 1991.
52. M. Juonala, M. Khnen, T. Laitinen, N. Hutri-Khnen, E. Jokinen, L. Tait-tonen, M. Pietikinen, H. Helenius, J. S. A. Viikari, and O. T. Raitakari, "Effect of age and sex on carotid intima-media thickness, elasticity and brachial endothelial function in healthy adults: the cardiovascular risk in young finns study," *European heart journal*, 29, 1198– 1206, 2008.
53. B. A. Kaufmann, C. Lewis, A. Xie, A. Mirza-Mohd, J. R. Lindner. "Detection of recent myocardial ischaemia by molecular imaging of P-selectin with targeted contrast," *echocardiography. Eur Heart J*, 28, 2011–2017, 2007.
54. C. Klein, T. R. Schmal, S. G. Nekolla, B. Schnackenburg, E. Fleck, E. Nagel, "Mechanism of late gadolinium enhancement in patients with acute myocardial infarction," *J. of Cardiovascular Mag, Res.*, 9, 653-658, 2007.
55. A. L. Klibanov, "Ligand-carrying gas-filled microbubbles: ultrasound contrast agents for targeted molecular imaging," *Bioconjug Chem*, 16, 9-17, 2005.

56. L. Klibanov, J. J. Rychak, W. C. Yang, S. Alikhani, B. Li, S. Acton, J. R. Lindner, K. Ley, S. Kaul, "Targeted ultrasound contrast agent for molecular imaging of inflammation in high-shear flow," *Contrast Media Mol Imaging*. 1, 259-266, 2006.
57. C. Leavens, R. Williams, F. S. Foster, P. N. Burns, M. D. Sherar, "Golay Pulse Encoding for Microbubble Contrast Imaging in Ultrasound," *IEEE Trans. UFFC*, 54, 2082-2090, 2007.
58. W. Lee, E. Konofagou, "Angle-independent and multi-dimensional myocardial elastography from theory to clinical validation," *Ultrasonics*, 48, 563-567, 2008.
59. Q. Li, Y. Guo, Y. Xuan, C. J. Lowenstein, S. C. Stevenson, S. D. Prabhu, W. Wu, Y. Zhu, R. Bolli, "Gene therapy with inducible nitric oxide synthase protects against myocardial infarction via cyclooxygenase-2-dependent mechanism," *Circulation*, 92, 741-748, 2003.
60. Y. Li, C. D. Garson, Y. Xu, R. J. Breyers, F. H. Epstein, B. A. French, J. A. Hossack, "Quantification and MRI validation of regional contractile dysfunction in mice post myocardial infarction using high resolution ultrasound," *Ultrasound in Medicine and Biology*, 33, 894-904. 2007.
61. Y. Li, C. D. Garson, Y. Xu, B. A. French, J. A. Hossack, "High frequency ultrasound imaging detects cardiac dyssynchrony in noninfarcted regions of the murine left ventricle late after reperfused myocardial infarction," *Ultrasound in Medicine and Biology*, 34, 1062-1075, 2008.

62. Y. Li, C. D. Garson, Y. Xu, P. A. Helm, J. A. Hossack, B. A. French, "Serial ultrasound evaluation of intramyocardial strain after reperfused myocardial infarction reveals that remote zone dyssynchrony develops in concert with left ventricular remodeling," *Ultrasound in Medicine and Biology*, 37, 1073-1086, 2011.
63. Y. Li, P. Helm, C. Garson, Y. Xu, B. French, J. Hossack, "A four-dimensional Model-based method for assessing cardiac contractile dyssynchrony in mice," *Ultrasonics Symposium*, 1753-6, 2008.
64. D. Lin, J. Holmes, J. Hossack, "An ultrasound-driven kinematic model of the heart that enforces local incompressibility," *Functional Imaging and Modeling of the Heart*, 129-136, 2011.
65. J. R. Lindner, K. Wei, S. Kaul, "Imaging of myocardial perfusion with sonovue in patients with a prior myocardial infarction," *Echocardiography*, 16, 753-760, 1999.
66. J. R. Lindner, M. Coggins, S. Kaul, A. Klibanov, G. Brandenburger, K. Ley, "Microbubble persistence in the microcirculation during ischemia/ reperfusion and inflammation is caused by integrin and compliment mediated adherence to activated leukocytes," *Circulation*, 101, 668 –75, 2000.
67. J. R. Lindner, J. Song, J. Christiansen, A. L. Klibanov, F. Xu, K. Ley, "Ultrasound assessment of inflammation and renal tissue injury with microbubbles targeted to P-selectin," *Circulation*, 104, 2107–2112, 2001.

68. J. Liu, J. Du, C. Zhang C, J. W. Walker, X. Huang. "Progressive troponin I loss impairs cardiac relaxation and causes heart failure in mice," *Am J Physiol Heart Circ Physiol*, 293, H1273–H1281, 2007.
69. Y. Liu, O. A. Carretero, O. H. Cingolani, T. Liao, Y. Sun, J. Xu, L. Y. Li, P. J. Pagano, J. J. Yang, X. Yang. "Role of inducible nitric oxide synthase in cardiac function and remodeling in mice with heart failure due to myocardial infarction," *APJHeart*, 289, H2616-H2623, 2005.
70. A. F.H. Lum, M. A. Borden, P. A. Dayton, D. E. Kruse, S. I. Simon, K. W. Ferrara, "Ultrasound radiation force enables targeted deposition of model drug carriers loaded on microbubbles," *Journal of Controlled Release*, 111, 128–134, 2006.
71. A. M. Malek, S. L. Alper, and S. Izumo, "Hemodynamic shear stress and its role in atherosclerosis," *JAMA: the journal of the American Medical Association*, 282, 2035–2042, 1999.
72. E. Mannucci, L. Lambertucci, M. Monami, A. Fedeli, V. Chiasserini, N. Marchionni, G. Masotti, and A. Ungar, "Pulse pressure and mortality in hypertensive type 2 diabetic patients. a cohort study," *Diabetes/metabolism research and reviews*, 22, 172–175, 2006.
73. T. Mansi, X. Pennec, M. Sermesant, "iLogDemons: A demons-based registration algorithm for tracking incompressible elastic biological tissues," *Int. J. Comput. Vis*, 92, 92-111, 2010.

74. P. B. Massion, O. Feron, C. Dessy, J. L. Balligand. "Nitric oxide and cardiac function, ten years after and continuing," *Circulation*. 93, 388-398, 2003.
75. F. U. S. Mattace-Raso, T. J. M. van der Cammen, A. Hofman, N. M. van Popele, M. L. Bos, M. A.D.H. Schalekamp, R. Asmar, R. S. Reneman, A. P.G. Hoeks, M. M.B. Breteler, J. C.M. Witteman, "Arterial Stiffness and Risk of Coronary Heart Disease and Stroke: The Rotterdam Study," *Circulation*, 113, 657-663, 2006.
76. F. Mauldin, D. Lin, J. Hossack, "The singular value filter: a general filter design strategy for PCA-based signal separation in medical ultrasound imaging," *Transaction on Medical Imaging*, 2011.
77. C. M. McEniery, S. Wallace, I. S. Mackenzie, B. McDonnell, Yasmin, D. E. Newby, J. R. Cockcroft, and I. B. Wilkinson, "Endothelial function is associated with pulse pressure, pulse wave velocity, and augmentation index in healthy humans," *Hypertension*, 48, 602–608, 2006.
78. F. Mechler, D. S. Reich, J. D. Victor, "Detection and discrimination of relative spatial phase by V1 neurons," *Journal of Neuroscience*, 22, 6129–6157, 2002.
79. L. Michael, M. Entman, C. Hartley, et al., "Myocardial ischemia and reperfusion: A murine model," *Am J Physiol Heart Circ Physiol*, 269, H2147–H2154, 1995.

80. R. Q. Migrino, X. Zhu, M. Morner, T. Brahmabhatt, M. Bright, M. Zhao, "Myocardial dysfunction in the periinfarct and remote regions following anterior infarction in rats quantified by 2D radial strain echocardiography: An observational cohort study," *Cardiovascular Ultrasound*, 6, 2008.
81. V. Mihalef, R. Ionasec, Y. Wang, Y. Zheng, B. Georgescu, D. Comaniciu, "Patient-specific modeling of left heart anatomy, dynamics and hemodynamics from high resolution 4D CT," *IEEE ISBI*, 504 – 507, 2010.
82. T. D. Miller, T. F. Christian, M. R. Hopfenspirger, D. O. Hodge, B. J. Gersh, R. J. Gibbons, "Infarct size after acute myocardial infarction measured by quantitative tomographic <sup>99m</sup>Tc sestamibi imaging predicts subsequent mortality," *Circulation*, 92, 334-341, 1995.
83. S. A. Mollema, G. B. Bleeker, S. S. Liem, E. Boersma, B. L. van der Hoeven, E. R. Holman, E. E. van der Wall, M. J. Schalij, J. J. Bax, "Does left ventricular dyssynchrony immediately after acute myocardial infarction result in left ventricular dilatation?" *Heart Rhythm Society*, 1145-1148, 2007.
84. M. Nahrendorf, K. Hiller, K. Hu, G. Ertl, A. Haase, and W. Bauer, "Cardiac magnetic resonance imaging in small animal models of human heart failure," *Medical Image Analysis*, 7, 369-375, 2003.
85. S. Niederer, K. Rhode, K. Razavi, N. Smith, "The importance of model parameters and boundary conditions in whole organ models of cardiac contraction," *FIMH*, 5528, 348 – 356, 2009.

86. H. Nesser, V. Avi, W. Gorissen, L. Weinert, R. Mascherbauer, J. Niel, L. Sugeng, R. Lang, "Quantification of left ventricular volumes using three-dimensional echocardiographic speckle tracking: comparison with MRI," *European Heart Journal*, 30, 1565-1573. 2009.
87. W. W. Nichols and M. F. O'Rourke, "McDonald's Blood Flow in Arteries: Theoretical, Experimental and Clinical Principles," Hodder Arnold, 2005.
88. D. H. O'Leary, J. F. Polak, R. A. Kronmal, T. A. Manolio, G. L. Burke, and J. Wolfson, S K, "Carotid-artery intima and media thickness as a risk factor for myocardial infarction and stroke in older adults. cardiovascular health study collaborative research group," *The New England journal of medicine*, 340, 14-22, 1999.
89. M. O'Donnell, A. R. Skovoroda, B. M. Shapo, S. Y. Emelianov, "Internal Displacement and Strain Imaging Using Ultrasonic Speckle Tracking," *IEEE Transactions on Ultrasonics Ferroelectrics & Frequency Control*, 41, 314-325, 1994.
90. P. Pacher, J. S. Bechman, L. Liaudet, "Nitric Oxide and peroxynitrite in health and disease," *Physiology Review*, 87, 315-424, 2007.
91. M. V. Pitzalis, M. Iacoviello, R. Romito, P. Guida, E. De Tommasi, G. Luzzi, M. Anaclerio, C. Forleo, P. Rizzon, "Ventricular asynchrony predicts a better outcome in patients with chronic heart failure receiving cardiac resynchronization therapy," *J Am Coll Cardiol*, 45, 70-1, 2005.

92. J. H. Pope, T. P. Aufderheide, R. Ruthazer, R. H. Woolard, J. A. Feldman, J. R. Beshansky, J. L. Griffith, H. P. Selker, "Missed diagnosis of acute cardiac ischemia in the emergency department," *New England Journal of Medicine*, 342, 1163-1170, 2000.
93. M. C. Porciani, F. Cappelli, L. Perrotta, M. Chiostrì, C. M. Rao, P. Pieragnoli, G. Ricciardi, A. Michelucci, S. Jelic, L. Padeletti. "Has mechanical dyssynchrony still a role in predicting cardiac resynchronization therapy response," *Echocardiography*, 27, 831–838, 2010.
94. V. L. Roger, A. S. Go, D. M. Lloyd-Jones, R. J. Adams, J. D. Berry, T. M. Brown, M. R. Carnethon, S. Dai, G. de Simone, E. S. Ford, C. S. Fox, H. J. Fullerton, C. Gillespie, K. J. Greenlund, S. M. Hailpern, J. A. Heit, P. M. Ho, V. J. Howard, B. M. Kissela, S. J. Kittner, D. T. Lackland, J. H. Lichtman, L. D. Lisabeth, D. M. Makuc, G. M. Marcus, A. Marelli, D. B. Matchar, M. M. McDermott, J. B. Meigs, C. S. Moy, D. Mozaffarian, M. E. Mussolino, G. Nichol, N. P. Paynter, W. D. Rosamond, P. D. Sorlie, R. S. Sotnick, T. N. Turan, M. B. Turner, N. D. Wong, J. Wylie-Rosett, "Heart disease and stroke statistics 2013 Update: A report from the American Heart Association," *Circulation*, 123, e18 - e209, 2013.
95. J. J. Rychak, J. R. Lindner, K. Ley, A. L. Klivanov, "Deformable gas-filled microbubbles targeted to P-selectin," *Journal of Controlled Release*, 11, 288-299, 2006.

96. F. Sam, D. B. Sawyer, Z. Xie, D. L. F. Chang, S. Ngoy, D. A. Brenner, D. A. Siwik, K. Singh, C. S. Apstein, W. S. Colucci. "Mice lacking inducible nitric oxide synthase have improved left ventricular contractile function and reduced apoptotic cell death late after myocardial infarction," *Circulation*, 89, 351-356, 2001.
97. T. Schlosser, C. Phol, S. Kuntz-Hehner, H. Omran, H. Becher, K. Tiemann, "Echoscintigraphy: a new imaging modality for the reduction of color blooming and acoustic shadowing in contrast sonography," *Ultrasound Med Biol.*, 29, 985-991, 2003.
98. M. Y. Shen, Y. H. Liu, A. J. Sinusas, R. Fetterman, W. Bruni, O. E. Drozhinin, B. L. Zaret, F. J. Wackers, "Quantification of regional myocardial wall thickening on electrocardiogram-gated spect imaging," *J Nucl Cardiol*, 6, 583-595, 1999.
99. E. Sho, H. Nanjo, M. Sho, M. Kobayashi, M. Komatsu, K. Kawamura, C. Xu, C. K. Zarins, and H. Masuda, "Arterial enlargement, tortuosity, and intimal thickening in response to sequential exposure to high and low wall shear stress," *Journal of vascular surgery*, 39, 601–612, 2004.
100. J. M. Spencer, "Continuum mechanics," Longman Press, London, 1980.
101. S. Stork, A. W. van den Beld, C. von Schacky, C. E. Angermann, S. W. J. Lamberts, D. E. Grobbee, and M. L. Bots, "Carotid artery plaque burden, stiffness, and mortality risk in elderly men: a prospective, population-based cohort study," *Circulation*, 110, 344–348, 2004.

102. M. S. Suffoletto, K. Dohi, M. Cannesson, S. Saba, J. Gorcsan III, "Novel speckle-tracking radial strain from routine black-and-white echocardiographic images to quantify dyssynchrony and predict response to cardiac resynchronization therapy," *Circulation*, 117, 960-968, 2006.
103. G. R. Sutherland, M. J. Stewart, K. W. Groundstroem, C. M . Moran, A. D. Fleming, F. J. Guell-Peris, R. A. Riemersma, L. N. Fenn, K. A. Fox, W. N. McDicken, "Color Doppler myocardial imaging: a new technique for the assessment of myocardial function," *J Am Soc Echocardiogr*, 7, 441-458, 1994.
104. M. G. Sutton, N. Sharpe, "Left ventricular remodeling after myocardial infarction: pathophysiology and therapy," *Circulation*, 101, 2981-8, 2000.
105. M. Takalkar, A. L. Klibanov, J. J. Rychak, J. R. Lindner, K. Ley, "Binding and detachment dynamics of microbubbles targeted to P-selectin under controlled shear flow," *J Control Release*, 96, 473–482, 2004.
106. M. Tanguy, D. Philippe, B. Adrian, "Motion estimation using the monogenic signal applied to ultrasound elastography," *IEEE EMB*, 33-36, 2010.
107. C. A. Taylor, C.A. Figueroa, "Patient-specific modeling of cardiovascular mechanics," *Annu. Rev. BioMed. Eng.*, 11, 109-134, 2009.
108. T. Tamatani, M. Suematsu, K. Tezuka, N. Hanzawa, T. Tsuji, Y. Ishimura, R. Kannagi, S. Toyoshima, M. Homma, "Recognition of consensus CHO structure in ligands for selectins by novel antibody against sialyl Lewis X," *Am. J. Physiol.* 269, H1282–H1287, 1995.

109. F. S. Villanueva, A. Klibanov, W. R. Wagner, "Microbubble-endothelial cell interactions as a basis for assessing endothelial function," *Echocardiography*, 19, 427-438, 2002.
110. F. S. Villanueva, E. Lu, S. Bowry, S. Kilic, E. Tom, J. Wang, J. Gretton, J. J. Pacella, W. R. Wagner, "Myocardial ischemic memory imaging with molecular echocardiography," *Circulation*. 115, 345-52. 2007.
111. K. C. Vinnakota, J. B. Bassingthwaighte, "Myocardial density and composition: A basis for calculating intracellular metabolite concentrations," *Am. J. Physiol. Heart Circ. Physiol.*, 286, H1742 – H1749, 2004.
112. W. F. Walker, G. E. Trahey, "A fundamental limit on the performance of correlation based phase correction and flow estimation techniques," *IEEE Trans. Ultrasonics, Ferroelectrics and Frequency Control*, 41, 644-654, 1994.
113. Y. Wang, B. Georgescu, H. Houle, D Comaniciu, "Volumetric myocardial mechanics from 3D+t ultrasound data with multi-model tracking," *STACOM-CESC, LNCS 6364*, 184-193, 2010.
114. J. M. Warram, A. G. Sorace, R. Saini, H. R. Umphrey, K. R. Zinn, K. Hoyt, "A triple-targeted ultrasound contrast agent provides improved localization to tumor vasculature," *J Ultrasound Med*, 30, 921-931, 2011.
115. G. E. Weller, E. Lu, M. M. Csikari, A. L. Klibanov, D. Fischer, W. R. Wagner, F. S. Villanueva, "Ultrasound imaging of acute cardiac transplant rejection with microbubbles targeted to intercellular adhesion molecule-1," *Circulation*, 108, 218-224, 2003.

116. G. E. Weller, M. K. Wong, R. A. Modzelewski, E. Lu, A. L. Klibanov, W. R. Wagner, F. S. Villanueva, "Ultrasonic imaging of tumor angiogenesis using contrast microbubbles targeted via the tumor-binding peptide arginine-arginine-leucine," *Cancer Res.* 65, 533-549, 2005.
117. G. E.R. Weller, F. S. Villanueva, E. M. Tom, W. R. Wagner, "Targeted ultrasound contrast agents: In vitro assessment of endothelial dysfunction and multi-targeting to ICAM-1 and sialyl Lewis<sup>x</sup>," *Biotechnology and Bioengineering*, 92, 780–788, 2005.
118. J. K. Willmann, R. H. Kimura, N. Deshpande, A. M. Lutz, J. R. Cochran, S. S. Gambhir, "Targeted contrast-enhanced ultrasound imaging of tumor angiogenesis with contrast microbubbles conjugated to integrin-binding knottin peptides," *Journal of Nuclear Med*, 51, 433-440, 2010.
119. Y. Xiaomei, M. Murase, "A Multi-scale phase-based optical flow method for motion tracking of left ventricle," *iCBBE*, 2010.
120. J. Xu, C. Zhang, A. Khanna, "Wideband high-frequency echocardiography to evaluate myocardial infarct size," *American Institute of Ultrasound Medicine*, 1527-1534.
121. S. Zhao, M. Borden, S. H. Bloch, D. Kruse, K. W. Ferrara, P. A. Dayton, "Radiation-Force Assisted Targeting Facilitates Ultrasonic Molecular Imaging," *Mol Imaging*, 3, 135–148, 2004.

122. Y. Q. Zhou, F. S. Foster, B. J. Nieman, L. Davidson, X. J. Chen, R. M. Henkelman, "Comprehensive transthoracic cardiac imaging in mice using ultra- sound biomicroscopy with anatomical confirmation by magnetic resonance imaging," *Physiol Genomics*, 18, 232–244, 2004.
123. Y. Q. Zhou, F. S. Foster, R. Parkes, S. L. Adamson, "Developmental changes in left and right ventricular diastolic filling patterns in mice," *Am J Physiol Heart Circ Physiol*, 285, H1563–1575, 2003.
124. Y. Zhu, X. Papademetris, A. J. Sinusas, J. S. Duncan, "A coupled deformable model for tracking myocardial borders from real-time echocardiography using an incompressibility constraint," *Med. Image Analysis*, 14, 429-448, 2010.
125. M. Zamir, *The Physics of Pulsatile Flow*. Springer, Feb. 2000.
126. S. J. Zieman, V. Melenovsky, and D. A. Kass, "Mechanisms, pathophysiology, and therapy of arterial stiffness," *Arteriosclerosis, thrombosis, and vascular biology*, 25, 932–943, 2005.